ALMA MATER STUDIORUM
UNIVERSITA' DEGLI STUDI DI BOLOGNA

Strongly correlated quantum gases in one dimension

TESI DI DOTTORATO IN FISICA

Candidato:
Marcello DALMONTE

Relatore
Prof.sa Elisa ERCOLESSI

Coordinatore
Prof. Fabio ORTOLANI

Co-relatori:
Prof. Peter ZOLLER &

Dr. Guido PUPILLO

SSD: Fis/02, Ciclo XXIII
Esame Finale anno 2011

Contents

1 Quantum matter in low dimensionality: a brief overview **1**
1.1 How does ″quantum″ matter in one-dimension? 1
1.1.1 Mermin-Wagner-Hohenberg theorem 2
1.1.2 Conformal symmetry in 1D 3
1.1.3 How to tackle 1D problems 4
1.1.4 Universality classes: Tomonaga-Luttinger liquids and sine-Gordon model 5
1.2 Experimental realization of one dimensional systems 6
1.2.1 Ultracold atoms and molecules loaded into optical lattices: a dream for theoreticians. 7

I Quantum emulators in one dimension **9**

2 Validation of a quantum analog simulator: sine-Gordon model with cold atoms **15**
2.1 Quantum sine-Gordon model with cold atoms 16
2.2 Methods Summary 23
2.2.1 Sample preparation. 23
2.2.2 Phase transition line. 25
2.3 Methods 25
2.3.1 1D Bose gas in a weak optical lattice. 25
2.3.2 Deep lattice: the Bose-Hubbard model. 26
2.3.3 Magnetic Feshbach resonance 26
2.3.4 Lattice loading and array of 1D tubes. 27
2.3.5 Commensurability. 27
2.3.6 Modulation parameters and error bars. 28

II Atomic bosonic and fermionic mixtures 29

3 Fermi-Fermi mixtures: pairing regimes and phase separation in the asymmetric Hubbard model. 35
- 3.1 Introduction . . . 35
- 3.2 Superconducting properties: singlet-pairing to charge-density wave transition at $U < 0$ . . . 37
- 3.3 Phase separation in the weak-coupling limit . . . 41
  - 3.3.1 Trial wave functions . . . 42
  - 3.3.2 Ground state energies . . . 43
  - 3.3.3 Phase boundaries . . . 46
- 3.4 Phase separation in the strong-coupling limit . . . 48
  - 3.4.1 Spinless fermions . . . 52
  - 3.4.2 Spatially separated states . . . 53
  - 3.4.3 PS′: Extensive number of intervals $M = \alpha L$ . . . 55
  - 3.4.4 Phase boundaries . . . 56
  - 3.4.5 Inclusion of phase separated states with an infinite number of interfaces . . . 59
- 3.5 Conclusions . . . 59

4 Pairing, crystallization and Haldane liquid of mass unbalanced atomic mixtures in one-dimensional optical lattices 63

5 Three-species mixtures: a color superfluid via three-body losses. 73
- 5.1 Three-body losses as three-body interactions . . . 73
- 5.2 Phase diagram in the constrained regime . . . 75
  - 5.2.1 Bosonisation formalism for the constrained Hamiltonian . . . 76
  - 5.2.2 Phase diagram from bosonisation . . . 77
  - 5.2.3 Ground state of H_C from DMRG (equal interactions) 79
  - 5.2.4 Ground state of H_C from DMRG (unequal interactions) . . . 79
  - 5.2.5 Time-dependent preparation of an ACS phase with ^{6}Li . . . 80
- 5.3 Addendum: detailed constraint mapping . . . 81
  - 5.3.1 Toy model: $\Gamma_3 \to \infty$ . . . 82
  - 5.3.2 Effective theory and pseudofermionic mapping . . . 82

6 Outlook: quantum magnetism and Bose-Bose mixtures 85
- 6.1 Bose-Bose mixtures: phase diagram from bosonization . . . 85
- 6.2 Numerical analysis . . . 86

6.2.1 Phase diagram at equal densities 87

III Long-range interacting systems in 1D and quasi-1D geometries 89

7 A new class of insulators: the Luttinger Staircase. 97
7.1 Single wire with long-range interactions 97
7.1.1 The Luttinger staircase 100
7.1.2 Analytical expression for K 104

8 Two-leg dipolar ladder: quasi-1D crystals and exotic bound states. 107
8.1 Introduction 107
8.2 Model Hamiltonian 109
8.2.1 Balanced case 110
8.2.2 Unbalanced case 112
8.2.3 Effect of the trap 114

9 Magnetic phases with long-range interactions: hidden order via three-body losses 117
9.1 Introduction 117
9.2 Bosonic Hamiltonian and λ-D model 118
9.3 Homogeneous phase diagram. 121
9.3.1 Strong coupling regime 126
9.4 Effect of a trapping potential. 127
9.4.1 Haldane order 128
9.4.2 Antiferromagnetic ordering 130
9.5 Conclusions 131
9.5.1 Addendum: constrained bosons - spin-1 mapping . . 134

CONTENTS

Introduction

One of the basic steps of Galilei's formulation of the scientific method[1] is the creation of a mathematical model which does not only embody all known aspects of a certain natural phenomenon, but can in principle explain effects yet to be observed: the formulation of *archetypes* is, by consequence, a building block of several experimental sciences, between them being, of course, physics. A typical example is represented by solid state physics: while solving the Schrödinger equation for 10^{23} atoms is by far an unsolvable problem, the possibility to describe such a system through simpler mathematical models provides several useful quantitative predictions which can be tested in the laboratory. However, solving models is not always an easy task, especially in the context of quantum mechanics. While numerical simulations based on classical computers can provide very accurate description to many-particle problems within classical statistical mechanics[2], no general solution method is known at the quantum level.

Almost thirty years ago, Richard Feynman proposed to invert the archetype paradigm[3]: instead of starting from a physical phenomenon which requires a quantitative explanation, one can first consider *the model* (archetype) and try to solve it by implementing its microscopic properties into a *quantum simulator*, that is, a highly controllable experimental setup in which one can faithfully mimic the basic properties of the archetype in question. The breakthrough proposal by Jaksch and coworkers [4] to *emulate* the so-called Bose-Hubbard model by using ultracold bosonic atoms loaded into optical potentials has paved the way to an entire new field in theoretical and experimental physics, that is, the investigation of ultracold matter in deep connection with many-body problems usually associated with other research fields such as condensed matter, high-energy and chemical physics. Remarkable experimental results related to many-body phenomena have already been achieved; between them, it is worth citing the superfluid-Mott insulator transition[5], the BEC-BCS crossover[6, 7] and the fermionization of one-dimensional bosonic gases[8, 9].

Two relevant questions naturally arise: *how can we validate a quantum emulator? Is it possible to disclose new physics, and clarify long-standing theoretical problems*?

The aim of the work presented here is to provide some quantitative answers to these questions in the context of one-dimensional systems. Low dimensional systems have remarkable differences with respect to 3D ones: from a theoretical standpoint, let us just mention that several solving techniques are available, and that the dominant role of quantum fluctuations can give rise to a rich variety of exotic phenomena. From the experimental point of view, cold atomic ensembles can be easily confined in 1D and, in addition, a growing number of materials can be described within 1D physics. Before coming to our original contributions, we will briefly review some 1D peculiarities in Chapter 1; then, we present our results divided in three parts, as described below.

In the first part of this thesis, we discuss how cold atoms can efficiently simulate quantum field theories. We focus on the so-called *sine-Gordon model*, an integrable theory widely studied in several ambits, from high-energy physics to condensed matter. By comparing analytical results with experimental measurements, we validate the system of interest as a powerful analog simulator, whose applications to a variety of many-body problems in low-dimensional physics can be of great interest for elucidating open problems.

In the second part, we present a series of results on one-dimensional multi-species Fermi gases. We first consider a variant of the Hubbard model(HM) in which the hopping rates are species-dependent(Chapter 3 and 4), and investigate some of its properties by means of numerical and analytical methods; interestingly, exotic effects, such as topological order and crystalline structure, can appear even in this relatively basic model. In Chapter 5, we turn our attention on dissipative effects on a three-species HM, which allow for the stabilization of a color superfluid phase which presents some analogies with the correspondent one in high-density QCD. In Chapter 6, we present a brief outlook on bosonic mixtures in one dimension and their relation with quantum magnetism, which is currently under investigation.

In the third and last part, the effect of non-local interactions usually present in cold dipolar gases is investigated in various setups. In Chapter 7, we consider a basic 1D geometry with purely repulsive interaction, and propose a quantitative field theoretical description for general interaction shape and strength. Part of these results are then employed in Chapter 8, where we show how a system composed of two coupled wires of dipolar particles displays a very rich phase diagram, including composite crystals

and the appearance of many-body bound states such as trimers. In Chapter 9, we show how dipolar bosons can also display various magnetic orders such as ferro-, antiferromagnetism and even topological order, which can be retained also in presence of a trapping potential requiring a minimal population control.

Contributors and publications

The relevant publications contained in this thesis are listed below, together with a brief description of all contributions by different authors:

- chapter 2 is a result from a theory/experiment collaboration with the group of Prof. Hanns-Christoph Nägerl in Innsbruck; the related reference is:
  1) E. Haller, R. Hart, M.J. Mark, J.G. Danzl, L. Reichsöllner, M. Gustavsson, G. Pupillo, M. Dalmonte and H.-C. Nägerl, Nature **466**, 597-600 (2010).
  G. P. and MD provided the theory support, whereas E. H., R. H., M.J.M., J-G.D., L.R., M- G. and H.-C.N. did the experimental work. All authors substantially contributed to the manuscript.

- chapter 3 is related to the following publication:
  2) L. Barbiero, M. Casadei, M. Dalmonte, C. Degli Esposti Boschi, E. Ercolessi and F. Ortolani, Phys. Rev. **B** 81, 224512 (2010).
  All the authors contributed substantially to the numerical and analytical work; in particular, MD carried the weak-coupling calculations. In addition, we present results from a forthcoming preprint:
  3) T. Roscilde, C. Degli Esposti Boschi and M. Dalmonte, to appear on the arXiv.
  Here, TR carried out quantum MonteCarlo calculations, and CDEB and MD provided theory support and DMRG results.

- chapter 5 is contained in the following publication:
  4) A. Kantian, M. Dalmonte, S. Diehl, W. Hofstetter, P. Zoller and A.J. Daley, Phys. Rev. Lett. **103**, 240401 (2009).
  All authors contributed substantially to the work; in particular, MD developed the analytical description of the system together with S.D.

- work in chapters 7 and 8 is contained in the following contributions:
  5)M. Dalmonte, G. Pupillo and P. Zoller, Phys. Rev. Lett. **105**, 140401 (2010).

6)M. Dalmonte, G. Pupillo and P. Zoller, to appear on the arXiv.
All authors contributed substantially in both works; MD introduced and developed the Luttinger liquid description in both papers, and carried out DMRG simulations in the second one.

- the main findings of chapter 9 are contained in the following preprint:
  7)M. Dalmonte, M. Di Dio, L. Barbiero and F. Ortolani, Phys. Rev. B **83**, in production (2011) (preprint available at arXiv:1009.5931v2).
  All authors contributed to numerical simulations and wrote the manuscript.

In addition, the results presented in Chapter 6 have been carried out in collaboration with Marco Mattioli and Fabio Ortolani, in the framework of a broader project together with Elisa Ercolessi and Davide Cornigli.

Chapter 1

Quantum matter in low dimensionality: a brief overview

This introductory chapter is devoted to the interesting features of low dimensional systems, with a particular emphasis on 1D physics. While we are far away from a complete presentation (for which we address the reader to classic texts such as Refs. [10] and [11]), we hope the topics treated below might give a rough idea on some peculiarities of one-dimensional systems.

In the first section, we present a theoretical point of view on low dimensionalities, illustrating general results and approaches to tackle many-body problems in one dimensional systems; in the second one, we give an overview on experimental realizations of such systems, starting from more standard condensed matter environments such as carbon nanotubes and Quantum Hall edge states, and finally focusing on quantum optics setups such as ultracold atoms and molecules loaded into optical lattices.

1.1 How does "quantum" matter in one-dimension?

The concept of symmetry has been fundamental in several ambits of human knowledge, ranging from sculpture and architecture to mathematics and biology. While most of its original understanding has been related to simple geometrical intuitions, the considerable progresses in topology and group theory in the last two centuries have strongly linked this rather abstract concept to the quantitative understanding of mathematical structures, equipping theoretical physicists with a powerful instrument to interpret a plethora of intriguing phenomena from high-energy physics to condensed matter systems.

One-dimensional physics flourishes of peculiarities, and, of course, symmetry is one of them.

1.1.1 Mermin-Wagner-Hohenberg theorem

One of the main general results in 1D physics is related to the so called *spontaneous symmetry breaking* (SSB) mechanism[12, 13, 14]. In statistical mechanics and quantum field theory, when a certain ground state exhibits less symmetry than the related Hamiltonian, one says that a certain symmetry has been broken: that's the essence of SSB. While various interesting phenomena, such as the emergence of superconductivity, can be explained in these terms, the most intuitive view on the subject is usually associated with the emergence of spontaneous magnetization in solids: given a certain ordered configuration $\mathcal{C}$ which minimizes the energy functional, an exactly opposite configuration $\mathcal{C}'$ with the same energy always exists. Nonetheless, the state of the system is not invariant under transformation $\mathcal{C} \leftrightarrow \mathcal{C}'$, and thus this *exchange* symmetry is broken[13].

The curious point is, in low dimensional systems, SSB suffers from a *no-go theorem* known as the *Mermin-Wagner(MW) theorem* (or Mermin-Wagner-Hohenberg(MWH) theorem). In their seminal paper [15], Mermin and Wagner showed that the Heisenberg model[16]:

$$H_{Heis} = \sum_{i,j} J_{ij} \vec{S}_i \vec{S}_j - h S_q^z \tag{1.1}$$

cannot display a finite magnetization $m(h)$ at finite temperature in one and two dimension, and at zero temperature in one dimension, if the interaction coefficients are short-range, that is:

$$\bar{J} = \frac{1}{2\mathcal{N}} \sum_{i,j} |J_{ij}||\vec{x}_i - \vec{x}_j|^2 < \infty \tag{1.2}$$

Here, $\mathcal{N}$ is the number of sites, $\vec{S}$ are standard spin operators and S_q^z is the so-called spin density wave operator [15]. In a similar fashion, Hohenberg [17] proved that a state cannot display a *standard* superfluid order in one and two dimensions at finite temperature using the so called *Bogoliubov inequality*[18, 19], which turns out to be fundamental even in the MW formulation.

The profound meaning of the MWH theorem is deeply rooted into the allowed symmetry of the system, being it quantum or classical. In its more general form, the MWH theorem states that, for short-range forces,

no phase transition associated with the SSB of a Lie group of symmetry can take place in space dimension $d < 3(4)$ for any $T > 0$ for a quantum (classical) system[14]. Interesting enough, a deep connection with a well known results in quantum field theory, the *Coleman theorem*[20], has been elucidated [13].

A natural question that arises is then: are there phase transition in one dimension? If so, how can we distinguish between different phases?

When replying to this query, the first element that should be taken into account is that, while SSB cannot involve continuos symmetries, discrete ones can still be broken. Typical examples of this situation are the superfluid-Mott insulator phase transition in the Bose-Hubbard model [21], where the translational symmetry U(1) is reduced to a discrete one related to the presence of an underlying lattice structure, and the Haldane phase of spin-1 chains [22], where non-explicit Z_2 symmetries are broken.

Another interesting feature of 1D systems is the so-called *quasi-long range order*(QLRO), which emerges in low dimensional critical theories as we will see in the next section.

1.1.2 Conformal symmetry in 1D

One of the most remarkable results in the context of 1D systems is related to the so called *conformal symmetry* [23, 24]. When a one dimensional quantum system is translationally and rotationally invariant, and, at the same time, does not display a typical length scale (that is, is also scale invariant), an additional symmetry, known as conformal, is also satisfied[25]. An analogous result holds for 2D classical systems[23].

The main effect of conformal invariance manifests itself in the asymptotic behavior of correlation functions. Let us consider, e.g., an action $\mathcal{S}(\Phi)$ and a two-point function:

$$\langle \phi_1(x_1)\phi_2(x_2)\rangle = \frac{1}{Z}\int [d\Phi]\phi_1(x_1)\phi_2(x_2)e^{-\mathcal{S}(\Phi)} \tag{1.3}$$

where $Z = \int [d\Phi]e^{-\mathcal{S}(\Phi)}$ and $\phi_{1,2}$ are fields with dimension $\Delta_{1,2}$. Applying scale, translational and rotational invariance, one gets:

$$\langle \phi_1(x_1)\phi_2(x_2)\rangle \simeq \frac{C_{12}}{|x_1 - x_2|^{\Delta_1+\Delta_2}} \tag{1.4}$$

which, considering also conformal invariance, reduces to[23]:

$$\langle \phi_1(x_1)\phi_2(x_2)\rangle = \delta(\Delta_1 - \Delta_2) * \frac{C_{12}}{|x_1 - x_2|^{\Delta_1}}. \tag{1.5}$$

This simple result has a remarkable consequence: in 1D critical models described by a conformal field theory (CFT), all correlation functions decay as power law at long distances. This immediately traces out SSB, in accordance with MWH theorem. One can anyway distinguish between different phases by looking at correlation function decay: in particular, the slowest decaying correlation is refereed as *dominant*, the remaining ones being *subdominant* [11]. We can then define that a system displays quasi-long-range order in a certain order parameter if the corresponding correlation function is dominant. As a simple example, let us consider a gas of bosons interacting via a repulsive delta-like potential. In 3D, bosons can condense, establishing a finite order parameter $\langle b \rangle \neq 0$; while in 1D this contingency is ruled out, one can still have a correspondent phase, which is usually referred as *1D superfluid*, when $\langle b_x^\dagger b_y \rangle$ is the slowest decaying correlation function (for further details, see Chapter 2 and relative references).

1.1.3 How to tackle 1D problems

The relevant role of quantum fluctuations, related to the results stated above, is responsible for the breakdown of some relevant many-body techniques when analyzing 1D models: between them, it is worth mentioning the mean field approach[14], the Landau theory of Fermi liquids[26], and most of diagrammatic techniques[11]. Nevertheless, various alternative numerical and analytical approaches work extremely well in 1D.

From the numerical side, exact diagonalization of relatively large systems (up to more than 30 sites for spin $1/2$ chains), combined with field theory techniques, has provided accurate solution of non-trivial problems such as the exact location of infinite-order phase transitions [11]. In addition, the so called *sign problem* of Quantum Monte Carlo (QMC) [11] methods when applied to fermionic models can be often neglected in 1D by mapping fermions to hard-core bosons through a *Jordan-Wigner transformation* [27]. Furthermore, the groundbreaking formulation of the density-matrix-renormalization group algorithm (DMRG) [28] has allowed the investigation of much larger systems with less computational effort, establishing DMRG as a state of art method to solve 1D problems at zero temperature. This method represents a substantial improvement with respect to standard numerical renormalization group algorithms [29], whose breakdown was evident even for non-interacting systems. It allows for precise numerical estimates of several physical quantities such as ground and excited state and energies, correlation functions and Renyi entropies, and

combined with finite size scaling theories gives a very accurate description of thermodynamic phase diagrams for 1D and quasi-1D systems. In this thesis, we employed a code developed in our group (in particular by Prof. Fabio Ortolani) with some extensions used to investigate system with non-local interactions, as explained in Chapters 8 and 9.

On the analytical side, the relative simpleness of 1D many-body problems has allowed for the formulation of exact solutions via *Bethe ansatz*: in essence, the system can be exactly diagonalized using purely analytical tools. Let us also mention the possibility to infer finite temperature properties of integrable systems within the *thermodynamical Bethe ansatz* framework [30].

However, all of these techniques dramatically improve when the underlying field theoretical background of a certain model is known.

1.1.4 Universality classes: Tomonaga-Luttinger liquids and sine-Gordon model

One of the most interesting field theory background in 1D bosonic, fermionic and even spin systems is the so called *Tomonaga-Luttinger liquid* (TLL) [31, 32], directly linked to the related model (TLM). The basic idea is, one can map most of 1D models into compactified bosonic field theories, whose complexity is determined by the initial number of degrees of freedom and by the nature of the interaction. This mapping is realized in the context of the *bosonization* technique [33, 10, 11] (see Appendix for a brief overview), and, once it is performed, it leaves us with one (or more) TLM, which can be exactly solved and from which one can extract all wanted correlation functions. In certain cases, additional terms, known in condensed matter as *backward* and *forward scattering*, can appear and give rise to an energy gap in the spectrum. In these cases, the underlying field theory is often embodied in the so called *sine-Gordon model* (sGM), which is of particular interest since it can unify in a single field theory background various mechanisms such as superfluid to Mott insulator and crystalline transition and several pairing mechanism in one dimension[10, 11].

In the remaining of this thesis, we will encounter several examples of such universality classes and show how, despite a very common theoretical background, they can give rise to an unexpected variety of physical phenomena (see Table 1.1 for a short-list).

Universality classes / *Microscopic models*	**sine-Gordon**	**Tomonaga-Luttinger**
Bosons in a periodic potential (Chapter 2)	Pinning transition	Superfluidity in the Lieb-Liniger model
Asymmetric Hubbard model (Chapter 3 and 4)	Crystalline transition	CDW/SS crossover
Constrained three-species Hubbard model (Chapter 5)	Two-color atomic superfluidity	Three-color atomic superfluidity
Asymmetric Bose-Bose mixtures (Chapter 6)	SCF-Neél transition	–
Dipolar bosons and fermions in periodic potentials (Chapter 7)	Class of crystalline transitions	SF/CDW crossover
2-leg dipolar ladder (Chapter 8)	multiparticle pairing (trimer liquids)	CDW/SS crossover
Constrained dipolar bosons (Chapter 9)	BKT transition toward hidden order	—

Table 1.1: Models investigated in this thesis and universality classes involved in each problem; for abbreviations, see the corresponding chapter.

1.2 Experimental realization of one dimensional systems

One of the most remarkable technological advances of the last half-century has been the possibility to experimentally realize and investigate physical systems in reduced dimensionality, e.g., where only certain spatial degrees of freedom are relevant. The first breakthrough observation of the *integer Quantum Hall Effect* [34] in 1980 has paved the way to a series of theoretical efforts directly linked to the possibility to explain physical phenomena in $D < 3$. The D=2 jungle is very broad and intricated: among all, it is worth citing remarkable experiments on high-temperature superconductivity [35], graphene [36] and topological insulators [38].

Interest on the 1D world is instead more recent, albeit early experiments on polymers structure were already performed in the late 70's. The notable technological advances in material science such as better sample preparation and improved probing techniques have shown that many

condensed matter systems display 1D properties. Between them, edge states in fractional Quantum Hall material have been shown to behave as *chiral TLL*[39], as well as carbon nanotubes[37] and several spin-ladder materials[11]. While several groundbreaking 1D features have already been observed, material science is still characterized by a limited possibility to *"tune"* material properties and access a limited number of underlying models. On the contrary, ultracold atoms and molecules trapped into optical potentials have opened a new perspective in many-body physics of low dimensional systems.

1.2.1 Ultracold atoms and molecules loaded into optical lattices: a dream for theoreticians.

The realization of Bose-Einstein condensation in 1995 [40, 41] represented one of the most remarkable experimental achievements in basic quantum mechanics back from its origin: the possibility to cool up to 10^5 alkali atoms down to less than a μK allowed for the observation of this macroscopic effect, consequence of a microscopic property such as Bose-Einstein statistic. From the point of view of strong correlations, however, these systems did not look immediately interesting because, among all, of their very dilute nature.

Two groundbreaking contributions then came into play. The first one was the observation of *Feshbach resonances* [42], which allow to tune the interparticle scattering length, and so the interactions, by simply tuning the magnetic field which acts on the atoms [43]. The second one was the idea to use optical potentials, created by counter propagating laser beams beams, to simulate a periodic potential [4], known as *optical lattice*, very similar to the one created by ions in standard materials. The realization of the superfluid to Mott insulator transition in a Bose gas subject to a 3D optical lattice paved the way to the observation of several strongly interacting states of matter such as the Tonks-Girardeau and super-Tonks gas, fermionic insulators and pairing regimes, just to cite few examples (see [44] and [45] for a complete overview).

In a quantum optical setup, one can tune with impressive accuracy all the ingredients of a certain model, such as particle statistics, interactions and disorder, and configurational space, in both geometry and dimensionality. The situation is thus quite different with respect to condensed matter systems, where there is little to none control on several microscopic properties, making a rigorous correspondence from a certain model to a physical system challenging.

Ultracold atoms (and molecules, as we will see later in Part III) provide then an unmatched background to test a variety of theoretical techniques and investigate physical problems so far unsolved, such as HTc superconductivity, supersolidity and thermalization in quantum dynamics [44, 46].

Part I

Quantum emulators in one dimension

In recent years, the idea of a quantum simulator has emerged as a useful tool to investigate physical phenomena whose explanation is still in question. Differently with respect to classical systems, quantum ones are much harder to simulate due to the exponential growth of the Hilbert space, which implies that a huge amount of computational resources are needed in order to efficiently describe real systems and physical processes. The basic idea of quantum emulation, or quantum analog simulation, is, in fact, quite natural[3, 47, 48]: in order to solve a quantum mechanical problem, one can employ a specifically designed laboratory quantum system which efficiently describe the considered model. Thus, quantum simulations do not only provide a specific insight on unsolved problems, but would also allow for accurate tests of various theoretical techniques employed to approximately solve the problem itself. In addition, quantum analog simulations are typically much less demanding than a complete, programmable quantum computer; they do not require an almost perfect realization of a quantum gate or error correction, and small number of *qubits* are usually needed in order to get appropriate answers.

While there is a broad plethora of yet unexplained physical phenomena, the possibility to realize a quantum emulator would be of extreme interest in two specific fields: quantum field theory (QFT) and strongly correlated systems (SCS). This is mainly due to the fact that, in both fields, *i)* controlled numerical algorithm are usually limited to particular configurations and are in general not universal, and *ii)* longstanding problems such as High-temperature superconductivity (HTc) and the complete phase diagram of QCD are yet to be solved.

In SCS, the main problem is related to the fact that while bosonic systems can be faithfully simulated via quantum MonteCarlo (QMC) calculations, fermionic and frustrated spin models are affected by the so-called *sign problem*, which reduces the possibility to treat them within QMC-based approaches. While different algorithms such as exact diagonalization, density-matrix renormalization group (DMRG) or dynamical mean-field theory (DMFT) have provided alternative methods for specific dimensional configurations, relevant models typical in SCS are yet to be solved; between them is the so-called *Hubbard model* (HM)[49, 50], a simple lattice model whose Hamiltonian contains a kinetic term and a local interaction which mimics a screened Coulomb repulsion between electrons:

$$H_{HM} = -t \sum_{<i,j>,\sigma=\uparrow,\downarrow} (c^{\dagger}_{i,\sigma} c_{j,\sigma}) + U \sum_{i} n_{i,\uparrow} n_{i,\downarrow}. \tag{1.6}$$

Despite its simplicity, an exact solution of (1.6) is known only in the one dimensional case [51, 52]. The suggestion that the 2D version of the HM

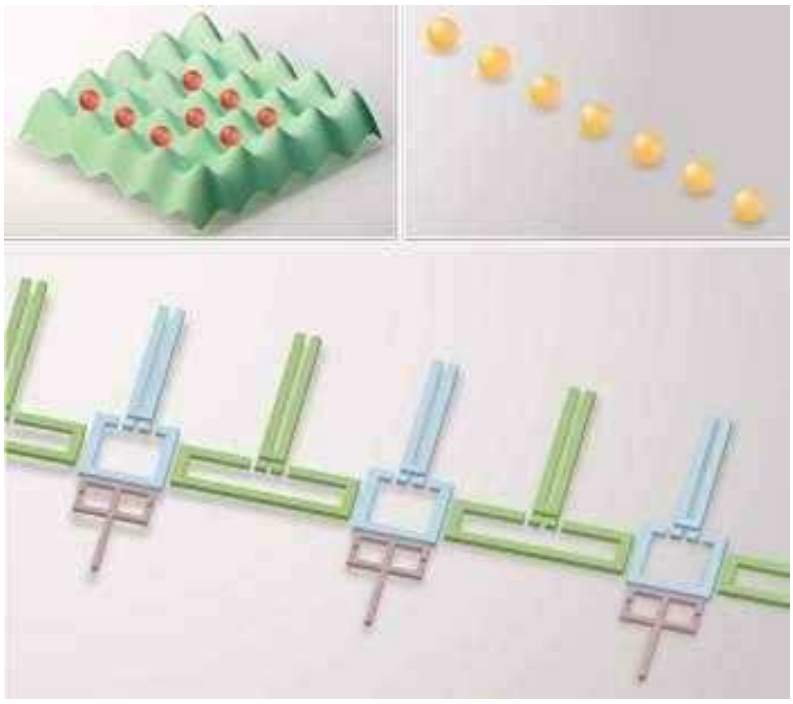

Figure 1.1: **Typical examples of analog quantum simulators**: cold atoms into optical lattices(top, left), a string of trapped ions(top, right) and superconducting circuits(bottom). Image from Ref. [48].

on a square lattice could explain the basic mechanism of high temperature superconductivity has strongly increased the interest on the HM itself. However, despite numerous results on the subject, a complete phase diagram is still missing. Analogous problems have been posed in QFT, where analytical techniques often reduce to perturbative arguments, and numerical simulations are challenging. In both contexts, a quantum simulator would then provide a groundbreaking insight on many unsolved problems. In recent years, several experimental setups have been proposed to simulate specific models: the reign of quantum simulators is quite rich, ranging from electrons in superconducting circuits and arrays of quantum dots [48] to trapped ions [53, 54, 55], photons and polaritons in arrays of cavities [56] (some typical examples are sketched in Fig. 1.1). In particular, cold atomic gases confined into optical lattices [4] have already proved to be a faithful simulator of typical condensed matter problems in a series of notable experiments [5, 57] (see Fig. 1.2) which describe at different levels the Mott Insulator-superfluid transition of the Bose-Hubbard model [21]. The broad degree of control and tunability combined with efficient prob-

ing techniques makes these systems suitable candidates to simulate not only SCS, but also quantum field theories, as recently emerged in various theoretical proposal (see, e.g., Ref. [58] and references therein). While several results have already been achieved with trapped ions, such as the quantum simulation of the Dirac equation [53] and the Klein paradox [54], similar results were not available with cold atoms up to 2 years ago.

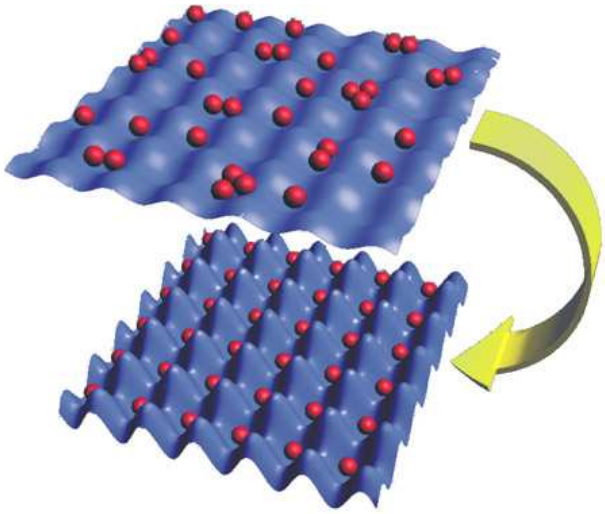

Figure 1.2: **Superfluid to Mott insulator quantum phase transition as realized in Ref. [5]**: by loading a Bose-Einstein condensate of ^{87}Rb atoms into a 3D optical lattice, Greiner and coworkers were able to show that the system undergoes a quantum phase transition from a superfluid phase to a Mott insulator as the depth of the lattice is increased.

At first hint, the first requirement for a quantum emulator is the possibility to validate its prediction towards known results, at least in some limits. A similar procedure has been carried out comparing extensive QMC results on the finite-temperature Bose-Hubbard model with experimental results [57]. The validation procedure constitutes a fundamental step toward simulation of more challenging theoretical problems.

In the remainder of the chapter, we will discuss the validation procedure of a cold atomic setups with respect to a well known QFT, the *sine-Gordon* model (SGM) [10, 59, 60]. Our validation is based on the integrable nature of the SGM, which provides us very accurate analytical results to be compared with experimental findings. The remarkable matching of theoretical predictions with experiments paves the way to the investigation of more complex problem related to 1D systems, such as transport properties

of Luttinger liquids and quantum dynamic.

Chapter 2

Validation of a quantum analog simulator: sine-Gordon model with cold atoms

One of the most remarkable results of quantum mechanics is the fact that many-body quantum systems may exhibit phase transitions even at zero temperature[12]. Quantum fluctuations, deeply rooted in Heisenberg's uncertainty principle, and not thermal fluctuations, drive the system from one phase to another. Typically, the relative strength of two competing terms in the system's Hamiltonian is changed across a finite critical value. A well-known example is the Mott-Hubbard quantum phase transition from a superfluid to an insulating phase[4, 5], which has been observed for weakly interacting bosonic atomic gases. However, for strongly interacting quantum systems confined to lower-dimensional geometry a novel type of quantum phase transition may be induced for which an arbitrarily weak perturbation to the Hamiltonian is sufficient to drive the transition[11, 10]. Here, for a one-dimensional (1D) quantum gas of bosonic caesium atoms with tunable interactions, we observe the sine-Gordon quantum phase transition from a superfluid Luttinger liquid to a Mott-insulator [61, 62]. For sufficiently strong interactions, the transition is induced by adding an arbitrarily weak optical lattice commensurate with the atomic granularity, which leads to immediate pinning of the atoms. We map out the phase diagram and find that our measurements in the strongly interacting regime agree well with a quantum field description based on the exactly solvable sine-Gordon model[59]. We trace the phase boundary all the way to the weakly interacting regime where we find good agreement with the predictions of the 1D Bose-Hubbard model. Our results open up the experimental study of quantum phase transitions,

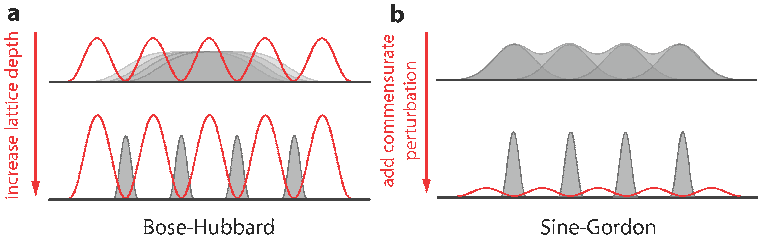

Figure 2.1: **Comparing two types of superfluid-to-Mott-insulator phase transitions in 1D.** Schematic density distributions (grey) in the presence of a periodic potential (red solid line). **a**, Mott-Hubbard type quantum phase transition for weak interactions[5]. The system is still superfluid at finite lattice depth (top). The transition to the insulating state is induced by raising the lattice depth above a finite critical value (bottom). **b**, Sine-Gordon type quantum phase transition for strong interactions[61]. In the absence of any perturbation, the system is a strongly correlated superfluid (top). For sufficiently strong interactions, not necessarily infinitely strong, an arbitrarily weak perturbation by a lattice potential commensurate with the system's granularity induces the transition to the insulating Mott state (bottom).

criticality, and transport phenomena beyond Hubbard-type models in the context of ultracold gases.

2.1 Quantum sine-Gordon model with cold atoms

Ultracold atomic gases are a versatile tunable laboratory system for the investigation of complex many-body quantum phenomena[44]. The study of quantum phases and quantum phase transitions is greatly enriched by the possibility to independently control the kinetic energy and the interactions. In deep optical lattice potentials the many-body dynamics for a weakly interacting gas is, to a very good approximation, governed microscopically by a Hubbard Hamiltonian[4] with a local onsite interaction energy U and kinetic energy J, which corresponds to tunneling of atoms from one lattice site to the next. Experiments with Bose-Einstein condensates (BEC) of Rb atoms have demonstrated the quantum phase transition from a superfluid phase for large J to an insulating Mott-Hubbard (MH) phase[5]. The transition between these two phases was obtained by quenching J in a lattice of finite depth. Recent experiments with fermionic atoms have demonstrated the presence of a fermionic MH insulating

state[63, 64], potentially opening the way to the study of high-temperature superconductivity in proximity of the MH phase in 2D.

Pinning transition with ultracold bosons

While the focus in the study of quantum phase transitions in the context of ultracold atoms has so far been on Hubbard-type physics in the weakly interacting regime, novel quantum phenomena occur in lower dimensions, where the effects of quantum fluctuations and correlations are enhanced. In a 1D bosonic gas, strong repulsive interactions lead to the formation of a Tonks-Girardeau (TG) gas, where bosons minimize their interaction energy by avoiding spatial overlap and acquire fermionic properties[65, 9, 8, 66]. The addition of an arbitrarily weak lattice potential commensurate with the atomic density, i.e. $n \sim 2/\lambda$, where n is the linear 1D density and $\lambda/2$ is the lattice periodicity, is expected to lead to a novel kind of quantum phase transition[11, 61]: the strongly correlated 1D gas is immediately pinned by the lattice and the superfluid TG phase is turned into an insulating, gapped phase. Figure 2.1 contrasts the Hubbard-type superfluid-to-Mott-insulator transition to this pinning transition. Given the universality of 1D quantum physics, the pinning transition will occur for interacting bosons as well as for fermions in 1D and has been discussed with respect to a variety of quantum models in low dimensions[11].

The pinning transition is described by the (1+1) quantum sine-Gordon (sG) model, which is an exactly solvable quantum field theory, extensively studied in high energy, condensed matter, and mathematical physics[10]. The sG Hamiltonian reads

$$\mathcal{H} = \frac{\hbar v_s}{2\pi} \int dx[(\partial_x\theta)^2 + (\partial_x\phi)^2 + \mathcal{V}\cos(\sqrt{4K}\theta)]. \tag{2.1}$$

Here, $\partial_x\theta$ and $\partial_x\phi$ are the fluctuations of the long-wavelength density and phase fields θ and ϕ, respectively, of the hydrodynamic description of the 1D liquid with commutation relation $[\partial_x\theta(x), \phi(y)] = i\pi\delta(x-y)$, v_s is the velocity of the soundlike excitations of the 1D gas, $\mathcal{V} = Vn\pi/(\hbar v_\mathrm{s})$ is proportional to the depth V of a weak lattice[11, 61], and $\hbar$ is Planck's constant h divided by 2π. For vanishing lattice $\mathcal{V} = 0$, Eq. (2.1) describes a Luttinger liquid, where the strength of interactions is parameterized by the dimensionless parameter $K = \hbar\pi n/(mv_\mathrm{s})$, which determines the long-distance power-law decay of the correlation functions, e.g. $\langle n(x)n(x')\rangle \sim n^2 + cK/(x-x')^2 + c'\cos(2\pi n*(x-x'))/(x-x')^{2K} + \ldots$, with c and c' constants and m the atomic mass. The sG model with a weak but finite lattice predicts a quantum phase transition of the Berezinskii-Kosterlitz-Thouless

(BKT) type between a superfluid state for $K > K_c = 2$, where the shallow lattice is an irrelevant perturbation, to an insulating Mott phase for $K < K_c$, for which the spectrum is gapped for any value of $\mathcal{V}$.

While in general K is a phenomenological parameter, in the case of a 1D bosonic gas it can be microscopically related to the Lieb-Liniger parameter $\gamma = mg/(\hbar^2 n)$, which characterizes interactions in a homogenous 1D system[67] (see section 2.2). Here, $g \simeq 2\hbar\omega_\perp a_{3D}$ is the coupling constant of the 1D δ-function interaction potential $U(x) = g\delta(x)$, where $\omega_\perp$ is the frequency of transverse confinement and a_{3D} is the 3D scattering length. The strength of interactions, and thus K, can be tuned by varying a_{3D} near a Feshbach resonance[43]. The TG regime corresponds to $\gamma \gg 1$. Using the relation between K and γ, Büchler and coworkers[61] have shown that particles are pinned for experimentally accessible values of $\gamma > \gamma_c \simeq 3.5$ in the limit of a vanishingly weak lattice. The pinning transition is expected to continuously transform into the MH-type quantum phase transition, which occurs for the weakly interacting gas when the lattice depth becomes sufficiently large. Here, using a quantum gas of caesium (Cs) atoms with tunable interactions confined to an array of independent 1D tubes (see section 2.2), we drive the superfluid-to-Mott-insulator phase transition by varying γ and determine the phase boundary all the way from the strongly to the weakly interacting regime using modulation spectroscopy and measurement of transport. For shallow lattices under conditions of commensurability, we observe immediate pinning of the particles for strong interactions when $\gamma > \gamma_c$.

Experimental results and comparison with theory

We first discuss our experiments in the strongly interacting regime. We start with a 3D Bose-Einstein condensate (BEC) of typically 1.3×10^5 Cs atoms without detectable thermal fraction in a crossed-beam dipole trap with magnetic levitation[68] and initialize our system by creating a conventional 3D MH-state in a deep 3D lattice at $U/(6J) \approx 75$ with precisely one atom per lattice site[5]. We find, by reversing the loading, that the procedure does not lead to heating of the sample. The array of 1D tubes is obtained by reducing the lattice depth V along one direction. Our procedure ensures that a majority of tubes has a near-commensurate number density (see Methods). A Feshbach resonance allows us to control a_{3D} with a precision of $3\ a_0$ limited by the presence of the magnetic field gradient. Here, a_0 is Bohr's radius. For the case of the shallow lattice, we probe the state of the system by amplitude modulation spectroscopy[69, 70]. We determine the presence of an excitation gap E_g by testing whether some energy can be

deposited into the 1D system at a given excitation frequency f. The lattice depth V is modulated at f by 25% to 45% for $40 - 60$ ms. After ramping down the lattice beams adiabatically with respect to the lattice band structure and after a levitated expansion time of $40 - 60$ ms[68], we detect the atoms by time-of-flight absorption imaging. We determine the spatial width of the atomic sample from a gaussian fit to the absorption profile and obtain the change δ of the spatial width compared to the unmodulated case as a function of f. Two typical measurements are shown in Fig. 2.2(a), one in the superfluid phase and one deep in the 1D Mott phase at the same value for the lattice depth, $V = 1.5(1)E_{\mathrm{R}}$, where $E_R = h^2/(2m\lambda^2)$ is the photon recoil energy. For weak interactions the system exhibits a linear increase for δ as a function of f, which we attribute to the superfluid character of the gas. For strong interactions, the increase, after a slow rise, shows a clear kink. We attribute the initial slow rise to excitation of residual superfluid portions of our inhomogeneous system and the sudden change in slope to the presence of an excitation gap. We associate the axis intercept f_{g} obtained from a linear fit to the steep part of the spectrum with the frequency of the gap. To determine the phase transition from the 1D Mott state to the superfluid state, we repeat this measurement for a given depth V as we scan γ by changing a_{3D}. A typical result is shown in Fig. 2.2(c). The gap closes as γ is reduced. For values $V \leq 2.0E_{\mathrm{R}}$, the transition point is identified with the abrupt step, i.e. we determine the critical value $\gamma_{\mathrm{c},V}$ at which the transition happens by an error-function fit to the data. Note that we always observe some small residual value for f_{g} of about 120 Hz for weak interactions. In general, we find that the measured value for the frequency of the gap is robust against variations of modulation amplitude, while the slope increases with stronger modulation.

For comparison, we present in Fig. 2.2(b) and (d) excitation spectra for an intermediate value of the lattice depth and for the case of a deep lattice, respectively. For $V = 3.0(2)E_{\mathrm{R}}$ the spectrum shows additional structure for high frequencies as band structure comes into play. We find that for $V > 2.0E_{\mathrm{R}}$ the gap opens up approximately linearly as a function of γ beyond a critical $\gamma_{\mathrm{c},V}$, see inset to Fig. 2.2(c). For deep lattices and for comparatively weak interactions the spectrum exhibits a broad distribution characteristic of a superfluid. For stronger interactions we recover the discrete excitation spectrum of the Mott phase in the Hubbard regime[5, 69] with a pronounced peak at $f = 1.0\ U/h$. Additional peaks[71] can be found at $f = 0.5\ U/h$ and above $f = 1.5\ U/h$.

For the case of a deep lattice, we find that the state of the system is very sensitively probed by transport measurements[73, 72]. A characteristic property of the Mott state is the inhibition of particle motion. In our

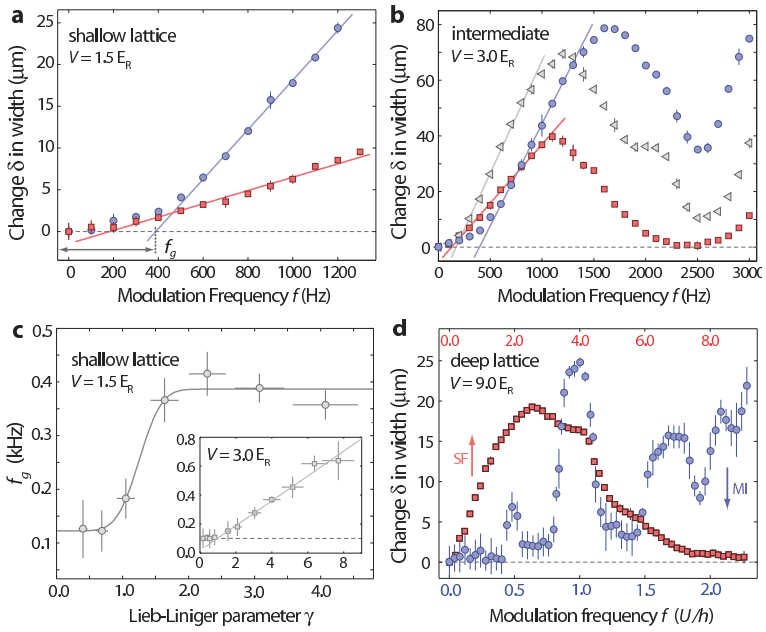

Figure 2.2: **Modulation spectroscopy on bosons in 1D. a, b, d**, Excitation spectra for low, intermediate, and high lattice depth V. The change δ of the spatial width after amplitude modulation is plotted as a function of the modulation frequency f for different values of γ. **a**, Characteristic spectra for $V = 1.5(1)E_{\mathrm{R}}$ in the superfluid (squares, $a_{3\mathrm{D}} = 115(2)\ a_0$, $\gamma = 1.0(1)$) and in the Mott regime (circles, $a_{3\mathrm{D}} = 261(2)\ a_0$, $\gamma = 3.1(2)$). The solid lines are linear fits to the high-frequency part of the spectrum. We determine the axis intercept f_{g} as indicated. **b**, Spectra for $V = 3.0(2)E_{\mathrm{R}}$. The system is superfluid at $\gamma = 0.51(6)$ (squares), while it exhibits a gap for $\gamma = 1.6(1)$ (triangles) and $\gamma = 4.1(3)$ (circles). **c**, Determination of the transition point for the case of the shallow lattice with $V = 1.5(1)E_{\mathrm{R}}$. The frequency f_{g} is plotted as a function of γ. The solid line is an error-function fit to the data. The inset plots f_{g} as a function of γ for $V = 3.0(2)E_{\mathrm{R}}$. **d**, Spectra for $V = 9.0(5)E_{\mathrm{R}}$ for weak (squares, $\gamma = 0.10(3)$) and strong (circles, $\gamma = 8.1(4)$) interactions in the superfluid (SF) and Mott insulator (MI) regimes. Here, f is in units of U. Modulation parameters and errors bars are discussed in the Methods.

experiment with the capability to tune interactions we expect the phase transition to manifests itself, at fixed V, through a strong suppression of transport when the strength of the interaction is raised above a certain critical value. Essentially, we test whether momentum can be imparted to the 1D system as a function of interaction strength. For a given V we apply a weak axial magnetic force for a brief time to the interacting system, chosen such that the imparted momentum would be approximately $0.2\hbar k$ if the system were non-interacting. Then, as a function of a_{3D}, we determine the center-of-mass displacement x_0 of the sample after a fixed time of flight. Fig. 2.3 shows that x_0 decreases monotonically with a_{3D}. For the case of a deep lattice with $V = 9.0(5)E_R$ the quenching of transport is abrupt. At a certain critical value for a_{3D} transport is fully inhibited[74, 75]. We find the critical a_{3D} by a linear fit to the decreasing data and by determining the axis intercept and derive from this a critical $\gamma_{c,V}$. Reducing the lattice depth to $V = 5.0(3)E_R$ and $V = 2.0(1)E_R$ leads to a less abrupt quenching of transport. For stronger interactions, the decrease starts to level off. Nevertheless, the initial decrease is still linear, allowing us to determine the critical $\gamma_{c,V}$ by an extrapolation of the initially linear decrease to zero. The inset to Fig. 2.3 shows the measured critical ratio $(U/J)_c$ determined by our transport method as a function of lattice depth V. When we compare our results with the predicted value[76] of $(U/J)_c \approx 3.85$ for the transition in 1D, we find a slight systematic overestimation of the transition point. This, however, is expected in view of e.g. the spatial inhomogeneity of the sample and the BKT-type nature of the transition in a finite size system.

Summary

We summarize our results in Fig. 2.4, where we present the phase diagram as a function of $1/\gamma$ and V. The set $\{\gamma_{c,V}\}$ defines the phase boundary between the 1D Mott insulator and the 1D superfluid. The measurements based on modulation spectroscopy cover a range from $V = 4E_R$ down to $0.5E_R$ (circles), while the transport measurements extend from $V = 2E_R$ to $10E_R$ (squares). In the weakly interacting regime, $1/\gamma > 2$, our data are in good agreement with the prediction of the MH model (dashed line). In the strongly interacting regime, $1/\gamma < 1$, the measured phase boundary extrapolates to a finite critical value $1/\gamma_c$ for the Lieb-Liniger parameter as the lattice depth V is reduced to zero. Our results are in excellent quantitative agreement with the theory for a commensurate system based on the sine-Gordon model (solid line, see Methods), for which $\gamma_c = 3.5$. We also find good agreement between our two types of measurement techniques in the intermediate regime ($V = 2E_R$ to $4E_R$). Our results demonstrate the

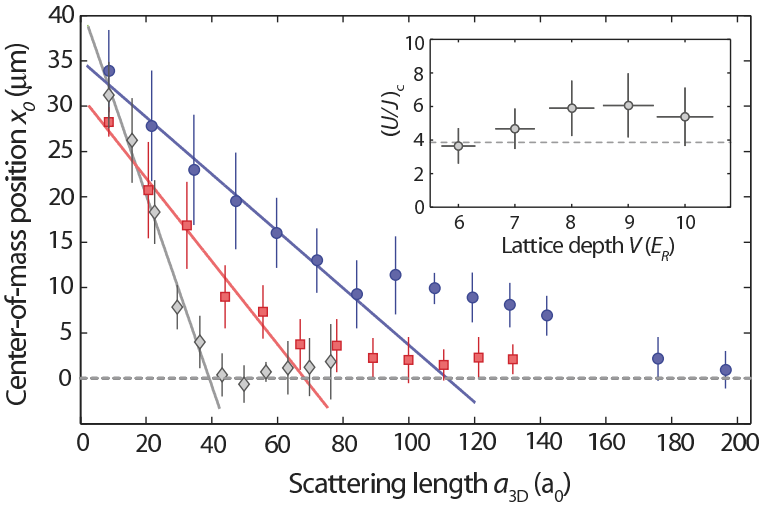

Figure 2.3: **Transport measurements on the 1D Bose gas.** Center-of-mass displacement x_0 as a function of a_{3D} for different values of V ($V = 9.0(5)E_R$ (diamonds), $V = 5.0(3)E_R$ (squares), $V = 2.0(1)E_R$ (circles)). We extrapolate the linear slope at small values for a_{3D} and associate the transition point with the axis intercept. For the data with $V = 2.0(1)E_R$ transport is not fully quenched as the condition of commensurability is not fulfilled for all atoms. All errors are the 1σ statistical error. The inset plots the mesured critical ratio $(U/J)_c$ at the transition point as a function of lattice depth V. The dashed line indicates the theoretical result $(U/J)_c \approx 3.85$ for the 1D Bose-Hubbard regime[76].

striking consequence of strong interactions in 1D geometry in the presence of a lattice: Beyond a critical value γ_c, an insulating Mott state exists for vanishingly small lattice depth V. The particles are immediately pinned by the lattice.

We measure a finite gap energy E_g for $\gamma > \gamma_c$ in the regime of a shallow lattice. In the limit of $\gamma \to \infty$ and $V \to 0$ one would expect the simple relation $E_g = V/2$ as the bosonic system has become fully fermionized and the lattice effectively induces a band insulator of fermions[61]. In the inset to Fig. 2.4 we plot the measured E_g as a function of V at fixed $\gamma = 11(1)$. For $V < 1E_R$ our data is in good agreement with the analytical result for the gap energy at finite γ (see Methods). Note that, for $V \geq 1E_R$, we observe a deviation for E_g away from the predicted values. This deviation occurs at rather shallow lattices. However, one does expect the curve to have a reduced slope for deeper lattices, for which E_g becomes of order U and is only weakly dependent on V.

Our results are a benchmark realization of quantum field theory models with tunable parameters in cold atomic systems. These results open up the experimental study of the out-of-equilibrium properties of sine-Gordon-type models. In particular, thermalization in integrable models beyond the Luttinger liquid model, quenches across quantum phase transitions, and their relations to the breakdown of the adiabatic theorem in low dimensions can now be investigated with full tunability of system parameters.

2.2 Methods Summary

2.2.1 Sample preparation.

We begin with a BEC with no detectable thermal fraction of typically 1.3×10^5 Cs atoms in the $|F = 3, m_F = 3>$ hyperfine ground state in a crossed-beam dipole trap with magnetic levitation. Details of the BEC preparation are presented elsewhere[68]. The BEC is adiabatically transferred to the 3D lattice by exponentially ramping up the power in the lattice laser beams within 300 ms. We create a 3D Hubbard-type Mott insulator with precisely one atom per site in the central region of the trap by adjusting the external dipole trap confinement prior to loading into the lattice. The array of vertically oriented tubes is created by ramping down the power in the vertically propagating beam pair. Typical trapping frequencies for the tubes are $\omega_{r,z} = 2\pi \times (12300(200), 21.9(3))$ Hz along the transversal and longitudinal directions, respectively.

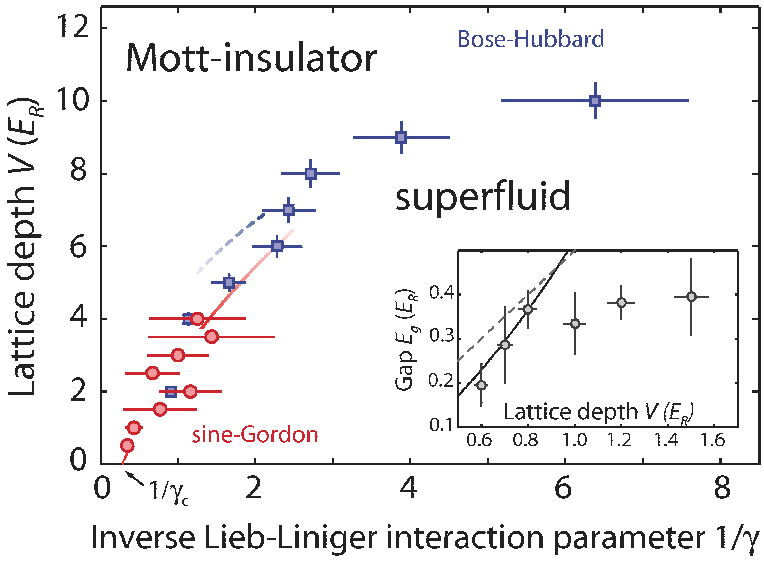

Figure 2.4: **Phase diagram for the strongly interacting 1D Bose gas.** Superfluid and Mott insulating phases in 1D versus inverse Lieb-Lininger interaction parameter $1/\gamma$ and optical lattice depth V in units of the photon recoil energy E_{R}. The critical interaction parameter is γ_{c}. For strong interactions and shallow lattices we determine the transition by amplitude modulation spectroscopy (circles). For weak interactions and deep lattices we probe the phase boundary by transport measurements (squares). The solid (dashed) line is the prediction from the sine-Gordon (Bose-Hubbard) model. Error bars are discussed in the Methods. The inset plots the measured gap energy $E_{\mathrm{g}} = hf_{\mathrm{g}}$ as a function of V for $\gamma = 11(1)$ and compares our data to the analytical result for finite γ as given by the sine-Gordon model (solid line, see Methods). Also shown is the universal behavior $E_{\mathrm{g}} = V/2$, which is valid for non-interacting fermions (dashed line).

It is not necessary to strictly adhere to the commensurate density condition to observe the pinning transition at very weak lattices[61]. However, we prepare our sample such that the commensurability condition is on average best fulfilled over the inhomogeneously populated array of tubes. We find this optimal configuration when the total atom number is chosen such that the peak density of the center tube is approximately $1.2\, n_{\mathrm{c}}$, where $n_{\mathrm{c}} = 2/\lambda$ is the commensurate 1D density. Typically there are about 60 atoms in the center tube.

2.2.2 Phase transition line.

For the case of a 1D Bose gas in a weak optical lattice the effective sine-Gordon Hamiltonian Eq. (2.1) is realized. In this regime, the BKT transition line between the superfluid and the Mott-insulating phases can be derived in terms of V and $\gamma = \gamma_{\mathrm{c},V}$ as

$$\frac{V}{E_{\mathrm{R}}} = 2\left(\frac{\pi}{\sqrt{\gamma - \gamma^{3/2}/(2\pi)}} - 2\right).$$

When the system is weakly interacting, $\gamma \ll 1$, and for deeper lattices, $V \gg 1E_{\mathrm{R}}$, the system can be described by the Bose-Hubbard Hamiltonian[4]. In this regime, the quantum phase transition between a superfluid and a MH state occurs at[76] $(U/J)_{\mathrm{c}} \approx 3.85$, which determines a transition line in the (V, γ) - plane via

$$\frac{4V}{E_{\mathrm{R}}} = \ln^2\left[\frac{2\sqrt{2}\pi}{\gamma}\left(\frac{U}{J}\right)_{\mathrm{c}}\sqrt{\frac{V}{E_{\mathrm{R}}}}\right].$$

Here, J is the hopping energy, and U is onsite interaction energy of the Bose-Hubbard model.

2.3 Methods

2.3.1 1D Bose gas in a weak optical lattice.

In the absence of the optical lattice, $V = 0$, the Luttinger liquid parameter K can be expressed in terms of the Lieb-Liniger parameter $\gamma = gm/(\hbar^2 n)$ for all strengths of interactions[67, 182]. For $\gamma \leq 10$ and $\gamma \gg 10$ one gets $K \simeq \pi/\sqrt{\gamma - \gamma^{3/2}/(2\pi)}$ and $K \simeq (1 + 2/\gamma)^2$, respectively. The addition of a weak but finite commensurate optical lattice with $V \leq 1E_{\mathrm{R}}$ realizes the

effective sine-Gordon Hamiltonian Eq. (2.1). Using a perturbative renormalization group approach, the BKT transition line between the superfluid and the Mott-insulating phases can be derived in terms of V and $\gamma = \gamma_{c,V}$ as

$$\frac{V}{E_R} = 2\left(\frac{\pi}{\sqrt{\gamma - \gamma^{3/2}/(2\pi)}} - 2\right).$$

For small lattice depths, the integrable structure of the sine-Gordon model[60, 78] allows one to derive the following analytical expression for the dependence of the spectral gap E_g on V and K

$$\frac{E_g}{E_R} = \frac{8\Gamma[\frac{\pi K}{2(2-K)}]}{\sqrt{\pi}\Gamma[\frac{1}{2}\frac{2+K(\pi-1)}{2-K}]}\left[\left(\frac{K^2 V}{16 E_R}\right)\frac{\Gamma[1-\frac{K}{2}]}{\Gamma[1+\frac{K}{2}]}\right]^{\frac{1}{2-K}}.$$

Here, Γ is the gamma function. For strong interactions $K \simeq 1$, the dependence of the gap on V is linear, and E_g approaches the free fermion value $E_g = V/2$. In the vicinity of $K = 2$, the gap closes exponentially approaching the BKT transition line.

2.3.2 Deep lattice: the Bose-Hubbard model.

In the weakly interacting regime $\gamma \ll 1$, for $V \gg 1E_R$, when all atoms occupy the lowest vibrational state in each potential well of the lattice, the system can be described by the following Bose-Hubbard model[4]

$$H = -J\sum_i (b_i^\dagger b_{i+1} + h.c.) + \frac{U}{2}\sum_i b_i^\dagger b_i^\dagger b_i b_i.$$

Here, b_i ($b_i^\dagger$) is the operator destroying (creating) a bosonic particle at the position of the i^{th}-well, $J = 4E_R(V/E_R)^{\frac{3}{4}}\exp[-2\sqrt{V/E_R}]/\sqrt{\pi}$ is the hopping energy, and $U = \sqrt{2\pi}g(V/E_R)^{1/4}/\lambda$ is onsite interaction energy. The quantum phase transition between a superfluid and a MH state occurs at[76] $(U/J)_c \approx 3.85$, which determines a transition line in the (V, γ) - plane via

$$\frac{4V}{E_R} = \ln^2\left[\frac{2\sqrt{2}\pi}{\gamma}\left(\frac{U}{J}\right)_c\sqrt{\frac{V}{E_R}}\right].$$

2.3.3 Magnetic Feshbach resonance

The strength of interaction can be tuned by means of a broad magnetic Feshbach resonance with a pole at -11.7 G and with a zero crossing for

the scattering length near 17 G[68]. To hold the atoms in the vertically oriented tubes, magnetic levitation by means of a magnetic field gradient is applied. For a cesium atom in the hyperfine state $\{F = 3, m_F = 3\}$ a magnetic field gradient of 31.1 G/cm cancels the gravitational force.

2.3.4 Lattice loading and array of 1D tubes.

We create a 3D optical lattice by interference of 3 pairs of counterpropagating dipole trap laser beams at wavelength $\lambda = 1064.5$ nm with $1/e^2$ beam waists of ~ 350 μm. The atomic BEC, initially trapped in a crossed-beam dipole trap, is adiabatically transferred to the 3D lattice by exponentially ramping up the power in the lattice laser beams within 300 ms. At the same time we increase the interaction strength by linearly raising the magnetic field strength and finally reach a 3D Hubbard-type Mott insulator with precisely one atom per site in the central region. The array of vertically oriented tubes is created by linearly ramping down the power in the vertically propagating beam pair in 100 ms reaching lattice depths from 10 to 0.5 E_R. At the same time we linearly reduce the magnetic field strength to set a_{3D}. Typical trapping frequencies for the tubes are $\omega_{r,z} = 2\pi \times (12300(200), 21.9(3))$ Hz along the transversal and longitudinal directions, respectively. The depth of the lattice along the tubes is calibrated by the pulsed Raman-Nath technique[79]. The transversal trapping frequencies of the tubes are determined by parametric heating measurements. The distribution of the atom number per tube can be directly determined from the density distribution in the Mott-insulating phase and shows an occupation of about 60 atoms in the center tube. Here, we assume a constant filling factor of one atom and no thermal or superfluid components. In view of our inhomogeneous system we calculate γ, for a given tube, by assuming a 1D Thomas-Fermi distribution and taking the center density. The reported γ is a weighted average over all tubes.

2.3.5 Commensurability.

To observe the pinning transition it is not necessary to fulfill the condition of commensurability precisely[61]. A finite commensurability parameter $Q = 2\pi(n - n_c)$ corresponds to a shift $\delta\mu$ of the chemical potential. Here, $n_c = 2/\lambda$ is the commensurate 1D density. The system stays locked to the Mott insulating phase as long as $\delta\mu$ remains smaller than the energy necessary to add another atom. When Q rises beyond a critical value $Q_c(\gamma, V)$, the system develops finite density excitations, which destroy the

long range order of the Mott insulator. We find that, for the array of 1D tubes, the commensurability condition in the superfluid regime is fulfilled best when the total atom number is chosen in such a way that the peak density of the center tube is approximately $1.2\ n_c$.

2.3.6 Modulation parameters and error bars.

For the data in Fig. 2.2 **a, b, d** we chose the following modulation times and amplitudes: **a** 40 ms, 35%, **b** 40 ms, 30%, **d** 30 ms, 35% for the superfluid phase and 25% for the Mott phase. In Fig. 2.2 **a, b, d**, the error bars for δ reflect the 1σ statistical error. In Fig. 2.2 **c**, the error bars for f_g are derived from the 1σ error on the fit parameters. The error for γ results from the 1σ statistical error of the independent input variables and the spread of γ due to the distribution of tubes. For the data in Fig. 2.4 the error in γ is derived from the 1σ error of the fit parameters for the modulation measurements. For the transport measurements, the error in γ results from the 1σ statistical error of the independent input variables and the spread of γ due to the distribution of tubes.

Part II

Atomic bosonic and fermionic mixtures

Recent experimental advances in trapping and cooling fermionic atomic gases [63, 64, 80, 81, 82, 83, 84, 85, 86] have paved the way to a series of theoretical studies involving not only Fermi gases [87], but also Bose-Fermi(BF), Fermi-Fermi(FF) and multispecies Fermi mixtures [44]. These achievements are of strong interest with respect to various topics in many-body physics. A natural parallelism emerges between two-species Fermi mixtures and electrons in metals: in this case, the spin degree of freedom in embodied in the system by *i)* considering mixtures of different atomic species or *ii)* employing species dependent optical lattices, which affect the tunneling rate of each species in a different way, thus allowing for a complete and almost unconstrained control over all system parameters, included dimensionality of the sample.

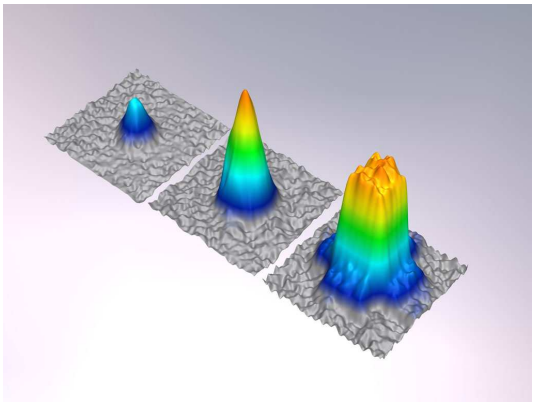

Figure 2.5: **Fermi surface of atoms in an optical lattice**: typical quasi-momentum distribution of a Fermi gas loaded into an optical lattice; from left to right, the number of particles is increased in such a way that atoms in the center of the trap start occupying higher bands. Image taken from Tilman Esslinger's group website.

A particular interest has been devoted to one dimensional systems, where exotic phenomena such as FFLO pairing and spin-charge separation may occur[88]. While in 1D powerful theoretical instruments are at disposal, there are still open problems regarding a variety of fermionic systems, between them being a slight modification of the HM, known as the asymmetric Hubbard model (AHM):

$$H = -\sum_{j\sigma} t_\sigma (c^\dagger_{j\sigma} c_{j+1\sigma} + \text{h.c.}) + U \sum_j n_{j\uparrow} n_{j\downarrow} \tag{2.2}$$

where the hopping coefficients are in general different, $t_\uparrow \neq t_\downarrow$. Differ-

ently with respect to the HM, this model is not exactly solvable; several approaches have been employed to describe its phase diagram, revealing a rich structure which can be in principle observed in cold atom experiments. In the first chapter of this section, we will quantitatively address some open questions regarding its pairing regimes and the so called *phase separation* (PS) phenomena, which have been already observed in the context of 3D FF mixtures [86] [see Fig.2.6]. We will employ two perturbative analytical techniques accompanied by numerical calculations based on the DMRG algorithm, and find out a strong filling dependence of the PS regimes. Then, we will present numerical results which show how exotic phenomena such as true crystals and topological phases can occur in certain parts of the phase diagram: remarkably, these phases were known to be stabilized only in presence of non-local interactions, whereas in our case only a local one in included. This feature shows how the breaking of the $SU(2)$ symmetry related to $t_\uparrow = t_\downarrow$ in the HM can effectively generate non-local interactions, which emerge naturally in perturbative arguments in several models but do not usually influence the underlying effective field theory as they do for the AHM. Let us finally notice that all of these results are also valid (up to a proper rescaling of certain correlation functions) for hard-core Bose-Bose mixtures, which in 1D can be mapped to FF mixture via the so-called *Jordan-Wigner transformation*.

In Chapter 5, we will instead focus on a slightly different subject. It is widely known that ultracold fermionic mixtures suffers from three-body recombination processes, which become considerable in presence of a *Fano-Feshbach resonance*(FR). Once three particles come close to each other, they do interact through a short range potential which, under certain circumstances, can favor the formation of a two-body bound state; the energy released during the process is then partially absorbed by the remaining particle, which is then expelled by the system. A typical example of three-body losses in heterogeneous Fermi mixtures is schematically presented in Fig. 2.7: once a three-species ^{6}Li gas is trapped, the fraction of remaining atoms abruptly changes close to a scattering resonance.

Dissipative processes are thus usually a nasty feature, which may strongly reduce the possibility to observe exotic phases like, e.g., trimer liquids [89, 90]. However, due to the so called *Quantum Zeno effect* [91], a strongly dissipative systems turns out to be effectively stable on short timescales; namely, if the loss rate Γ associate to three-body recombination is much larger than the typical energy scale of the system δ, the number of particles is essentially conserved up to timescales proportional to Γ/δ^2. Taking advantage of this mechanism, Syassen and coworkers have been able to realize a Tonks-Girardeau gas with Feshbach molecules [92], which are

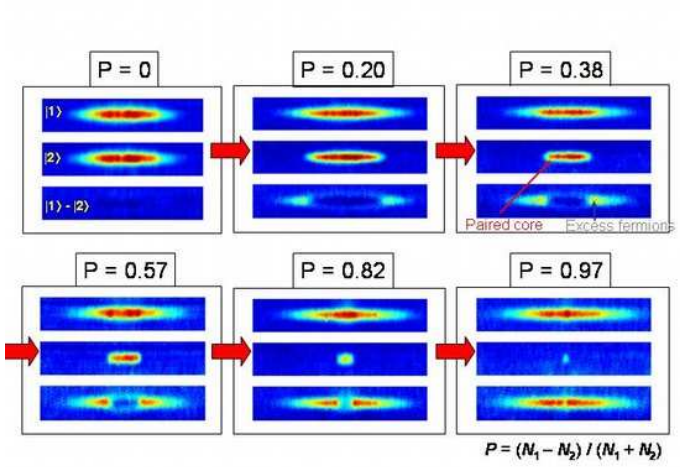

Figure 2.6: **Phase separation in a two-species Fermi gas**: real space density distribution of un unbalanced FF mixture with attractive interactions: phase separation emerges a long as the gas gets polarized[see Ref. [86] for more details]. Image taken from Randy Hulet's group website.

usually unstable towards two-body scattering.

The possibility to use losses as effective many-body interactions has been proposed in [93], considering in detail a standard Bose-Hubbard model. The effect of strong three-body losses in such a system effectively cuts the Hilbert space up to double occupancies, allowing to investigate the attractive regime, usually not accessible because of many-body collapse. Even in this simple case, various interesting phenomena such as a dimer liquid and Ising-type criticality emerge. In Chapter 5, we will illustrate how such three-body effective interactions can give rise to anomalous pairing mechanism in one dimensional three-species gases, stabilizing an *atomic color superfluid* analog to the color flavor locked phase suggested to appear in high-density QCD.

As a final outlook, in Chapter 6 we will present some numerical results on the possibility to realize magnetic phases such as *counter flow superfluidity* and *Néel antiferromagnet* in strongly unbalanced two species bosonic mixtures, giving a particular emphasis on the ^{87}Rb-^{41}K experimental setup developed at LENS.

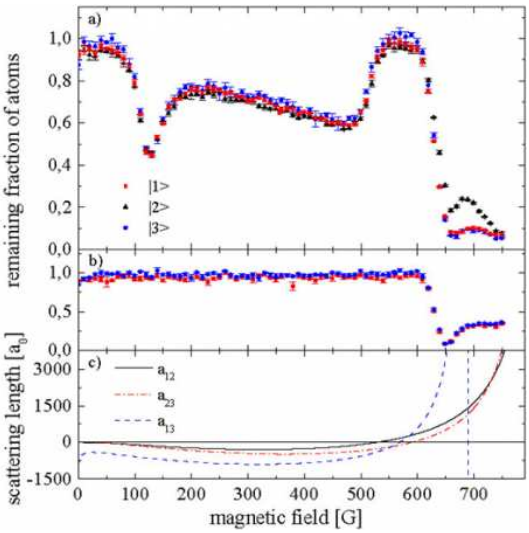

Figure 2.7: **Scattering properties and three-body losses in ^{6}Li**: *a)* remaining fraction of atoms in a three species ^{6}Li mixture after 250 ms as a function of the magnetic field; *b)* same results for a two-species mixture; two-body scattering length for different interspecies interactions; for more details, see [84]. Image taken from the website of Selim Jochim's group.

Chapter 3

Fermi-Fermi mixtures: pairing regimes and phase separation in the asymmetric Hubbard model.

We address some open questions regarding the phase diagram of the one-dimensional Hubbard model with asymmetric hopping coefficients and balanced species. In the attractive regime we present a numerical study of the passage from on-site pairing dominant correlations at small asymmetries to charge-density waves in the region with markedly different hopping coefficients. In the repulsive regime we exploit two analytical treatments in the strong- and weak-coupling regimes in order to locate the onset of phase separation at small and large asymmetries respectively.

3.1 Introduction

In this chapter we study a variation of the one-dimensional Hubbard model (HM) in which the difference between the hopping amplitudes, say $t_\uparrow > t_\downarrow$, is responsible for an explicit breaking of the rotational symmetry. It is described by the Hamiltonian

$$H = -\sum_{j\sigma} t_\sigma (c^\dagger_{j\sigma} c_{j+1\sigma} + \text{h.c.}) + U \sum_j n_{j\uparrow} n_{j\downarrow} \tag{3.1}$$

where $c_{j\sigma}$ denotes the annihilation operator of a fermion with $\sigma = \uparrow, \downarrow$ at site j and $n_{j\sigma} = c^\dagger_{j\sigma} c_{j\sigma}$ are the associated number operators.

This asymmetric Hubbard model (AHM) has been studied in the past [94] to describe the essential features of the metal-insulator transition in rare-earth materials and transition-metal oxides; in this case σ represents

two types of spinless fermions (the real spin being considered not essential for the transition to be modelled). The "light" particles are described by band (Bloch) states, while the "heavy" ones tend to be localized on lattice (Wannier) sites. More recently, this model has gained a renewed interest in experiments with optical lattices, in which both the effective strengths of the kinetic and of the potential parts can be varied in a rather controlled way, including the possibility of reaching the attractive regime $U < 0$. The possibility to use cold atoms [44, 4] to engineer condensed matter systems with a high tunability offers an experimental way to test theoretical results with great accuracy. Two-species models with different hopping coefficients can also be realized by trapping atomic clouds with two internal states of different angular momentum, thereby introducing a spin dependent optical lattice, which enables to modify the ratio $a = t_\downarrow/t_\uparrow$ by controlling the depth of the optical lattice [95]. Yet another possibility is to trap two different species of fermionic atoms, so that the "anisotropy" a is given naturally by the ratio of masses. In the context of cold atoms in optical lattices the subscripts $\sigma = \uparrow, \downarrow$ are not related to the electron spin but label the two different species of fermions, either different atoms with half-integer spin or different excited states of one atomic specie with fine structure splitting.

Many recent papers on the subject are devoted to the onset of the so-called Fulde-Ferrell-Larkin-Ovchinnikov (FFLO) phase, which may occur with *unbalanced* species [96, 97]. In this chapter we will consider instead the case of *balanced* species: $N_\uparrow = N_\downarrow$. The parameters that influence the phase diagram can be cast in the form of an anisotropy coefficient $z = (t_\uparrow - t_\downarrow)/(t_\uparrow + t_\downarrow) = (1-a)/(1+a)$ and a dimensionless onsite potential $u = U/t$, where $t = (t_\uparrow + t_\downarrow)/2$ is an overall energy scale. In addition one can consider the effect of the total filling $n = N/L$, N being the total number of fermions and L the chain length. At variance with the typical situation in condensed matter physics, where the bulk filling and magnetization $m^z = (n_\uparrow - n_\downarrow)/2$ are controlled in a grand-canonical framework by the chemical potential and an external magnetic field respectively, in the context of cold atoms it is conceivable to fix independently the number of particles in each of the two species, despite the fact that only a given choice of the densities $n_\uparrow$ and $n_\downarrow$ might correspond to the absolute minimum of the grand potential. Henceforth we will assume that they are equally populated, that is $n_\uparrow = n_\downarrow = n/2$ and we will limit ourselves to $n < 1$. Note that if $E(n, m^z)$ is the energy in a given sector of n and m^z (these two quantities are good quantum numbers also in the asymmetric case), then a particle-hole transformation $n_{j\sigma} \to (1 - n_{j\sigma})$ leads to $E(2-n, -m^z) = E(n, m^z) - UL(n-1)$, so that for $m^z = 0$ it is

sufficient to analyze the phase diagram for positive and negative U and $n < 1$, in order to infer features also at $n > 1$. The phase diagram at half-filling, $n = 1$, has been studied in ref. [98], soon after the development of White's density-matrix renormalization group (DMRG) method [28]. The limiting case of the symmetric HM ($z = 0$) can be solved exactly via the Bethe *ansatz* approach [99]. The opposite extremal case $z = 1$ is usually called the Falicov-Kimball (FK) model. In any dimensionality, it has been proven [100] that for large *positive* U and $n \neq 1$ the system has a ground state characterized by a spatially non-homogeneous density profile, called phase-separated (PS) state. This phase persists also for $z \lesssim 1$ [101] and can be interpreted as the result of an effective *attractive* interaction between light fermions, mediated by the heavy ones (see [102] in 1D and [103] in 2D). At smaller asymmetries, the system is instead in a more conventional spatially homogeneous phase (HP). The ground state phase diagram for the model in the $m^z = 0$ sector has been discussed in [88] by means of the bosonization approach. In this context [104] the HP-PS transition line at $u > 0$ has been interpreted as the curve in (z, u)-plane where the velocity of one of the two decoupled bosonic modes vanishes.

Let us summarize the content of this chapter. In Sec. 3.2 we will study numerically the attractive regime ($U < 0$), by using a DMRG program. In particular we will examine which kind of correlations (charge or pairing) is dominant in this region of the phase diagram. Then we will move to consider the repulsive ($U > 0$) regime. In Sec. 3.3 we will analytically discuss the weak coupling regime ($|U| \ll t_\sigma$) by means of a variational method that compares the energy of the PS state with that of the HP state, the latter being calculated within a second order perturbation analysis. In Sec. 3.4 we move to study the strong coupling regime ($U \gg t_\sigma$) in order to determine a phase diagram which includes also different types of PS states. The results are summarized and the conclusions are drawn in Sec. 3.5. A cartoon representation of the different phases to which we refer in the following can be found in Fig. 3.1.

3.2 Superconducting properties: singlet-pairing to charge-density wave transition at $U < 0$

One of the open points raised in ref. [88] is the existence of regions at $U < 0$ characterized by dominating charge-density wave (CDW) correlations instead of the singlet-superconducting (SS) ones that one has in the attractive symmetric HM. On a lattice the CDW and the SS correlation functions are

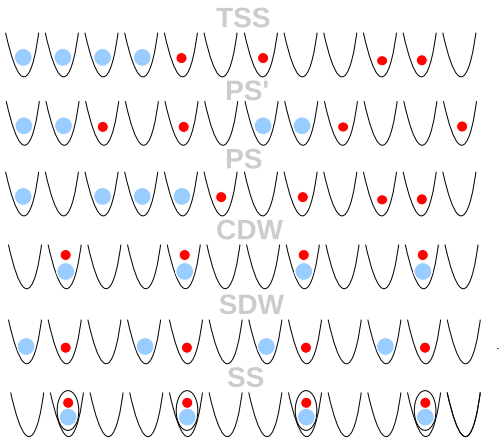

Figure 3.1: Schematic representation of the phases discussed in the text. Large and small disks represent heavy and light fermions respectively. The ellipsis encircling the pairs in the SS phase denotes onsite pairing.

defined respectively as

$$C(r) = \langle n_j n_{j+r} \rangle - \langle n_j \rangle \langle n_{j+r} \rangle$$

$$P(r) = \langle \eta_j^\dagger \eta_{j+r} \rangle$$

where $n_j = n_{j\uparrow} + n_{j\downarrow}$ while $\eta_j = c_{j\downarrow} c_{j\uparrow}$ is the operator that destroys an onsite pair with singlet spin wavefunction. At large distances r, bosonization procedures predict [11]

$$C(r) \sim \frac{-K_\rho}{\pi^2 r^2} + A \frac{\cos(2k_F r)}{r^{K_\rho + K_\sigma}}$$

$$P(r) \sim \frac{B}{r^{1/K_\rho + K_\sigma}}$$

where A and B are constants, and K_ρ and K_σ are the Luttinger parameters for the charge and spin degrees of freedom respectively. Clearly $C(r)$ dominates over $P(r)$ when $K_\rho < 1$, while K_σ has to be fixed to 0 for gapped spin phases. A numerical estimate of K_ρ from finite-size data can be obtained as in ref. [105] by considering the structure factor

$$S(q) = \sum_r \mathrm{e}^{\mathrm{i}qr} \langle n_j n_{j+r} \rangle$$

Here we have dropped the dependence on j because we implicitly assume that the correlation functions are translationally invariant due to periodic boundary conditions (PBC). The value $S(q = 0)$ corresponds to the

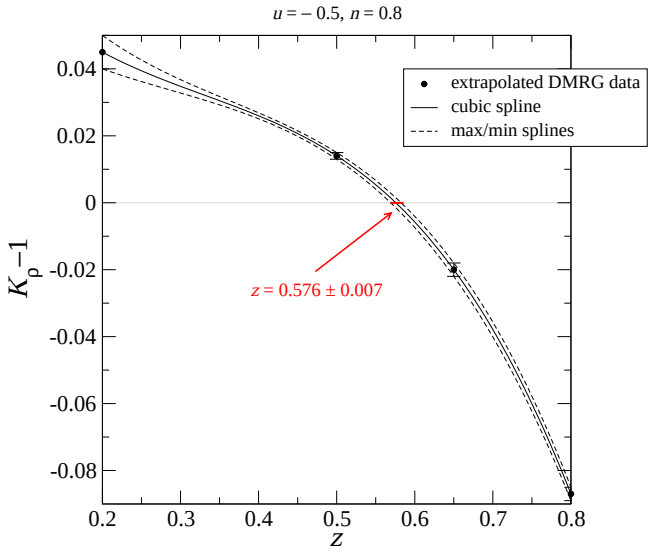

Figure 3.2: Example of cubic splines interpolation to locate the transition point and the associated error, using the DMRG data of table 3.1. The horizontal solid segment at $K_\rho = 1$ indicates the reported interval.

average correlation and it diverges in the thermodynamic limit, since typically $\langle n_j n_{j+r} \rangle$ saturates at a finite value n^2 for large distances. So one may consider the connected charge correlation $C(r)$ in order to avoid this divergence. This choice affects the structure factor only at $q = 0$ and bosonization predicts that the value of K_ρ is directly related to the *limit* $q \to 0$

$$S(q) \simeq K_\rho \frac{q}{\pi} + \dots$$

Following the procedure of ref. [105] by selecting the smallest possible non-vanishing momentum compatible with PBC $q_1 = 2\pi/L$ one builds a sequence that approximates the linear slope

$$K_\rho(L) = S(q_1)\frac{L}{2}.$$

The dependence on L indicates that the sequence has to be extrapolated to $L \to \infty$ in order to obtain the limit $q \to 0$ and the parameter K_ρ. The DMRG results corresponding to various fillings $n = 0.4,\ 0.6,\ 0.8$ with $z = 0.2,\ 0.5,\ 0.65,\ 0.8$ and $u = -0.001,\ -0.5,\ -3$ are reported in table 3.1; in the caption we have reported also the relevant features of our DMRG numerical calculations. For a fixed value of $u < 0$ we always find that the extrapolated K_ρ decreases with increasing z. From this grid of points we can have an idea of the SS-CDW transition curve by locating the points at which $K_\rho = 1$. This has been done interpolating the data with splines. An example of this procedure is given in Fig. 3.2, while the global results are plotted in Fig. 3.3.

$u \setminus z$		0.2	0.5	0.65	0.8
	$n = 0.4$				
-10^{-3}		$1.001 \pm 0.002^{\ddagger}$	$0.9978 \pm 0.0002^{*}$	$0.994 \pm 0.001^{*}$	$0.986 \pm 0.004^{*}$
-0.5		1.0700 ± 0.0004	1.038 ± 0.001	0.992 ± 0.002	0.906 ± 0.003
-3		1.4209 ± 0.0005	1.2528 ± 0.0003	1.0976 ± 0.0002	0.86715 ± 0.00005
	$n = 0.6$				
-10^{-3}		$1.0034 \pm 0.0008^{*}$	$1.001 \pm 0.001^{\ddagger}$	$1.000 \pm 0.002^{\ddagger}$	$0.998 \pm 0.004^{\ddagger}$
-0.5		$1.050 \pm 0.001^{\ddagger}$	$1.04 \pm 0.01^{\ddagger}$	$1.03 \pm 0.02^{\ddagger}$	$1.00 \pm 0.05^{\ddagger}$
-3		1.26016 ± 0.00007	1.110 ± 0.003	0.969 ± 0.004	0.751 ± 0.004
	$n = 0.8$				
-10^{-3}		$1.008 \pm 0.002^{*}$	$0.9976 \pm 0.0001^{*}$	0.983 ± 0.005	0.951 ± 0.009
-0.5		$1.045 \pm 0.005^{\ddagger}$	1.014 ± 0.001	0.980 ± 0.002	0.913 ± 0.002
-3		1.1603 ± 0.0001	1.0163 ± 0.0008	0.880 ± 0.001	0.6722 ± 0.0008

Table 3.1: Extrapolations for the parameter K_ρ from DMRG simulations with PBC, $L = 10, 20, 30, 40, 50$, 1100-1300 optimized states and seven finite-system sweeps. This conservative choice guarantees an energy relative error of $O(10^{-6})$ up to $L = 30$ and $O(10^{-5})$ up to $L = 50$ (recall that the charge degrees of freedom are always gapless). Unless otherwise specified the extrapolations have been performed using quadratic fits in $1/L$ and the error bars are evaluated according to [106] (Chapter 15) using the sum of squared differences normalized to the fit degrees of freedom as a measure of the spread in the ordinates. ‡: Oscillating about reported value with spread. *: Linear fit in $1/L$.

In ref. [88] (Fig. 1 therein) the authors report a triangular region obtained by means of bosonization at $u < 0$ where the dominant correlations are CDW or SS depending on the filling. Here we observe that the shape of the transition line is indeed dependent on n: for $u < -0.5$ the separation line might have both a negative and a positive slope, depending on the value of n. For small (negative) u the curve has always a negative slope. Because of the uncertainty related to DMRG and finite-size effects, our estimate of the transition points is limited to $u \leq -10^{-3}$; moving closer to $u = 0$ would produce values of K_ρ essentially always equal to 1 within the numerical error, for all values of z, so we have not pushed our analysis and conclusions closer to $u = 0$.

Finally we should mention that a direct inspection of the charge correlation functions in real and in Fourier space reveals that the only characteristic wavenumber is $2k_F = \pi n$, where typically the structure factor

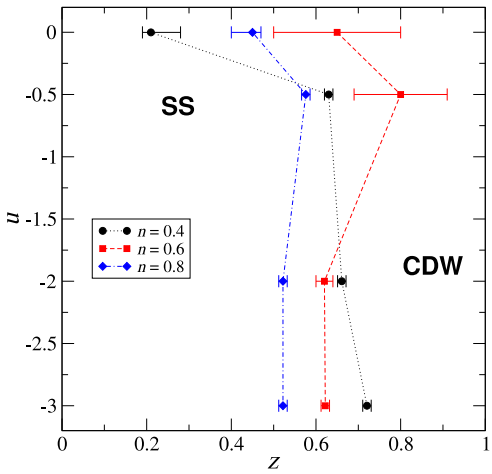

Figure 3.3: Numerical estimates of the transition lines from SS (on the left) to CDW (on the right) dominant correlations in the attractive regime for the values of filling reported in the legend. Not all the data used to obtain the figure have been reported in table 3.1. The error bars associated to the transition point have been determined by means of splines passing through the upper and lower edges of each interval of possible values of K_ρ reported in the table (see the construction of Fig. 3.2); when the uncertainty in z turned to be smaller than 10^{-2} we have conventionally set it to this value to account for the approximation introduced by cubic splines interpolation. The lines joining the points are guides to the eye.

displays a peak for $u < 0$, but there is neither FFLO behavior - as expected since we have selected balanced species - nor a collapse (predicted at sufficiently large negative u [107]).

3.3 Phase separation in the weak-coupling limit

From a quantitative point of view, bosonization cannot be conclusive about the location of the HP to PS transition at $z \cong 1$. This is due to the fact that, while a continuum limit approach is justified close to $z = 0$, in the FK limit even a small U can involve processes away from the Fermi surface, and so the requirement $|U| \ll \min[t_\uparrow, t_\downarrow]$ strictly reduces the range of reliably of

this approach[88].

Numerical data [108] indicate that in the highly asymmetric regime phase separation appears above a critical value of U which approaches zero in the low-density limit.

When approaching the FK limit $z \to 1$, the kinetic energy of the lighter species becomes the dominant term of the Hamiltonian at weak coupling, $U \ll t_\uparrow$. For $U > 0$, the competition between the light particle kinetic energy and the repulsive on-site interaction can drive the system into an instability with respect to phase separation [101]: there exists a critical value $u_{PS}(z, n)$ above which light particles will occupy a large region of the system where $n_{i\downarrow} = 0$, creating an effective pressure which confines heavy particles into a small region with density close to 1; this effect is reminiscent of the phase separated regime present in the FK model in the repulsive regime.

Different numerical and analytical methods have been proposed in literature to identify this phase transition between the HP and the PS regimes [104, 109, 108]. In the following, we will (*i*) apply a second order perturbation theory approach, first introduced [110] to study the ground state of the weakly interacting symmetric HM, to compute the energy of a homogeneous phase ground state of the AHM and (*ii*) compare HP and PS state energies in order to detect the line of quantum phase transition as a function of the original model parameters z, u, n. Finally, a comparison with previous results will be presented.

3.3.1 Trial wave functions

In the low coupling regime, we can consider as extended ground state the exact one at $U = 0$ (and $t_\downarrow \neq 0$), which can be obtained by filling both Fermi bands up to $k_{F\sigma}$:

$$|\Psi\rangle_{HP} = \prod_{|q|\leq k_{F\downarrow}} \tilde{c}^\dagger_{q\downarrow} \prod_{|k|\leq k_{F\uparrow}} \tilde{c}^\dagger_{k\uparrow}|0\rangle \tag{3.2}$$

where $|0\rangle$ represents the zero-fermions vacuum and $\tilde{c}^\dagger_{k\sigma}$ are the creation fermionic operators in Fourier space. While $|\psi\rangle_{HP}$ is not an exact eigenstate of the full Hamiltonian, perturbation theory above this ansatz have provided excellent results for $z = 0$ [110], where a comparison with the exact solution is possible, and, as shown later in the section, even in the highly asymmetric regime.

The PS ground state instead can be obtained in the following way: first, we confine all heavy particles in a given part of the lattice of relative length

ν, with $(L - N_\uparrow)/L \geq \nu \geq N_\downarrow/L$; then we consider two different chains of length $L_\downarrow = \nu L,\ L_\uparrow = L(1-\nu)$ respectively and then fill the new Fermi bands till the momenta $k'_{F\sigma} = \pi N_\sigma / L_\sigma$:

$$|\Psi(\nu)\rangle_{PS} = \prod_{|q'|\leq k'_{F\downarrow}} \tilde{c}^\dagger_{q'\downarrow} \prod_{|k'|\leq k'_{F\uparrow}} \tilde{c}^\dagger_{k'\uparrow}|0\rangle.$$

In practice we have to consider that the effective light-particle and heavy-particle "chain lengths" are not L but $L(1-\nu)$ and $L\nu$, respectively.

In addition, we can define a *totally segregated state* (TSS) as the one with a completely full region of heavy particles, i.e. $\nu = N_\downarrow/L$. In this case, the variational wave function can be written as:

$$|\Psi\rangle_{TSS} = \prod_{(1-n_\downarrow)L<j<L} c^\dagger_{j\downarrow} \prod_{|k'|\leq k'_{F\uparrow}} \tilde{c}^\dagger_{k'\uparrow}|0\rangle.$$

where now the down-fermion creation operators are taken in real space representation. Both TSS and PS state trial wave functions are eigenstate of the Hamiltonian up to a boundary term which we neglect in the following $L \to \infty$ limit.

3.3.2 Ground state energies

The instability of a homogeneous ground state towards a phase separated one can be analyzed by computing the corresponding zero temperature energy:

$$\mathcal{E}_{PS} = \frac{{}_{PS}\langle\Psi|H|\Psi\rangle_{PS}}{L}, \quad \mathcal{E}_{HP} = \frac{{}_{HP}\langle\Psi|H|\Psi\rangle_{HP}}{L}$$

and by comparing them to get the phase transition hypersurface in parameter space described by:

$$\mathcal{E}_{PS}(n_\uparrow, n_\downarrow, U, z) - \mathcal{E}_{HP}(n_\uparrow, n_\downarrow, U, z) = 0$$

A similar criterion can be applied to distinguish between TSS and PS state without segregation, as described later in the section. We remark that in the PS region, due to the fact that within the two subchains of length $L_{\uparrow,\downarrow}$ the up and down particles do not overlap, the interaction term provides at most a boundary contribution which can be neglected in the thermodynamic limit. We will come back to this point later.

We can then compute the PS state energy density $\mathcal{E}_{PS}$ considering only the kinetic term contribution. For a general ν, the result is

$$\mathcal{E}_{PS}(\nu) = -t(1+z)\frac{2(1-\nu)}{\pi}\sin\left(\frac{\pi n_\uparrow}{1-\nu}\right) \tag{3.3}$$

$$-t(1-z)\frac{2\nu}{\pi}\sin\left(\frac{\pi n_\downarrow}{\nu}\right)$$

As already stated in [101] (in particular Sec. 3 therein), it is possible to fix the lowest energy state with respect to ν searching for a minimum of (3.3) at fixed densities and hopping rates. The corresponding condition $\partial_\nu \mathcal{E}_{PS} = 0$ becomes

$$\begin{aligned}(1+z)\sin\left(\frac{\pi n_\uparrow}{1-\nu}\right) - \frac{\pi n_\uparrow}{1-\nu}\cos\left(\frac{\pi n_\uparrow}{1-\nu}\right) \\ = (1-z)\left[\sin\left(\frac{\pi n_\downarrow}{\nu}\right) - \frac{\pi n_\downarrow}{\nu}\cos\left(\frac{\pi n_\downarrow}{\nu}\right)\right]\end{aligned} \tag{3.4}$$

If there exists a value of ν, ν^* with $1-n_\uparrow > \nu^* > n_\downarrow$, which satisfies this condition, then the lowest energy state is $|\Psi(\nu^*)\rangle_{PS}$; otherwise, the minimum of $\mathcal{E}_{PS}$ lies on the boundary $\nu^* = n_\downarrow$ and TSS is energetically more favorable. The boundary between these two regions is described by the condition $\partial\mathcal{E}_{PS}/\partial\nu|_{\nu=n_\downarrow} = 0$; the solution of this equation provides a characteristic anisotropy coefficient $\bar{z}$ for given $n_{\uparrow,\downarrow}$ that turns out to be independent of u. We expect that $\bar{z}$ represents a good estimate for the phase transition between TSS and $\nu \neq n_\downarrow$ states even at intermediate couplings. In fact, we find good agreement with the values corresponding to the (almost) horizontal lines plotted in Fig. 3 of ref. [108].

As said before, here we consider only the balanced case $n_\uparrow = n_\downarrow = n/2$, for which the condition that yields the optimal $\nu = \nu^*(z)$ in the range $\nu \in (n/2, 1-n/2)$ simplifies to

$$z = \frac{f\left(\frac{\pi n}{2\nu}\right) - f\left(\frac{\pi n}{2(1-\nu)}\right)}{f\left(\frac{\pi n}{2\nu}\right) + f\left(\frac{\pi n}{2(1-\nu)}\right)} \tag{3.5}$$

with $f(x) = \sin x - x\cos x$. The upper limit for ν is formally obtained by compressing the up-electrons so that $1-\nu = n/2$. When $\nu = 1/2$ the numerator of the right-hand side vanishes and z reaches the minimum possible value $z = 0$. When $\nu = \nu_{min} = n/2$ the right-hand side has the value

$$\bar{z}(n) = \frac{\pi - f(\pi n/(2-n))}{\pi + f(\pi n/(2-n))}.$$

This function decreases monotonically with the filling from $\bar{z}(0) = 1$ to $\bar{z}(1) = 0$. If $z \geq \bar{z}(n)$, the minimum energy is attained at the lower limit $\nu^* = n/2$, corresponding to maximum compression of the down-fermions, independently of value of z. Clearly, high densities favor a TSS state, since a large amount of light particles produce a sufficient pressure in order to

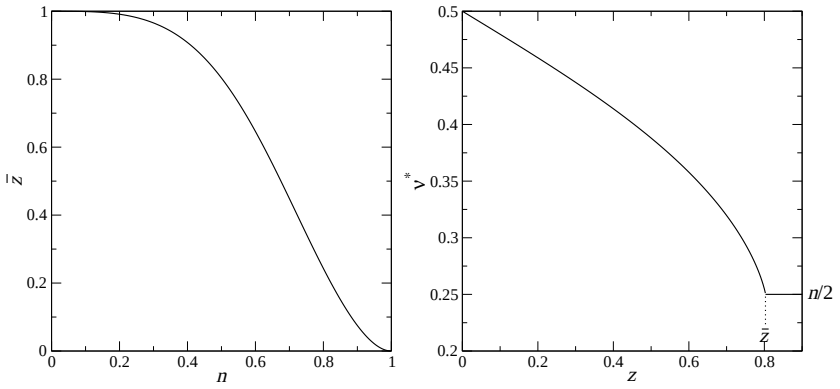

Figure 3.4: Right panel: Plot of the function $\bar{z}(n)$. Left panel: Optimal value of ν as a function of z in the whole interval $[0, 1]$ for filling $n = 1/2$.

compress all heavy particles in a very small region. When the density is low enough, this condition cannot be satisfied, except at very large mass imbalances, and heavy particles still contribute to the kinetic energy of the system. Fig. 3.4 shows an example of such a construction for $n = 1/2$.

The energy density of the HP state receives instead both kinetic and interaction contributions: $\mathcal{E}_{HP} = \mathcal{E}_T + \mathcal{E}_U$. The kinetic part is equivalent to the ground state energy density of the non-interacting case

$$\mathcal{E}_T = -t(1+z)\frac{2}{\pi}\sin(\pi n_\uparrow) - t(1-z)\frac{2}{\pi}\sin(\pi n_\downarrow) \tag{3.6}$$

whereas the interacting part in the weak coupling limit can be expressed as a series in U applying a second order perturbation theory [110]:

$$\mathcal{E}_U = \frac{1}{L}\,{}_{HP}\langle\Psi|H_U|\Psi\rangle_{HP}$$
$$+\frac{1}{L}\left({}_{HP}\langle\Psi|H_U\frac{1}{\mathcal{E}_T - H_0}H_U|\Psi\rangle_{HP}\right)_{\text{conn}} + \mathcal{O}(U^3)$$

where $(...)_{\text{conn}}$ indicates a sum over connected diagrams and H_0 denotes the unperturbed Hamiltonian. The first order contribution is obtained rewriting the number operators in momentum space, thus obtaining

$${}_{HP}\langle\Psi|H_U|\Psi\rangle_{HP} = LUn_\uparrow n_\downarrow \tag{3.7}$$

while the second order contribution can be computed evaluating Goldstone diagrams:

$$\mathcal{E}^{(2)}_{HP} = -\frac{U^2}{t(2\pi)^3}\frac{\vartheta(k_{F\uparrow}, k_\downarrow, a)}{(1+z)} \tag{3.8}$$

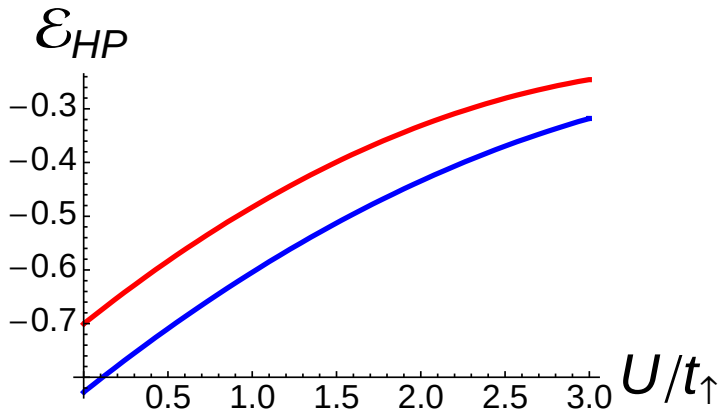

Figure 3.5: Energy density of the HP state at $n = 1$ for different asymmetry parameters: upper red line $t_\downarrow/t_\uparrow = 0.1$, lower blue line $t_\downarrow/t_\uparrow = 0.3$.

$$\vartheta(k_{F\uparrow}, k_\downarrow, a) \equiv \int_0^{\frac{\pi}{2}} \frac{dq}{\sin q} \int_{-q}^{q} dk \times$$
$$\times \int_{-q}^{q} \frac{dk'}{\sin(k + k_{F\uparrow}) + a \sin(k' + k_{F\downarrow})}.$$

Integrating the previous expression numerically, we can give a quantitative estimate of the phase boundary near the FK limit. Furthermore, by comparing $\mathcal{E}_{HP}$ up to second order (plotted in Fig. 3.5) with previous numerical results [108], we have a good check that at half filling the variational ground state (3.2) is a correct description of the system even at finite $U/t_\uparrow \leq 3$.

3.3.3 Phase boundaries

The weak-coupling phase diagram is generally characterized by two types of phase transition: one between the HP state and the PS region, and the other one between different types of PS states.

Combining Eqs.(3.3), (3.6), (3.7) and (3.8), the first mentioned phase transition line is determined by the equation:

$$2 \sin\left(\frac{\pi n}{2}\right) - (1+z)\frac{2-n}{2} \sin\left(\frac{\pi n}{2-n}\right) =$$
$$\frac{\pi}{2} u \left[\frac{n^2}{4} - u \frac{\vartheta(k_{F\uparrow}, k_{F\uparrow}, a)}{(2\pi)^3 (1+z)}\right] \tag{3.9}$$

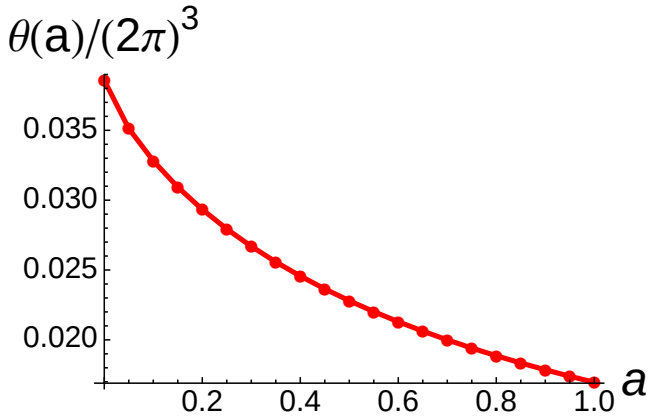

Figure 3.6: Second-order perturbative contribution at half filling $\vartheta(\pi/2, \pi/2, a)/(2\pi)^3$ for different values of a; solid line is a guide for the eye.

Table 3.2 shows how the correlated energy factor depends on $k_{F\uparrow}$ and $z = (1-a)/(1+a)$. In general, the larger the asymmetry z is (the smaller is a) the larger is ϑ. An illustrative plot at half-filling is presented in Fig. 3.6. Furthermore ϑ approaches 0 in the low-density limit and grows with the filling.

$a \backslash k_{F\downarrow} = \pi n/2$	$\pi/3$	$\pi/4$	$\pi/6$
0.01	0.028	0.022	0.013
0.05	0.027	0.021	0.012
0.1	0.026	0.02	0.012
0.15	0.025	0.019	0.012
0.2	0.024	0.018	0.011

Table 3.2: Numerical values for $\vartheta(k_{F\uparrow}, k_{F\uparrow}, a)/(2\pi)^3$ below half filling. Notice that the term $(1+z)$ in the denominator of Eq. (3.8) has not been included in the definition of ϑ so to have a more direct comparison with ref. [110].

We will consider first the case when the density is medium-high: $n_\uparrow = n_\downarrow = n/2 > 0.25$, when a transition from HP to TSS state should always take place, being $\nu^* > n/2$ unfavored. By inspecting Eq. (3.9) it turns out that the ground state in the weak coupling limit is always homogeneous, even for large z ($a < 0.2$, i.e. $z > 2/3$). This fact agrees with pre-

vious numerical results [108] showing that the TSS phase is present only for $U/t_\uparrow \gtrsim 2.5$. Even close to quarter filling, the phase transition in the FK limit is predicted at $U/t_\uparrow = 1.15$, which is beyond the weak coupling regime we are considering in this section.

Let us examine now the low density regime: $n_\uparrow = n_\downarrow = n/2 < 0.25$, where the TSS might be the ground state only at very small a. Now we have to determine the transition point from HP to TSS state in the FK limit (a very small) as well as to explore the possibility of a transition to a PS state with $\nu > n_\downarrow$ for larger values of a. We will examine first the $n = 1/3$ case as an example. In the highly asymmetric regime ($a < 0.01$, i.e. $z > 0.98$), we again find a transition from a HP to a TSS state which happens for values of $U(n = 1/3)/t_\uparrow \sim 0.3$. As explained in the previous section, using Eqs. (3.3) and (3.4) we can determine the phase transition line between TSS and a PS state with $\nu \neq n_\downarrow$. This transition occurs for $t_\downarrow(n = 1/3)/t_\uparrow \sim 0.025$, a value which turns out to be independent of U since no contributions from the correlation energy are present. These transition points are in good accordance with the numerical results reported in [108], and allow us to complete a general weak coupling phase diagram in the highly asymmetric regime for $n = 1/3$, which is shown in Fig. 3.7. At smaller densities, the critical value $U(n)/t_\uparrow$ at which one finds the transition from the HP to the TSS state becomes smaller. For example $U(n = 1/6)/t_\uparrow \sim 0.06$, while $U(n = 1/12)/t_\uparrow \lesssim 10^{-3}$. We notice that it is impossible, within our perturbative approach (see Eq. (3.9)), to find for this coefficient a value equal to zero: its value decreases as n becomes smaller but stays always finite, going to zero smoothly as n tends to zero. In addition, the TSS is always unstable with respect to a PS one, the transition now appearing at lower asymmetries ($t_\downarrow(n = 1/6)/t_\uparrow \sim 2.5 \times 10^{-3}$, $t_\downarrow(n = 1/12)/t_\uparrow \sim 2.7 \times 10^{-4}$), whose values are still essentially insensitive to U.

3.4 Phase separation in the strong-coupling limit

In this section we analyze the case of strong repulsive onsite interaction between fermions, corresponding to $t_\sigma \ll U$, a regime which is of particular interest for the experimental realization of the symmetric ($z = 0$) model in a cold atom system [63], in which a Mott-insulator phase at half filling was found. One of the questions left open by bosonization is what happens to the HS-PS transition curve close to $z = 0$. From the phase diagrams in refs. [88] and [107] it is not clear whether it approaches a finite value when $z \to 0$ or, conversely, if there is a characteristic value of $z \neq 0$ at which it

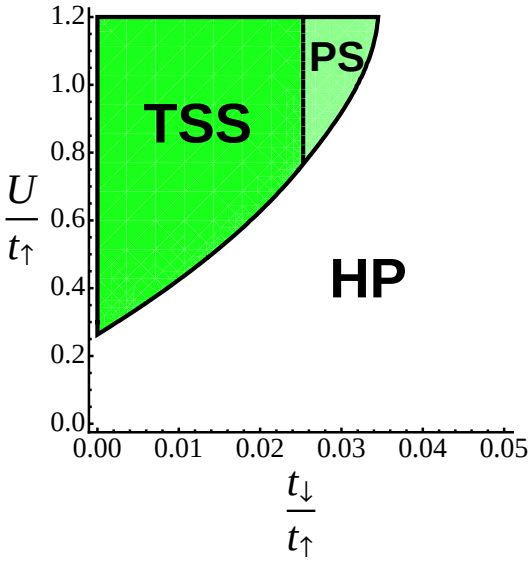

Figure 3.7: Weak-coupling phase diagram with $n = 1/3$: white region represents the homogeneous state (HP), green regions are different phase separated states. The phase transition lines are computed using Eq. (3.4) (dashed) and Eq. (3.9) (solid). In this section we have adopted the parameters $U/t_\uparrow = u/(1+z)$ and $a = t_\downarrow/t_\uparrow = (1-z)/(1+z)$ instead of u and z to facilitate the comparison with previous results in the weak-coupling region.

diverges, as indicated also by some data on short sizes in ref. [111] (Sec. IV therein). To study this regime, we will construct an effective Hamiltonian that is able to describe the AHM when the parameter t can be considered as a small perturbation with respect to U, for a generic filling, by using the method of the flow equations, developed by Wegner [112] and applied to the HM in [113]. The advantages of using such a technique are extensively described in [113]. We only remark here that it yields a very general procedure which, in a recursive way, allows to find an effective Hamiltonian at any order of perturbation, for arbitrary fillings and geometries.

We start by decomposing the fermionic Hilbert space of the model into the subspaces $\mathcal{H}_k$ with exactly k fermionic pairs (double occupancies): $\mathcal{H} = \oplus_{k=0}^{N/2}\mathcal{H}_k$. The projectors P_k on these subspaces are defined via the generating function

$$\sum_{k=0}^{N} P_k x^k = \prod_{i\in L}\left[1-(1-x)n_{i\uparrow}n_{i\downarrow}\right].$$

The kinetic energy term for the spin σ fermions, $T_\sigma = \sum_{<ij>} c^\dagger_{i\sigma}c_{j\sigma}$, can be decomposed into three parts $T_\sigma = T_{0\sigma}+T_{+1\sigma}+T_{-1\sigma}$, which change the number of pairs by $\delta k = m = 0, +1, -1$. In other words: $T_{m\sigma} = \sum_{k=0}^{N} P_{k+m}T_\sigma P_k$. In these expressions, we have introduced the sum over $< ij >$ which de-

notes nearest-neighbors sites i and j (with the couples ij and ji counted once each) since the procedure we are going to discuss is generalizable to any dimension. More explicitly:

$$T_{0\sigma} = \sum_{<ij>} \left[n_{i\bar{\sigma}} c^{\dagger}_{i\sigma} c_{j\sigma} n_{j\bar{\sigma}} + (1 - n_{i\bar{\sigma}}) c^{\dagger}_{i\sigma} c_{j\sigma} (1 - n_{j\bar{\sigma}}) \right]$$
$$T_{+1\sigma} = \sum_{<ij>} n_{i\bar{\sigma}} c^{\dagger}_{i\sigma} c_{j\sigma} (1 - n_{j\bar{\sigma}})$$
$$T_{-1\sigma} = \sum_{<ij>} (1 - n_{i\bar{\sigma}}) c^{\dagger}_{i\sigma} c_{j\sigma} n_{j\bar{\sigma}}$$

It is not difficult to verify that $[N_d, T_{m\sigma}] = m T_{m\sigma}$, where $N_d = \sum_i n_{i\uparrow} n_{i\downarrow}$, reflecting the transition from the Hilbert space $\mathcal{H}_k$ to $\mathcal{H}_{k+m}$. To discuss higher-order interactions terms, it is useful to introduce products of hopping operators, $T^{(k)}_{\sigma_1 ... \sigma_k}(\mathbf{m}) = T_{m_1\sigma_1} ... T_{m_k\sigma_k}$ with the index vector $\mathbf{m} = (m_1, m_2, ..., m_k)$. It is found that the commutator of such an operator product with N_d involves the total weight of the product, $M(\mathbf{m}) = \sum_{i=1}^{k} m_i$, and generally reads $\left[N_d, T^{(k)}_{\sigma_1 ... \sigma_k}(\mathbf{m}) \right] = M(\mathbf{m}) T^{(k)}_{\sigma_1 ... \sigma_k}(\mathbf{m})$. We want now to find an effective Hamiltonian which does not mix the different Hilbert space sectors $\mathcal{H}_k$, i.e. which conserves the total number of local pairs, thus suited to study physical properties at energy and temperature scales which are well below the Hubbard energy $|U|$. To do so, we consider a continuous unitary transformation which allows to remove interactions with non-vanishing overlap between different Hilbert space sectors. Thus, the transformed Hamiltonian depends on a continuous flow parameter l:

$$H(l) = -\sum_{\sigma} t_{\sigma} \Theta_{\sigma}(l) + U N_d$$

where the generalized kinetic energy term $\Theta_{\sigma}(l)$ contains all order interactions which are generated by the transformation:

$$\Theta_{\sigma}(l) = \sum_{k=1}^{\infty} \frac{t_{\sigma}^{k-1}}{U^{k-1}} \sum_{\{\mathbf{m}\}} F^{(k)}_{\sigma_1 ... \sigma_k}(l; \mathbf{m}) T^{(k)}_{\sigma_1 ... \sigma_k}(\mathbf{m}) \tag{3.10}$$

Here $F^{(k)}_{\sigma_1 ... \sigma_k}$ denote suitable coupling functions that have to be determined by asking that the unitary transformation cancels all terms that do not conserve the number of local pairs. The flow equations for these coupling functions follow from the equation of the flow for the Hamiltonian [112]:

$$\frac{dH(l)}{dl} = [\eta_{\sigma}(l), H(l)] \tag{3.11}$$

which has been written here by using the (antihermitean) generator of the transformation

$$\eta_\sigma(l) = \frac{t_\sigma}{U}\,[V, \Theta_\sigma(l)] =$$

$$= \sum_{k=1}^{\infty} \frac{t_\sigma^k}{U^k} \sum_{\{\mathbf{m}\}} M(\mathbf{m}) F^{(k)}_{\sigma_1 \ldots \sigma_k}(l;\mathbf{m}) T^{(k)}_{\sigma_1 \ldots \sigma_k}(\mathbf{m})$$

Now, after imposing both the initial conditions ($F^{(1)}_{\sigma_1}(0;m) = 1$ and $F^{(k)}_{\sigma_1 \ldots \sigma_k}(0;\mathbf{m}) = 0$ for $k > 1$) and the symmetries related to hermiticity and particle-hole transformation $c^\dagger_{i\sigma} \to c_{i\sigma}$, which reverses the sign of the hopping term, one can recast the original flow equation (3.11) in a recursive set of coupled nonlinear differential equations. From these equations it is easy to see that all the terms which connect different sectors of the Hilbert space vanish in the limit $l \to \infty$. At the second order we find that the effective Hamiltonian reads as:

$$\begin{aligned} H_{s-c} = & -t_\uparrow \sum_{<ij>} \Big[n_{i\downarrow} c^\dagger_{i\uparrow} c_{j\uparrow} n_{j\downarrow} + (1 - n_{i\downarrow}) c^\dagger_{i\uparrow} c_{j\uparrow} (1 - n_{j\downarrow}) \Big] \\ & -t_\downarrow \sum_{<ij>} \Big[n_{i\uparrow} c^\dagger_{i\downarrow} c_{j\downarrow} n_{j\uparrow} + (1 - n_{i\uparrow}) c^\dagger_{i\downarrow} c_{j\downarrow} (1 - n_{j\uparrow}) \Big] \\ & + J \sum_{<ij>} \Big[S^x_i S^x_j + S^y_i S^y_j + \Delta (S^z_i S^z_j - n_i n_j / 4) \Big] + U N_d \end{aligned} \tag{3.12}$$

where $S^{x,y,z}_i$ are the spin operators at site i, $J = 2t_\uparrow t_\downarrow / U$ and $\Delta = (t^2_\uparrow + t^2_\downarrow)/2t_\uparrow t_\downarrow \geq 1$. At half filling, $n = 1$, we get, in according to Takahasi's theorem [114], that the terms corresponding to the odd orders of the expansion (in the our case the first two lines) vanish and we find the same Hamiltonian obtained in [98] representing a spin chain with an anisotropy term $\Delta \geq 1$ along the $z-$axis (XXZ chain): the spin excitations are gapped and the spin-spin correlators decay exponentially with the distance. Also, in the limit $t_\uparrow = t_\downarrow$ (symmetric HM) the anisotropy term Δ becomes 1 and we find the well-known Heisenberg Hamiltonian (XXX chain), as it should be.

It is well known [98] that for $z > 0$ the system is in the Néel-like phase, with non-vanishing charge and spin gap and true long-range order. Here we are interested in examining the two limiting cases $z = 1$ (FK model) and $z = 0$ (Hubbard model) to study, more precisely, (i) the phase appearing in the Hubbard model when $U \to \infty$, i.e. the so called spinless fermions phase (SF), where the orientation of the spins loses its relevance since the doubly occupied sites are strictly forbidden, and (ii) the PS state predicted in the FK model where the two fermionic species are demixed.

3.4.1 Spinless fermions

The SF state $|\Psi\rangle_{SF}$ of the Hubbard model in the limit $U \to \infty$ at filling $n = N/L \leq 1$ and equally populated species $n_\uparrow = n_\downarrow = n/2$ is rotationally invariant and invariant under the up-down exchange. In this case, the expectation value of the hopping terms of the Hamiltonian (3.12) reads as follows

$$
\begin{aligned}
{}_{SF}\langle\Psi|[-t\sum_{j,\sigma}(c^\dagger_{j\sigma}c_{j+1\sigma}+\text{h.c.})-tz\sum_j(c^\dagger_{j\uparrow}c_{j+1\uparrow}+\text{h.c.}) \\
+tz\sum_j(c^\dagger_{j\downarrow}c_{j+1\downarrow}+\text{h.c.})]|\Psi\rangle_{SF}=-\frac{2t}{\pi}\sin(\pi n)
\end{aligned}
$$

As for the J-terms, we can borrow directly its expression from (A3) of [115]:

$$
\frac{{}_{SF}\langle\Psi|\sum_j n_j n_{j+1}|\Psi\rangle_{SF}}{L}=n^2-\frac{\sin^2(\pi n)}{\pi^2} \tag{3.13}
$$

Moreover, since $|\Psi\rangle_{SF}$ is SU(2)-invariant, we can write

$$
\frac{{}_{SF}\langle\Psi|\sum_j S^\alpha_j S^\alpha_{j+1}|\Psi\rangle_{SF}}{L}=\frac{1}{3}\frac{{}_{SF}\langle\Psi|\sum_j \vec{S}_j\cdot\vec{S}_{j+1}|\Psi\rangle_{SF}}{L} \tag{3.14}
$$

for $\alpha = x, y, z$ even if the J-part in the strong-coupling Hamiltonian is anisotropic, where now, from (A3) and (A4) of of [115], we find

$$
\frac{{}_{SF}\langle\Psi|\sum_j \vec{S}_j\cdot\vec{S}_{j+1}|\Psi\rangle_{SF}}{L}=\left(\frac{1}{4}-\ln 2\right)\left[n^2-\frac{\sin^2(\pi n)}{\pi^2}\right].
$$

Collecting all the pieces it is easy to see that

$$
\begin{aligned}
\mathcal{E}_{SF}=\frac{{}_{SF}\langle\Psi|H_{s-c}|\Psi\rangle_{SF}}{L}=-\frac{2t}{\pi}\sin(\pi n)+ \\
+\frac{4t^2(1-z^2)}{U}\left[n^2-\frac{\sin^2(\pi n)}{\pi^2}\right]\left[\frac{2+\Delta}{3}\left(-\ln 2+\frac{1}{4}\right)-\frac{1}{4}\right]
\end{aligned}
$$

As an example, in Fig. 3.8 we plot the local densities of fermions obtained numerically on a chain with $L = 60$ and open boundary conditions (OBC), $z = 0.1$, $n = 0.2$ and $u = 100$. The two species tend to occupy alternate regions but the fraction of double occupation is still significant. The comparison with the total density profile for spinless fermions at the same equivalent filling shows that the SF state is a good description of the ground state in this case. We have verified that the same happens if the filling is increased up to $n = 0.9$, the other parameters being unchanged. On the contrary, if we still fix $u = 100$, $n = 0.2$ but increase the anisotropy to $z = 0.3$, appreciable differences in the density profiles start to appear.

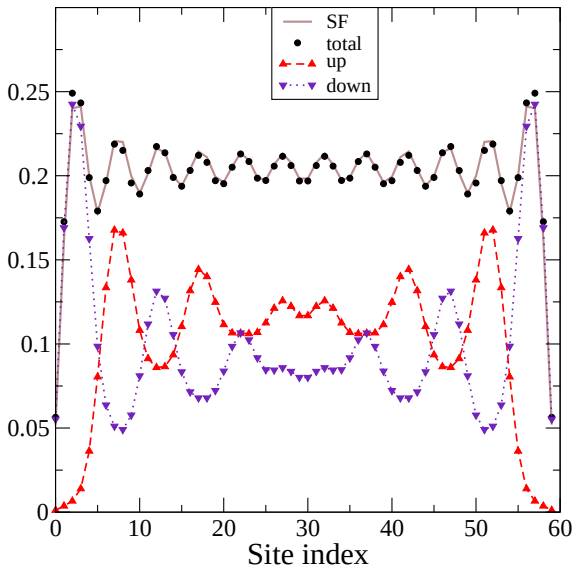

Figure 3.8: Spatial density profiles for an open chain with $z = 0.1$, filling $n = 0.2$ and $u = 100$. The continuous curve labelled SF is the local density for an equivalent chain of spinless fermions (i.e. Eq. (3.17) with $\ell = L$ and $p = nL$), showing a very good agreement with the spinful numerical data.

3.4.2 Spatially separated states

In the strong-coupling approach we can actually formulate a slightly more general form of the PS state with respect to that of Sec. 3.3.1 which, however, leads formally to the same analytical expressions. Let us consider a sequence of M contiguous intervals $I_{j\uparrow}$, $I_{j\downarrow}$ ($j = 1, \ldots, M$) and a state $|\Psi\rangle_{PS}$ in which the up and down spins are separated in the sense that there are no doubly occupied sites, $I_{1\uparrow}$ contains only up spins, $I_{1\downarrow}$ contains only down spins, then again $I_{2\uparrow}$ with up spins and so on. Let $L_{j\sigma}$ and $N_{j\sigma}$, respectively, the number of sites and the number of electrons in the interval $I_{j\sigma}$. We then make the further strong assumption that each up or down interval, irrespective of its length, is equally filled meaning that $\bar{n}_\uparrow = N_{j\uparrow}/L_{j\uparrow}$ and $\bar{n}_\downarrow = N_{j\downarrow}/L_{j\downarrow}$ do not depend on j. Now, if

$$\nu L = \sum_{j=1}^{M} L_{j\downarrow} \ , \quad (1-\nu)L = \sum_{j=1}^{M} L_{j\uparrow}$$

are the total lengths associated with the motion of down and up spins we have $N_\uparrow = \sum_{j=}^{M} N_{j\uparrow} = \sum_{j=1}^{M} \bar{n}_\uparrow L_{j\uparrow} = \bar{n}_\uparrow L(1-\nu)$ and similarly $N_\downarrow = \bar{n}_\downarrow L\nu$ and so, for equally populated species $\bar{n}_\uparrow = n/[2(1-\nu)]$ and $\bar{n}_\downarrow = n/(2\nu)$.

We first consider the thermodynamic limit in the case in which the interface points (which are $2M$ in number) do not contribute to the bulk energy density ($\lim_{L\to\infty} 2M/L = 0$) and, at the same time, each interval is extensively large ($\lim_{L\to\infty} L_{j\sigma}/L > 0$), so that for every interval we can use the formula for the kinetic energy density of free fermions without

worrying about finite-size and/or boundary effects:

$$\frac{{}_{PS}\langle\Psi|T_{s-c}|\Psi\rangle_{PS}}{L} = \frac{\sum_{j=1}^{M} L_{j\uparrow}}{L}\left[-\frac{2t_\uparrow}{\pi}\sin\left(\pi\frac{n}{2(1-\nu)}\right)\right]$$
$$+\frac{\sum_{j=1}^{M} L_{j\downarrow}}{L}\left[-\frac{2t_\downarrow}{\pi}\sin\left(\pi\frac{n}{2\nu}\right)\right]$$
$$= -\frac{2t_\uparrow}{\pi}(1-\nu)\sin\left(\pi\frac{n}{2(1-\nu)}\right) - \frac{2t_\downarrow}{\pi}\nu\sin\left(\pi\frac{n}{2\nu}\right).$$

Note that we do not necessarily require that the heavy (down) species is fully compressed, meaning $\nu = n/2$. The value for ν will be determined variationally in order to give the smallest possible energy at a fixed z, exactly as done in Sec. 3.3.2. Let us now calculate the energy of such a state.

As far as the J-term is concerned we first note that the transverse part is vanishing. In fact both S_j^x and S_j^y are composed by spin-flip terms like $c_{j\sigma}^\dagger c_{j\bar{\sigma}}$ but each interval contains spins of only one specie. Next, all the Δ-term can be rewritten as

$$\Delta\left(S_j^z S_{j+1}^z - \frac{n_j n_{j+1}}{4}\right) = \frac{\Delta}{4}[(n_{j\uparrow} - n_{j\downarrow})(n_{j+1\uparrow} - n_{j+1\downarrow})$$
$$-(n_{j\uparrow} + n_{j\downarrow})((n_{j+1\uparrow} + n_{j+1\downarrow})] = -\frac{\Delta}{2}(n_{j\uparrow}n_{j+1\downarrow} + n_{j\downarrow}n_{j+1\uparrow}). \qquad (3.15)$$

When the expectation value on $|\Psi\rangle_{PS}$ is taken, the up and down parts factorize and there can be non-vanishing contributions only when j and $j+1$ are at an interface between two intervals carrying opposite spins. If, as assumed above, the number of interface points does not grow as L we can neglect these contributions in the limit $L \to \infty$. Therefore the energy density of the PS state reads

$$\mathcal{E}_{PS}(\nu) = \frac{{}_{PS}\langle\Psi|H_{s-c}|\Psi\rangle_{PS}}{L}$$
$$= -\frac{2t_\uparrow}{\pi}(1-\nu)\sin\left(\pi\frac{n}{2(1-\nu)}\right) - \frac{2t_\downarrow}{\pi}\nu\sin\left(\pi\frac{n}{2\nu}\right).$$

As anticipated, this expression coincides with Eq. (3.3) in the balanced case $n_\uparrow = n_\downarrow = n/2$. In Fig. 3.9 we present two examples of the spatial density profile for large u and intermediate/large z, from which the spatial separation of the two species can be clearly inferred. Note also that the light species occupies regions with a non-vanishing fraction of empty sites and an oscillating density profile $\langle n_{j\uparrow}\rangle$ is seen. Nonetheless the local

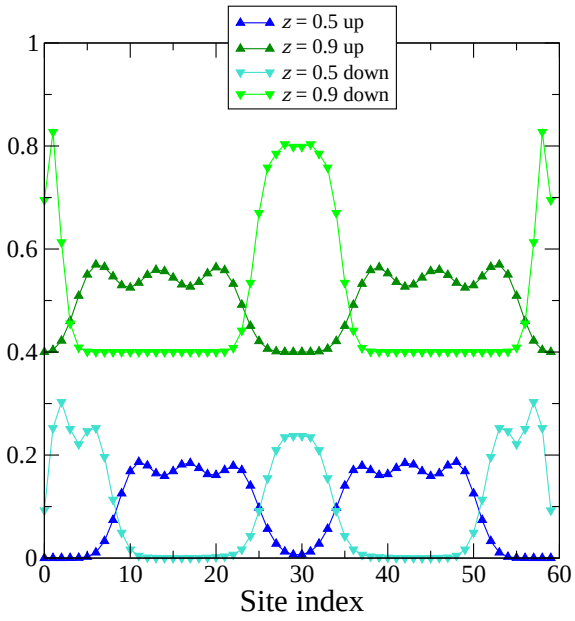

Figure 3.9: Spatial density profiles for open chains with $z = 0.5$ and $z = 0.9$ (offset by $+0.4$ for clarity), filling $n = 0.2$ and $u = 100$.

density in the intervals occupied by the heavy fermions does not reach 1, so in these case we do not have a TSS as instead, for example, in Fig. 3 of ref. [116] valid for $u = 20$, $z = 2/3$, filling $n = 0.8$ on 40 sites (reproduced in our calculations but not shown here).

3.4.3 PS′: Extensive number of intervals $M = \alpha L$

In order to treat also the case in which the number of interfaces scales as a finite fraction α of the total number of sites, we will assume that all the intervals hosting up spins are equally long and equally filled: $L_{j\uparrow} = \ell_\uparrow$, $N_{j\uparrow} = p_\uparrow \; \forall j = 1, \ldots, M$ so that $\ell_\uparrow = (1-\nu)/\alpha$ and $p_\uparrow = n/(2\alpha)$; similarly for the intervals with down spins $\ell_\downarrow = \nu/\alpha$ and $p_\downarrow = n/(2\alpha) = p_\uparrow$. Note that, for equally populated species, necessarily the finite number of electrons in each interval is the same for up or down spins, while the finite lengths are in general different. The energy density of this type of phase separated state will therefore have the form

$$\mathcal{E}_{PS'} = \frac{M}{L}(\kappa_\uparrow + \kappa_\downarrow) - \frac{J\Delta}{L}\sum_{j=1}^{L}(\langle n_{j\uparrow}\rangle\langle n_{j+1\downarrow}\rangle + \langle n_{j\downarrow}\rangle\langle n_{j+1\uparrow}\rangle)$$

where $\kappa_{\uparrow,\downarrow}$ are the kinetic energies of $p = p_\uparrow = p_\downarrow$ up or down fermions on intervals of length $\ell_{\uparrow,\downarrow}$ with OBC, while the Δ-term comes from Eq. (3.15) and now cannot be neglected. The on-site terms $\langle n_{j\sigma}\rangle$ also have to be evaluated in the same fashion and will be localized at the left or right

end of the intervals (with equal values). Let us denote them by η_σ; we have a contribution $\langle n_{\mathrm{right}\uparrow}\rangle\langle n_{\mathrm{left}\downarrow}\rangle + \langle n_{\mathrm{right}\downarrow}\rangle\langle n_{\mathrm{left}\uparrow}\rangle = 2\eta_\uparrow\eta_\downarrow$ for each of the M pairs of up+down intervals so that

$$\mathcal{E}_{PS'} = \alpha(\kappa_\uparrow + \kappa_\downarrow - 2J\Delta\eta_\uparrow\eta_\downarrow).$$

The calculation of the kinetic energy and of the surface density for an effective open chain of ℓ sites with p free fermions is given in the addendum 3.5, leading to:

$$\mathcal{E}_{PS'} = \alpha t\{(1+z)\left\{1 - \frac{\sin\left[\frac{\pi(2p+1)}{2(\ell_\uparrow+1)}\right]}{\sin\left[\frac{\pi}{2(\ell_\uparrow+1)}\right]}\right\}$$

$$+(1-z)\left\{1 - \frac{\sin\left[\frac{\pi(2p+1)}{2(\ell_\downarrow+1)}\right]}{\sin\left[\frac{\pi}{2(\ell_\downarrow+1)}\right]}\right\}$$

$$-\frac{1+z^2}{u}\frac{\left\{2p+1-\frac{\sin\left[\frac{\pi(2p+1)}{\ell_\uparrow+1}\right]}{\sin\left(\frac{\pi}{\ell_\uparrow+1}\right)}\right\}\left\{2p+1-\frac{\sin\left[\frac{\pi(2p+1)}{\ell_\downarrow+1}\right]}{\sin\left(\frac{\pi}{\ell_\downarrow+1}\right)}\right\}}{(\ell_\uparrow+1)(\ell_\downarrow+1)}\}.$$

The conditions $p \le \ell_\uparrow$ and $p \le \ell_\downarrow$ define the range of $\nu \in [n/2, 1-n/2]$, while the conditions $p \ge 1$, $\ell_\uparrow \ge 1$ and $\ell_\downarrow \ge 1$ imply $\alpha \le \min(n/2, \nu, 1-\nu) = n/2$. Once this expression is minimized by suitable values of α and ν in this range we should, at least, check if the resulting energy density is smaller than the optimal energy density $\mathcal{E}_{PS}$ determined above for the same values of z, n and, now, also u.

Finally, we mention that we have also tried to enlarge the set of trial/variational states by including the homogeneous one (defined in Sec. 3.3), which is the correct ground state in the limit $U = 0$ for all z. However we have verified that this additional state, for the fillings we have considered, could become relevant only when $u \lesssim 1$, outside the domain of validity of the strong-coupling approach. Therefore, for the sake of compactness, we do not report these results here.

3.4.4 Phase boundaries

From the condition $\mathcal{E}_{PS} < \mathcal{E}_{SF}$ we get

$$-\frac{2(1+z)}{\pi}(1-\nu^*)\sin\left(\pi\frac{n}{2(1-\nu^*)}\right)$$

$$-\frac{2(1-z)}{\pi}\nu^* \sin\left(\pi\frac{n}{2\nu^*}\right) < -\frac{2}{\pi}\sin(\pi n)$$
$$+\frac{4(1-z^2)}{u}\left[n^2-\frac{\sin^2(\pi n)}{\pi^2}\right]\left[\frac{2+\Delta}{3}\left(-\ln 2+\frac{1}{4}\right)-\frac{1}{4}\right]$$

that is $u < u_{PS}(z)$ for $d(n,z) > 0$ or $u > u_{PS}(z)$ otherwise, having defined

$$d(n,z) = \sin(\pi n) - (1+z)(1-\nu^*)\sin\left[\pi\frac{n}{2(1-\nu^*)}\right]$$
$$-(1-z)\nu^*\sin\left(\pi\frac{n}{2\nu^*}\right)$$

and

$$u_{PS}(n,z) = 2\pi(1-z^2)\frac{\left[n^2-\frac{\sin^2(\pi n)}{\pi^2}\right]\left[\frac{2+\Delta}{3}\left(-\ln 2+\frac{1}{4}\right)-\frac{1}{4}\right]}{d(n,z)}$$

Now we can draw a phase diagram in the (z,u)-plane for a fixed value of the total filling n by indicating the regions where the PS or the SF state has the lower energy. We show two examples (for $n = 0.4$ and 0.9) in Figs. 3.10 and 3.11, respectively. We have analyzed in detail also the phase diagram for $n = 0.6$ (not shown), that turns out be qualitatively similar to the one for $n = 0.4$. Having in mind that bosonization could be considered quantitatively reliable only for small values of the interaction, we have reported in the figures (dashed lines) the curves of Wentzel-Bardeen instability [107] where the velocity of one of the bosonization modes vanishes thereby indicating phase separation. In addition, we have considered two typical cases of PS at $n = 0.9$ ($L = 20, 40, 60$), namely those at $u = 100$ for $z = 0.1$ and at $u = 5$ for $z = 0.9$. In both cases, the charge structure factor $S(q)$ (as defined in Sec. 3.2) displays a divergence for $q \to 0$ typical of PS states [105] and a peak at $q = 4k_F(\mathrm{mod}2\pi) = 2\pi n(\mathrm{mod}2\pi) = 2\pi(1-n)$.

In the strong-coupling approach the most interesting thing to understand seems to be the divergence of the transition line separating PS from SF behavior at small z and large u. We have verified that when $\nu = \nu^*(z)$ is inserted into $d(n,z)$ the denominator appearing in $u_{PS}(n,z)$ is always negative. In order to estimate $u_{PS}(n,z)$ analytically we set $\nu^*(z) = 1/2 - z\nu_1 - z^2\nu_2 + O(z^3)$ with $\nu_{1,2} > 0$ (see Fig. 3.4) and expand $d(n,z)$ for $z \to 0$

$$d(n,z) = -2\nu_1[f(\pi n) - \pi^2 n^2 \nu_1 \sin(\pi n)]z^2 + O(z^3)$$

so that at leading order

$$u_{PS}(n,z) = \frac{1}{z^2}\frac{\pi\ln 2\left[n^2-\frac{\sin^2(\pi n)}{\pi^2}\right][1+O(z)]}{\nu_1(n)[f(\pi n)-\pi^2 n^2\nu_1(n)\sin(\pi n)]} \tag{3.16}$$

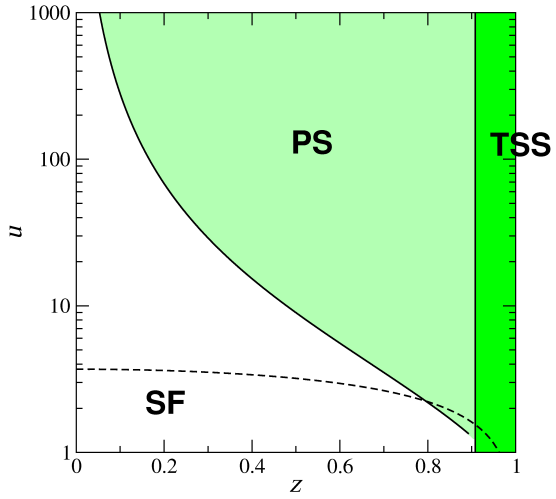

Figure 3.10: Transition lines in the (z, u)-plane at filling $n = 0.4$ indicating how the ground state changes from SF to PS. In the separated regime above the transition lines, the state can be either PS (left) or TSS (right) (see Sec. 3.3.2) and the separation between the two is marked by the vertical lines (analogously to Fig. 3 of ref. [108]). The dashed line corresponds to the bosonization prediction.

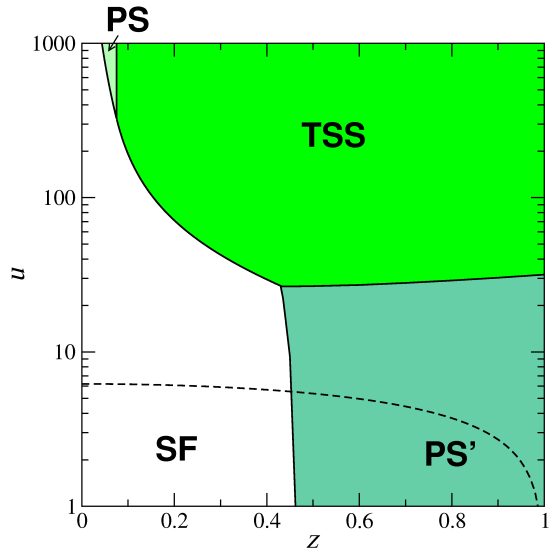

Figure 3.11: Same as Fig. 3.10 but with filling $n = 0.9$. Now also the PS' (see text) state is relevant for moderate values of u and the corresponding transition lines with SF and PS are marked.

with $f(x) = \sin x - x\cos x$ as before. As far $\nu_1(n)$ as is concerned, by inserting $\nu = 1/2 - z\nu_1 + O(z^2)$ in Eq. (3.5) and solving at first order in z we get $\nu_1(n) = f(\pi n)/[f'(\pi n)2\pi n]$. In summary, our analytical approach predicts that there is no finite value of z below which PS disappears; by moving to a sufficiently large repulsive coupling it is always possible to induce a PS at arbitrarily small anisotropy.

3.4.5 Inclusion of phase separated states with an infinite number of interfaces

We have compared the energy density of the PS state at given values of n and z with the corresponding value for the PS' state discussed in Sec. 3.4.3. At small filling, say $n = 0.1$, the two variational solutions (with respect to ν or ν and α, respectively) coincide in the sense that the optimal value $\alpha^* \to 0$ and the optimal value of ν is the same. Moreover $\mathcal{E}_{PS'} \geq \mathcal{E}_{PS}$. When the filling is increased to, say, $n = 0.4$ the situation is similar with the exception of a small region ($u \lesssim 0.8$ for $z = 0$ or $u \lesssim 2.8$ for $z = 0.9$) that can be considered to be outside the scope of the strong-coupling approach. At $n = 0.6$, the PS' solution can be ignored for $u \gtrsim 3.2$ (a result checked at $z = 0$ and $z = 0.1$) or $u \gtrsim 5.2$ (as checked at $z = 0.5$ and $z = 0.9$). Thus, close to half-filling the PS' becomes relevant also at intermediate values of u and we have examined it in more detail.

Let us fix $n = 0.9$; in the symmetric case $z = 0$ the optimal value of α remains at its maximum $\alpha^* = n/2$ for $u < 32$ where it starts to decrease to reach $\alpha^* = 0$ at $u \cong 44.3$; the PS' state has a lower energy density with respect to the PS one for $u \lesssim 45.8$. For positive z as long as $z \leq 0.43$ the PS' solution is never better than the ones considered before. When z increases further the PS' state is favored over the PS or even the SF one; the region at large z and moderate u where $|\Psi\rangle_{PS'}$ has a lower energy is characterised by the fact that $\alpha^* = n/2$ and $\nu^* = n/2$ so that $p = \ell_\downarrow = 1$ meaning that all the down spins are isolated from each other. This configuration resembles the trimer crystal phase found in ref. [117], with a mixture of hardcore bosons with attractive interaction and fillings 1/3 and 2/3, which is equivalent to a repulsive case with balanced species and total filling 2/3 when a particle-hole transformation is performed.

3.5 Conclusions

Our study, which combines analytical calculations in the strong- and weak-coupling regimes and DMRG simulations both for attractive and repulsive

interaction, sheds some light on three qualitative and quantitative questions that are still open in the literature of the 1D AHM:

1. The shape of the transition line from SS to CDW dominant correlations for $U < 0$ is filling-dependent and re-entrant in some cases (see Fig. 3.3);
2. Phase separation and phase segregation take place close to the Falicov-Kimball limit above an interaction value U_c which depends on the population in such a way that it approaches zero in the small density regime. Furthermore, transitions between phase separation and phase segregation at varying interaction take place at a nearly constant asymmetry;
3. For small asymmetry, close to the Hubbard limit $t_\downarrow \lesssim t_\uparrow$, the SF-PS transition takes place at larger and larger values of U; Eq. (3.16), obtained in the framework of a variational strong-coupling argument, indicates that an arbitrarily small asymmetry is sufficient, at very large repulsions, to create a phase separated state which destroys the spinless fermion-like ground state of the Hubbard model.

Addendum: Free spinless fermions with open boundary conditions

The eigenfunctions of the hopping operator $-t\sum_{j=1}^{L-2}(c_j^\dagger c_{j+1} + \text{h.c.})$ have the form

$$\varphi_m(j) = \sqrt{\frac{2}{\ell+1}}\sin(k_m j)\ , \quad k_m = \frac{\pi m}{\ell+1}\ , \quad m = 1, \ldots, \ell$$

and the dispersion relation is formally the same as in the case of PBC $\epsilon(k_m) = -2t\cos(k_m)$ so

$$\kappa = -2t\sum_{m=1}^{p}\cos\left(\frac{\pi m}{\ell+1}\right) = t\left\{1 - \frac{\sin\left[\frac{\pi(2p+1)}{2(\ell+1)}\right]}{\sin\left[\frac{\pi}{2(\ell+1)}\right]}\right\}$$

where $p \leq \ell$ is the number of particles.

To compute the average density on the j-th site $\langle n_j\rangle$ we pass to the creation/annihilation operators in k-space

$$c_j = \sqrt{\frac{2}{L+1}}\sum_{m=1}^{\ell}\sin\left(\frac{\pi m}{\ell+1}j\right)\tilde{c}_{k_m}$$

$$\langle n_j \rangle = \frac{2}{L+1} \sum_{m,m'} \sin\left(\frac{\pi m}{\ell+1} j\right) \sin\left(\frac{\pi m'}{\ell+1} j\right) \times$$
$$\times \langle 0 | \tilde{c}_{k_1} \dots \tilde{c}_{k_p} (\tilde{c}^\dagger_{k_m} \tilde{c}_{k_{m'}}) \tilde{c}^\dagger_{k_p} \dots \tilde{c}^\dagger_{k_1} | 0 \rangle$$

The only non-vanishing possibility within the matrix element for the vacuum $|0\rangle$ filled up to the momentum $k_p = \pi p/(\ell+1)$ is $m' = m$, so we have the characteristic function of the Fermi sea n_{k_m}

$$\langle n_j \rangle = \frac{2}{\ell+1} \sum_{m=1}^{p} \sin^2\left(\frac{\pi m}{\ell+1} j\right)$$
$$= \frac{p}{\ell+1} - \frac{1}{\ell+1} \sum_{m=1}^{p} \cos\left(\frac{2\pi m}{\ell+1} j\right)$$
$$= \frac{2p+1}{2(\ell+1)} - \frac{\sin\left[\frac{\pi(2p+1)}{\ell+1} j\right]}{2(\ell+1)\sin\left(\frac{\pi}{\ell+1} j\right)} \tag{3.17}$$

The density at the edge is obtained by setting $j = 1$.

Chapter 3. Fermi-Fermi mixtures: pairing regimes and phase separation in the asymmetric Hubbard model.

Chapter 4

Pairing, crystallization and Haldane liquid of mass unbalanced atomic mixtures in one-dimensional optical lattices

We numerically determine the very rich phase diagram of mass-imbalanced binary mixtures of hardcore bosons (or equivalently of fermions, or hardcore-Bose/Fermi mixtures) loaded in one-dimensional optical lattices. Focusing on commensurate fillings away from half filling, we find a fundamental asymmetry between attractive and repulsive interactions. Attraction is found to always lead to pairing, associated with a spin gap, and to pair crystallization for very strong mass imbalance. In the repulsive case the two atomic components remain instead fully gapless over a large parameter range. Only a very strong mass imbalance leads to the opening of a spin gap, associated with a novel Haldane liquid phase exhibiting topological string order. This phase is the precursor of a crystalline phase occurring for an even stronger mass imbalance. This fundamental asymmetry is at odds with recent theoretical predictions, and can be tested directly via time-of-flight experiments on trapped cold atoms.

One-dimensional quantum liquids occupy a special place in the context of quantum many-body systems: indeed interactions of any strength lead to quantum fluctuations as strong as to discard Bose condensation for bosons and the Fermi liquid picture for fermions down to zero temperature. For sufficiently weak interactions a new unifying paradigm of the so-called Tomonaga-Luttinger liquids (TLL) emerges [11], characterized by the fact that all elementary excitations are gapless, and both diag-

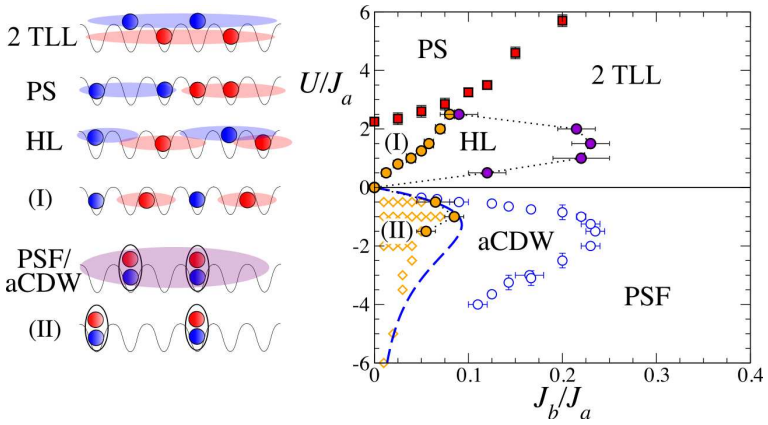

Figure 4.1: Phase diagram of a mass-imbalanced atomic mixture with filling $n_a = n_b = 1/3$. The phase boundaries are determined via QMC; the open diamonds indicate points in parameter space for which DMRG finds a fully gapped Wigner crystal phase of type (II). The dashed line indicate the FK gap Δ_k/J_a for kink-antikink pairs. The left panel presents a sketch of the phases: 2 TLL = 2 Tomonaga-Luttinger liquids; PS = phase separated; HL = Haldane liquid; PSF = pair superfluid; aCDW = algebraic charge density wave; (I) and (II): Wigner crystals.

onal and off-diagonal correlations decay algebraically with the distance. Recent advances in the trapping of ultracold atoms in optical lattices allow to realize one-dimensional quantum liquids in a highly flexible way, with the possibility of fully controlling the statistics and the interaction strength [44]. Recent experiments have demonstrated the physics of one-dimensional Bose gases with strong interactions up to the hardcore (or Tonks-Girardeau) limit [9, 8] (see also Chapter 2). A special role in the context of one-dimensional systems is played by binary mixtures, either bosonic, fermionic, or Bose-Fermi ones, for which TLL theory predicts the separation of spin and charge modes [11]. In the case of particles with equal masses and repulsive short-range interactions, both charge and spin sectors can be gapless, and one recovers an effective picture of two decoupled TLLs. Such a picture can be made unstable via several mechanisms: via Mott localization in presence of an underlying lattice and for integer total filling; via localization into a Wigner crystal in presence of a strong off-site repulsion; via phase separation; or via the formation of bound states (*e.g.* Cooper pairs for attractive interactions) leading to the appearance of a spin gap.

Here we show that the TLL picture undergoes a complex series of in-

stabilities in binary mixtures with *mass imbalance* between the two species. We focus here on quantum particles on a lattice with intraspecies hard-core repulsion and on-site interspecies interactions, describing at the same time spin-1/2 fermions, spin-1/2 hardcore bosons, and mixtures of hard-core bosons and spinless fermions. The system Hamiltonian reads

$$\mathcal{H} = \sum_i \left[-(J_a a_i^\dagger a_{i+1} + J_b b_i^\dagger b_{i+1} + \text{h.c.}) + U n_{i,a} n_{i,b} \right] \tag{4.1}$$

in which a and b correspond to the two atomic species. Mass imbalance is controlled by the ratio $j = J_b/J_a$. As far as the spectrum and the diagonal observables are concerned, we do not need to specify the statistics of the a and b operators; for what concerns off-diagonal observables, on the other hand, in the following we will refer explicitly to hardcore bosons, satisfying bosonic commutation relations off-site and fermionic anticommutation relations on-site. The denomination of the many-body phases will also be mostly inspired by the case of hardcore-boson mixtures.

We will consider both repulsive ($U > 0$) and attractive ($U < 0$) interactions, and we will here focus on the case of equal densities away from half filling, $n_a = n_b = n \neq 1/2$. Our results refer to a commensurate filling $n = 1/p$ with integer p (or equivalently $n = 1 - 1/p$). The system with equal masses, $J_a = J_b$, is integrable [52]: it features spin-charge separation into two TLL in the repulsive case; in the attractive case an a-b bound state appears, associated with the opening of a spin gap, and only the charge sector remains gapless, giving rise to a paired superfluid (PSF) phase. The case of mass imbalance has been studied recently by bosonization [88, 107, 104], and numerically via the density-matrix renormalization group (DMRG) and related approaches [118, 97] (see also the previous Chapter).

Making use of numerically exact methods, here we determine comprehensively the rich phase diagram of the system with mass imbalance, $J_b < J_a$, as shown in Fig. 4.1. The latter figure refers to the case $n = 1/3$, but the qualitative features are generic for commensurate fillings. Our main findings are the following: 1) In the attractive case, the PSF phase is found to persist up to strong imbalance, at which the system becomes unstable to the formation of a Wigner crystal of pairs. 2) In the repulsive case, on the other hand, the double TLL of the mass-balanced case survives up to a large imbalance, at which two different instabilities appear. For sufficiently large repulsion, the two species phase-separate. For weaker repulsion, first a spin-gap opens, associated with the appearance of an exotic Haldane liquid (HL) phase with fluctuating magnetic order captured by a string order parameter; this phase is the precursor of a Wigner-crystal

phase with pinned b particles, and a particles localized in the interstitial regions.

Before discussing the detailed derivation of the phase diagram, we point out that the physics described in this paper is largely accessible to current experimental setups on stable ultracold mixtures in one-dimensional optical lattices. The mass imbalance can be realized with heteronuclear mixtures (*e.g.* ^{40}K-^{6}Li, for the fermionic case, ^{41}K-^{87}Rb for the bosonic case, and ^{40}K-^{87}Rb for the Bose-Fermi case [43]), and with homonuclear mixtures in different hyperfine states, and it can be continuously tuned by using lasers with a wavelength close to the magic value or to an atomic resonance for one of the two species. The interspecies interaction can be tuned by Feshbach resonances, as widely demonstrated in the recent literature [43]. Given the unique opportunity offered by cold atoms to realize the asymmetric mixtures treated in this paper, in the following we will repeatedly refer to the experimental implications of our results.

The phase diagram of Fig. 4.1 is the result of a joint numerical study based on quantum Monte Carlo (QMC) and DMRG. Our QMC calculations are based on a canonical formulation [119] of the Stochastic Series Expansion approach with directed loops [120], applied to chains with up to $L = 150$ sites with periodic boundary conditions, and at temperatures $\beta J_b = L$ capturing the $T = 0$ physics for both species. Our DMRG calculations apply to chains with up to $L = 144$ with open boundary conditions and retaining up to $M = 1156$ states, and with periodic boundary conditions up to $L = 48$ keeping up to $M = 1800$ states and 7 finite-size sweeps.

We start our discussion by the attractive case. For a very broad range of mass imbalance, the system displays a PSF phase, characterized by quasi-condensation of bound a-b pairs, giving rise to an algebraic decay of the pairing correlation function [11]:

$$G_{ab}(r) = \langle a_i^\dagger b_i^\dagger b_{i+r} a_{i+r} \rangle \sim r^{-1/K_\rho}; \tag{4.2}$$

density-density correlations are also decaying algebraically as

$$C_\rho(r) = \langle n_i n_{i+r} \rangle - n^2 \approx -\frac{K_\rho}{\pi^2 r^2} + A \frac{\cos(2\pi n r)}{r^{K_\rho}}; \tag{4.3}$$

here $n_i = n_{i,a} + n_{i,b}$, and K_ρ is the charge Luttinger exponent. For equal masses $K_\rho > 1$ [11] for all $|U| > 0$, so that the dominant correlations are the pairing ones. We extract the Luttinger exponent from the slope of the density structure factor at $q \to 0$, $S_\rho(q) = \sum_r \exp(iqr) C_{ab}(r) \approx K_\rho \, q/\pi$, and we find that mass imbalance leads to a reduction of K_ρ, consistently with what observed for other fillings in the previous Chapter by using DMRG

techniques. For large mass imbalance the Luttinger exponent K_ρ becomes smaller than one: this corresponds to the loss of quasi-condensation, in favor a quasi-solid phase (or algebraic charge density wave, aCDW), with dominant density correlations. This phase is the precursor of a quantum phase transition to a Wigner crystal of pairs – phase (II) of Fig. 4.1 – with the onset of long-range density order at wavevector $Q = 2\pi n$. We determine the extent of the crystalline phase via QMC by determining the mass imbalance at which $S_\rho(Q)$ starts diverging linearly with system size; and by DMRG detecting the onset of the exponential decrease of G_{ab} and C_{ab}, marking the opening of a charge gap [121]. The crystalline phase is well understood coming from the Falicov-Kimball (FK) limit, $J_b = 0$. In this limit, which is easily treated with exact diagonalization, we find that the ground state corresponds to the Wigner crystal of pairs for all values $U < 0$. The gap $\Delta_{\rm k}$ to the formation of kink-antikink pairs in the crystal is found to be a non-monotic function of $|U|$, displaying an intermediate maximum. We observe that, for small $|U|$, the boundary of the crystalline region follows closely the locus at which the gap $\Delta_{\rm k}$ equals J_b, and it has a re-entrant shape mimicking the non-monotonic behavior of the gap as a function of U. This shows that the quantum melting transition corresponds to a condensation of kink-antikink pairs in the ground state.

The repulsive side of the phase diagram is more complex. Based on a bosonization and renormalization group approach, Refs. [88, 107] conclude that a spin gap should open for any infinitesimal mass imbalance as $\Delta_s \approx \Lambda \exp(-A'/|J_a - J_b|)$ for $J_b \lesssim J_a$, where $\Lambda \sim J_a, J_b$. On the contrary, Ref.[104], also based upon bosonization, concludes that the spin gap is absent in the repulsive case. In contrast to Refs.[88] and [107], all our numerical findings point toward the persistence of a fully gapless TLL behavior for both the charge *and* spin sector over a dominant portion of the phase diagram. Our conclusion is based on a number of crossed evidences. First of all, we observe that the one body correlation functions $G_a(r) = \langle a_i^\dagger a_{i+r} \rangle$ and $G_b(r) = \langle b_i^\dagger b_{i+r} \rangle$ can be very well fitted with the simple power-law form $G_{a(b)}(r) = A_{a(b)} d(r|L)^{-1/(2K_{a(b)})}$, where $d(r|L) = L|\sin(\pi r/L)|/\pi$ is the conformal distance (see Fig. 4.2). In particular we find that, for weak and moderate repulsions, $K_{a(b)} > 0.5$, which implies that the momentum distribution $n_{a(b)}(q) = \sum_r \exp(iqr) G_{a(b)}(r)$ displays a quasi-condensation divergent peak at $q = 0$, to be detected in time-of-flight experiments.

Moreover we investigate the spin-spin correlation function

$$C_\sigma(r) = \langle S_i^z S_{i+r}^z \rangle \approx -\frac{K_\sigma^*}{\pi^2 r^2} + A \frac{\cos(2\pi n r)}{r^{K_\rho + K_\sigma^*}}; \tag{4.4}$$

where $S_i = (n_{i,a} - n_{i,b})/2$, and K_σ^* is the spin Luttinger exponent; in absence

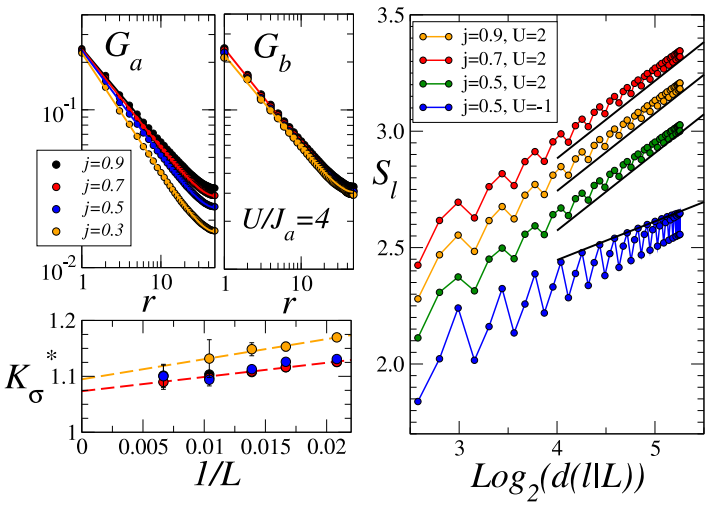

Figure 4.2: Evidences for the absence of spin gap for moderate mass imbalance. The left panels show the Green's function for both species (solid lines are fits to $A_{a(b)}d(r|L)^{-1/(2K_{a(b)})}$, $L = 96$) and the extrapolated K_σ^* exponent for $U/J_a = 4$ and various j values. In the right panel, we plot the block entropy S_l as a function of the conformal length in logarithmic scale (up to a constant contribution) for chains with $L = 120$ sites and different values of U, j; black thick line are reference line for $c = 2$ (upper 3) and $c = 1$ conformal field theories.

of a spin gap $K_\sigma^* \geq 1$. We extract the Luttinger exponent from the low-q behavior of the spin structure factor, $S_\sigma(q) \approx K_\sigma^* \, q/\pi$, extrapolating the finite-size estimate $K_\sigma^*(L) = [(L/2)S_\sigma(2\pi/L; L) + (L/4)S_\sigma(4\pi/L; L)]/2$ to the thermodynamic limit $L \to \infty$. We find that mass imbalance leads initially to a growth of K_σ^* above the exact value $K_\sigma^* = 1$ for the balanced case; K_σ^* is found to decrease again towards 1 and further drop to zero only for strong mass imbalance (see Fig. 4.2).

Finally we exploit the fact that an explicit counting of the number of gapless degrees of freedom in the system comes from the central charge c of the conformal field theory corresponding to our model of interest. This quantity can be directly extracted via DMRG, using the fundamental result that the entanglement entropy (EE) of a boundary block of the system

grows with the size l of the block [122] as

$$S_l = -\mathrm{Tr}(\rho_l \log_2 \rho_l) \approx \frac{c}{6} \log_2[d(l|L)] + \mathrm{const.} \tag{4.5}$$

where ρ_l is the reduced density matrix of the boundary block. Fig. 4.2 shows that the scaling of the EE is fully consistent with $c = 2$ providing further evidence for the fact that the TLL has two gapless components even for a significant mass imbalance.

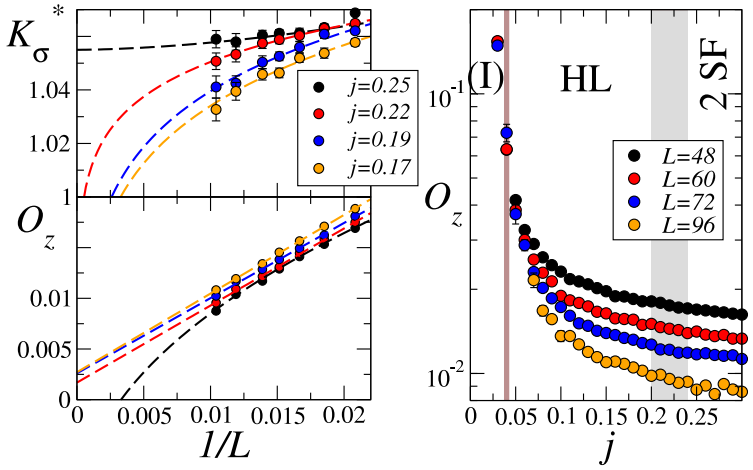

Figure 4.3: Left panels: appearance of a spin gap for $U/J_a = 1$ and increasing mass imbalance, and concomitant appearance of string order. Right panel: evolution of the string-order parameter with mass imbalance.

On the other hand, a careful study of the behavior of the system shows that the two-component TLL becomes indeed unstable to the formation of a spin gap for *strong* mass imbalance ($j \lesssim 1/4$ for $n = 1/3$). The spin gap, albeit rather small, leaves a clear signature in the Luttinger exponent K_σ^*, which is found to extrapolate to a value smaller than 1, as shown in Fig. 4.3. The opening of a spin gap signals the formation of a bound state of some sort: but what could this bound state be in a purely repulsive system? We argue that a bound state can appear between the light a particles and the *holes* of the b species, which are in a commensurate proportion

$m = (1-n)/n$ to the a particles. As shown in Ref. [123], a sufficiently strong mass imbalance can indeed bind together particle composites in 1D quantum fluids - in the specific case of $n = 1/3$ we have trimers formed by one a particle and two b holes ($\bar{b}$). If the a-$m\bar{b}$ composites have mutual repulsive interactions, as observed in the case of trimers [117], their binding favors configurations of the type $..a0ba0b0a0b0ab...$ in which the a and b particles alternate spatially. Such configurations, albeit lacking long-range density order, contain strong non-local correlations that can be captured using a *string order parameter*

$$O_z(L) = -\left\langle \sigma_0^z \, e^{i\pi \sum_{j=1}^{L/2-1} \sigma_j^z} \, \sigma_{L/2}^z \right\rangle \tag{4.6}$$

where $\sigma_i^z = 2S_i^z = n_{i,a} - n_{i,b}$. This is the analog of the string order parameter introduced in Ref. [124] to capture the hidden order of Haldane chains. As shown in Fig. 4.3, we observe indeed that $O_z(L \to \infty)$ becomes finite at the onset of the spin gap. A fundamental difference with the case of Haldane chains is that here string order appears in a globally *gapless* system, which can be termed a Haldane liquid (HL), as first introduced in Ref. [125] for a 1D lattice gas of dipolar fermionic molecules.

The HL appears as a "fluid" precursor of a truly crystalline phase - phase (II) in Fig. 4.1 - which occurs for moderate repulsion and extreme mass imbalance; this phase is a Wigner crystal of repulsive a-$m\bar{b}$ composites, equivalent to the one discussed in Ref. [117] (see discussion of the quantum phase transition leading to it in Ref. [121]).

Our theoretical results have immediate consequences for current experiments on one-dimensional mixtures of mass-imbalanced cold atoms. Such experiments can probe both attractive and repulsive interactions, within the same experimental conditions, via the use of Feshbach resonances [43]. Our phase diagram reveals a fundamental asymmetry between the attractive and the repulsive case for weak and moderate mass imbalance, with the formation of bound pairs on the attractive side and the absence of spin gap on the repulsive one. This asymmetry is very well seen in time of flight experiments probing the momentum distributions $n_a(k)$, $n_b(k)$, which are very broad on the attractive side, while they exhibit sharp quasi-condensation peaks on the repulsive side – as shown in Fig. 4.4. This asymmetry can be used as strong evidence of *pairing* on the attractive side. A partial symmetry is recovered only for strong mass imbalance, with the opening of a spin gap in the repulsive case, and the occurrence of a crystalline phase for both signs of the interaction. This is also well captured by the momentum distributions, showing this time a suppression of the quasi-condensation peaks on the repulsive side due to

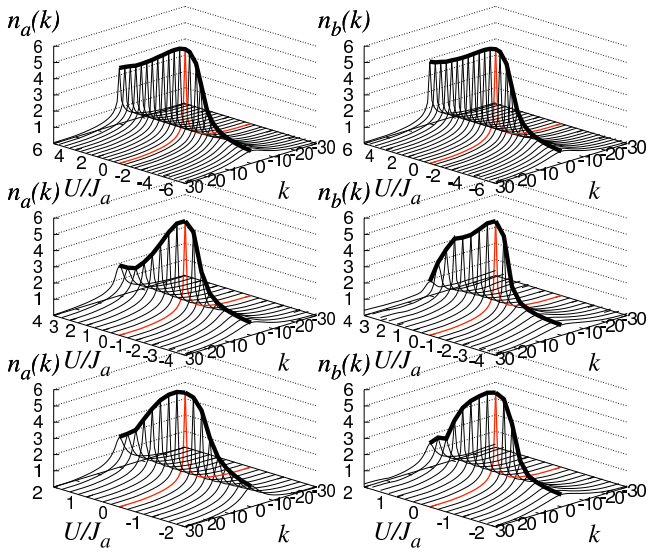

Figure 4.4: Evolution of the momentum distribution of both species on a $L = 60$ chain, for interactions spanning the repulsive and the attractive side at fixed mass imbalance. From top to bottom: $j = 2/3, 1/10, 1/20$.

the appearance of the HL phase and of the crystalline phase.

Another very attractive feature of the model in question is appearance of a gapless phase exhibiting string order (SO). Contrary to other models with SO investigated in the recent literature [126, 125] the present one has *on-site* interactions only, namely it can be realized in current experiments on van-der-Waals interacting gases. The only drawback is that *long-range* SO is very weak and very fragile to any finite temperature. Yet current cold-atom experiments can only probe short-range SO correlations due to the inhomogeneous trapping. Our simulations indicate that SO correlations are the strongest diagonal correlations in the system, and hence they will be clearly visible via spin-dependent *in-situ* imaging [127]. The requirement of simultaneous imaging of the two species is crucial to observe SO, because SO is not accompanied by density order of any of the two species separately. The evolution of short-range SO correlations is presented in Ref. [121].

Chapter 4. Pairing, crystallization and Haldane liquid of mass unbalanced atomic mixtures in one-dimensional optical lattices

Chapter 5

Three-species mixtures: a color superfluid via three-body losses.

Large three-body loss rates in a three-component Fermi gas confined in an optical lattice can dynamically prevent atoms from tunneling so as to occupy a lattice site with three atoms. This effective constraint not only suppresses the occurrence of actual loss events, but stabilises BCS pairing phases by suppressing the formation of trions. We study the effect of the constraint on the many-body physics using bosonisation and density matrix renormalisation group techniques (DMRG), and also investigate the full dissipative dynamics including loss for the example of ^{6}Li.

5.1 Three-body losses as three-body interactions

Recent developments in the experimental control of degenerate Fermi gases with cold atoms [63, 64, 80, 81, 82, 83] have paved the way for the study of three-component Fermi mixtures of different species or internal states [84, 85]. For attractive two-body interactions, these systems offer a chance to observe competition between an atomic colour superfluid phase, which has BCS pairing of different components, and a phase of trions, formed of three atoms of different colour [128, 129, 89, 90, 130, 131]. In a broader context, colour superfluids appear in different forms, e.g., in QCD [132]. A key feature of current atomic physics experiments, though (e.g., with Lithium), is the large three-body loss rate observed in these mixtures [84, 85]. Here we discuss how these high loss rates, which are normally undesirable, can give rise to an effective three-body hard-core constraint [93, 133, 92, 134] when the gas is loaded into an optical lattice [44]. This constraint would stabilise the system, suppressing three-body occupation of lattice sites,

and thus actual loss events. Moreover, trion formation will also be suppressed, enhancing pairing phases such as the atomic colour superfluid.

Below we analyze this process quantitatively, focussing on a 1D system. This focus allows us (i) to compute the phase diagram in the presence of a constraint by combining Tomonaga Luttinger Liquid (TLL) bosonisation techniques with density matrix renormalisation group (DMRG), and then (ii) to make quantitative predictions for the full non-equilibrium dynamics for realistic experimental parameters by combining time-dependent DMRG methods [135, 136, 137, 138, 139] with quantum trajectories techniques [93]. The consequences of the constraint are particularly striking in 1D because when all two-body interactions are attractive, the atomic colour superfluid (ACS) phase is normally absent in the absence of the constraint (in fact BCS correlations decay exponentially). Instead, competition is observed between a charge-density wave (CDW) and a phase with symmetric (on-site) trions (ST) [89, 90] (see Fig. 5.1 *a*). We show that the constraint prevents ST formation and produces an ACS phase with dominant, algebraically decaying BCS pairing correlations. This competes with a CDW and off-site trions (OT) (see Fig. 1b).

A three component Fermi gas in the lowest band of an optical lattice is described by the Hamiltonian ($\hbar = 1$)

$$H_U = -\sum_{\langle i,j\rangle,\sigma} J_\sigma (c^\dagger_{i,\sigma} c_{j,\sigma} + h.c.) + \sum_{i,\sigma} U_\sigma m_{i,\sigma} m_{i,\sigma+1}, \tag{5.1}$$

where $\langle i,j\rangle$ denotes a sum over neighbouring sites, $c^\dagger_{i,\sigma}, c_{i,\sigma}$ are fermionic operators with a species index $\sigma = 1,2,3$, $m_{i,\sigma} = c^\dagger_{i,\sigma} c_{i,\sigma}$, J_σ are the tunnelling amplitudes, and U_σ are the onsite interaction energy shifts. In the following, we will consider balanced densities $\bar{m}_\sigma = \bar{n}/3$ for total mean number density $\bar{n}$, and in typical realisations we will have equal tunnelling amplitudes $J_\sigma = J$. This model is valid in the limit $J_\sigma, U_\sigma \bar{n} \ll \omega$, with ω the energy separation between the lowest two Bloch bands.

Three-body recombination will result in decay into the continuum of unbound states, i.e., loss from the optical lattice. The decay dynamics can be described by a master equation in which loss occurs from a single site occupied by three atoms at a rate γ_3 [93],

$$\dot{\rho}^{(N)} = -\mathrm{i}\left(H_{\mathrm{eff}}\rho^{(N)} - \rho^{(N)} H^\dagger_{\mathrm{eff}}\right) + \gamma_3 \sum_i t_i \rho^{(N+3)} t_i^\dagger,$$

where $\rho^{(N)}$ is the system density operator for a total number of N atoms, $t_i = c_{i,1}c_{i,2}c_{i,3}$, and the effective Hamiltonian is $H_{\mathrm{eff}} = H_U - i\gamma_3 t_i^\dagger t_i/2$. If we

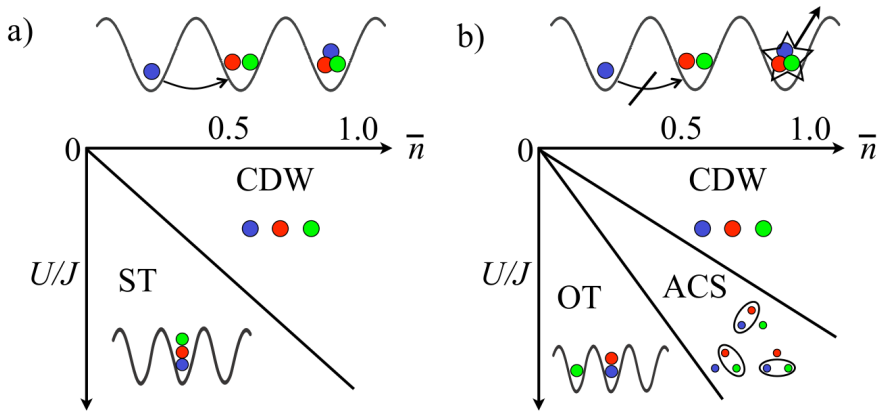

Figure 5.1: Qualitative phase diagram for attractive interactions $U < 0$ and equal populations $\bar{n}/3$ of each component in a three-component 1D Fermi gas. These are shown in the SU(3) symmetric case (where all pairwise interactions between different components are of equal strength), a) without and b) with a three-body hard-core constraint arising from three-body loss. The unconstrained case is characterised by competition between symmetric (on-site) trions (ST) and a charge-density wave (CDW). The hard-core constraint suppresses trion formation, stabilising BCS pairing in an atomic colour superfluid (ACS), which competes with a CDW and off-site trions (OT).

begin with an initial state not involving three body occupation, then via a mechanism analogous to the quantum Zeno effect, a large loss rate $\gamma_3 \gg J$ will *suppress* coherent tunnelling that would produce triply occupied sites. For large γ_3/J, loss occurs at an effective rate that decreases as J^2/γ_3 in second-order perturbation theory. Then, on a timescale $\sim \gamma_3/J^2$ where loss can be neglected, the system dynamics is described by the constrained Hamiltonian

$$H_C = \mathcal{P} H_U \mathcal{P}, \quad \mathcal{P} = \prod_j \mathcal{P}_j = \prod_j (1 - m_{j,1} m_{j,2} m_{j,3}),$$

where $\mathcal{P}$ is a projector onto the subspace of states with at most two atoms per site.

5.2 Phase diagram in the constrained regime

Below we first compute the ground state of H_C and determining the phase diagram in the presence of a perfect constraint. We treat both the SU(3)

symmetric case where all interaction constants are equal (as could be realised, e.g., with nuclear spin states in alkaline earth atoms [140]), and the case where interactions are unequal (as are typical in Lithium experiments at low magnetic fields [84, 85]). We then return to the full picture of the non-equilibrium dynamics by computing time evolution under the master equation. This both allows us to test the assumption that loss probabilities are small on relevant experimental timescales, and to investigate time-dependent preparation of states. In particular, we investigate the production of an ACS state for the case of ^{6}Li for typical experimental parameters.

In 1D, the phase diagram is determined by identifying the dominant order in the system in different parameter regimes. To do this, we consider the behavior of correlation functions, and determine which is the strongest at long distances. The orders shown in Fig. 5.1 *b* are: CDW for which we compute the correlation function $C(x) \propto \langle n_i n_{i+x} \rangle$ of the total density operator $n_i = \sum_\alpha m_{i,\alpha}$, ACS with BCS correlations $P_\sigma(x) \propto \langle d^\dagger_{i,\sigma} d^\dagger_{i,\sigma+1} d_{i+x,\sigma} d_{i+x,\sigma+1} \rangle$ and OT with $OT(x) \propto \langle \tilde{t}^\dagger_{i,\sigma} \tilde{t}_{i+x,\sigma} \rangle$ with $\tilde{t}_{i,\sigma} = d_{i,\sigma} d_{i,\sigma+1} d_{i+1,\sigma+2}$. Below we determine the behavior of these correlation functions via bosonisation and DMRG methods, determining whether the decay is exponential or algebraic, and finding decay exponents $\mathcal{D}_{CDW}$, $\mathcal{D}_{ACS}$, and $\mathcal{D}_{OT}$ in the case of the latter.

5.2.1 Bosonisation formalism for the constrained Hamiltonian

In order to apply the bosonisation formalism we identify an exact mapping of the constrained fermionic Hamiltonian H_C to an unconstrained fermionic Hamiltonian which automatically respects the constraint, at the expense of including higher order interactions. We introduce projected operators $d^\dagger_{i\sigma} = (\prod_{j \neq i} \mathcal{P}_j) c^\dagger_{i\sigma}$, $d_{i\sigma} = (\prod_{j \neq i} \mathcal{P}_j) c_{i\sigma}$, entirely in terms of which we express the Hamiltonian. We verify (i) that the operators $d_{i\sigma}$ obey fermionic commutations on the subspace where at most two atoms occupy any site, and that (ii) the Hamiltonian has vanishing matrix elements in the space with occupations greater than two and (iii) acts as zero on any state in this latter space. Thus, we arrive at a fermionic Hamiltonian with built-in constraint, which we analyse with standard bosonisation techniques. Here we summarise the results, with the calculations presented in more detail in a forthcoming work [141]. We introduce three bosonic fields $\phi_\sigma(x)$ related to the continuum version of $(d^\dagger_{i\sigma}, d_{i\sigma})$, from which we can construct a Hamiltonian by taking the linear combinations

$\phi_c = (\phi_1 + \phi_2 + \phi_3)/\sqrt{3}$, which represents collective fluctuations of the total density, and $\phi_{s1} = (\phi_1 - \phi_2)/\sqrt{2}$ and $\phi_{s2} = (\phi_1 + \phi_2 - 2\phi_3)/\sqrt{6}$, which represent the spin sectors. If we define TLL parameters K_α and conjugate momentum fields Π_α corresponding to each field ϕ_α ($\alpha \in \{c, s1, s2\}$), we then obtain

$$\begin{aligned} H &= \sum_{\alpha=c,s1,s2} \left\{ \frac{v}{2}[K_\alpha \Pi_\alpha^2 + \frac{1}{K_\alpha}(\partial_x \phi_\alpha)^2] \right\} + \\ &- \frac{2g_{ss}}{a^2} \cos[\sqrt{2\pi}\phi_{s1}] \cos[\sqrt{6\pi}\phi_{s2}] - \frac{g_s}{a^2} \cos[\sqrt{8\pi}\phi_{s1}], \end{aligned}$$

where $v = 2aJ \sin[\pi\bar{n}/3]$ is the Fermi velocity, a is the lattice spacing. The coefficients g_{ss} and g_s exhibit non-trivial dependence on U/J and $\overline{m}_\sigma$, as do K_α.

The dependence of the decay exponents for different orders on K_α can be extracted from the formalism, and by expanding K_α in the weak interaction limit we obtain also the dependence on U/J and $\bar{n}$. We will present these formulas, which are not very compact, in a longer article [141]. The key results are summarised in the paragraph below, and are benchmarked against values extracted from numerical simulations in Table I.

5.2.2 Phase diagram from bosonisation

For comparison, the qualitative phase diagram for attractive interactions $U_\sigma < 0$ in the absence of the hard-core constraint is depicted in Fig. 5.1 *a*. There are two phases, one with symmetric (on-site) trion (ST) order and the other with charge-density-wave (CDW) order, which actually cross over into one another, the transition line marking where algebraic decay is equally strong. This was previously studied for equal attractive interactions using a combination of the TLL formalism and DMRG methods [89, 90]. In a wide region near the SU(3) symmetric line $U_\sigma = U < 0$, CDW is dominant for higher densities and intermediate interactions. A particular feature of this case is that a gap appears in the entire spin sector, so that in contrast to a two-species Fermi gas, ACS correlations decay exponentially (as do spin-density wave correlations).

In the presence of the constraint this picture changes substantially (see Fig. 5.1 *b* with small $|U/J|$). The ST phase is suppressed by the constraint, and for most regions of the diagram the spin sector is gapless, so that all correlations decay algebraically. We observe competition between an OT, a CDW, and an ACS phase, which for equal interactions involves simultaneous pairing of all three pairs of components. The only exception to this

is at low densities $\bar{n} < 0.2$ and intermediate interactions, where bosonization results predict a second order transition below which ACS correlations again decay exponentially and OT correlations dominate over CDW correlations. At higher densities, there is a crossover from the ACS to the CDW phase. In the case of unequal interactions, the charge sector and two spin sectors are coupled [141]. For sufficiently strong imbalance in U_α a gap in the spin sector may open, so that only BCS-pairing for the channel with the largest $|U_\alpha|$ survives.

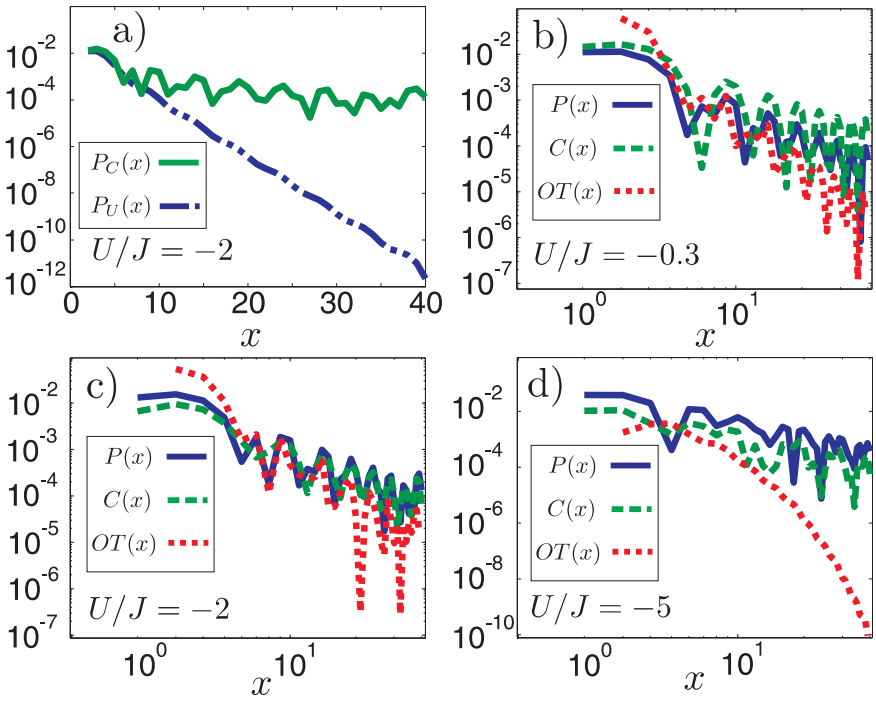

Figure 5.2: a) ACS-correlations $P_\sigma(x)$ with (solid line) and without (dash-dotted line) the three-body constraint as a function of distance x on a 40 site lattice. b) - d) $P_\sigma(x)$ with CDW-correlations $C(x)$ and off-site trion correlations $OT(x)$ for different values of U, at a density $\bar{m}_1 = \bar{m}_2 = \bar{m}_3 = 0.2$, with the constraint. In qualitative agreement with bosonisation, we observe that for weak coupling (b) CDW clearly dominates. As the coupling is increased (b-d), ACS appears to dominate. For the values shown here, ACS dominates off-site trions, with $OT(x)$ decaying exponentially for strong coupling.

5.2.3 Ground state of H_C from DMRG (equal interactions)

To underpin these results quantitatively and go beyond weak-coupling, we present calculations based on DMRG methods [135, 136, 137, 138, 139]. In Fig. 5.2, we see again the striking comparison between the ACS correlations in the ground states for H_U and H_C, which exhibit exponential decay without the hard-core constraint, and algebraic decay in the presence of the constraint. In Figs. 2b-c we show a comparison of the correlations corresponding to the ACS ($P_\sigma(x)$), CDW ($C_\sigma(x)$) and OT ($OT(x)$), in the ground state of the model with a three-body hard-core constraint (H_C). These are presented for symmetric but varying interactions from weak to strong coupling, $U/J \in [-10, -0.3]$. For increasing interactions, the values of $P_\sigma(x)$ become larger with respect to $C_\sigma(x)$, so that the ACS appears to dominate for stronger interactions. While off-site trions still show algebraic decay for $U/J \geq -2$, they are subdominant to the ACS and CDW, and they decay exponentially for $U/J \leq -5$ (Figs. 5.2 *b-d*). This is a strong deviation from the weak-coupling bosonisation results, and could indicate an instability (e.g., towards phase separation), or the appearance of a gap in the dual field of the charge sector. However, with system sizes of 40 lattice sites, we have not observed any evidence of phase separation.

Extracting the exponents of the algebraic decay of the correlation functions further confirms this picture, as shown in Table 1. The constrained model sees an enhancement of ACS correlations with decreasing U, while CDW correlations generally decay faster as U is lowered. In the weak coupling regime we also generally observe good agreement with the perturbative values of the exponents from TLL-theory. In the strong coupling regime ($U/J \leq -5$) for the constrained case, the exponents $\mathcal{D}_{ACS}$ and $\mathcal{D}_{CDW}$ saturate, with $\mathcal{D}_{ACS}$ taking a value compatible with the TLL prediction.

5.2.4 Ground state of H_C from DMRG (unequal interactions)

In the case of asymmetric interactions we also observe an ACS pairing, but with only the two components paired that exhibit the strongest interactions. As an example, we consider the case of ^{6}Li, where in Fig. 5.3 *a* we plot the Hamiltonian parameters as a function of magnetic field strength near 500-700 G for a fixed lattice depth. From the pairing correlations shown in Fig. 3b, we see that at 500 G, the only algebraically decaying correlations are those corresponding to components 1 and 3, which have the strongest interparticle interaction.

$-U/J$	$\mathcal{D}_{ACS}$	$\mathcal{D}_{CDW}$	$\mathcal{D}_{OT}$
0.3	1.71(0.02)/2.04	1.39(0.02)/1.95	3.3(0.3)/3.00
0.6	1.66(0.02)/2.03	1.40(0.03)/1.96	3.3(0.3)/3.00
1	1.60(0.02)	1.40(0.03)	3.1(0.4)
2	1.4(0.2)	1.4(0.1)	3.0(0.4)
5,8,10	1.4(0.4)	1.4(0.3)	exp

Table 5.1: Exponents for algebraic decay of correlations, computed for ground states in a system of 40 lattice sites with $\bar{m}_\sigma = 0.2$ by fitting a power law to the periodic peaks of the correlations (see Fig. 5.2). Errors are given in parentheses, analytic values in the weak coupling limit are given to the right of slashes. We find agreement with the qualitative predictions of analytic theory, i.e. for weak coupling we start out with the CDW-phase dominant, from where $\mathcal{D}_{CDW}$ remains constant whilst $\mathcal{D}_{ACS}$ and $\mathcal{D}_{OT}$ decrease with increasing $|U/J|$. We further observe a transition to exponential decay for the off-site trions in the strong coupling limit.

5.2.5 Time-dependent preparation of an ACS phase with ^{6}Li

Considering this example, we now return to the full time-dependent dynamics including three-body loss, in order to demonstrate a method to produce these ACS states in ^{6}Li. We simulate the many-body master equation on 12-24 lattice sites by combining time-dependent DMRG methods with quantum trajectories techniques, as described in [93]. We assume that the lattice is initially loaded at a magnetic field of 615 G, where the repulsive interactions (see Fig. 5.3 *a*) will stabilise the system in the presence of loss. We then consider a time-dependent ramp of the magnetic field to 500 G. The characteristics of the ramp we choose (shown in Fig. 5.3 *c*) are: (i) it is adiabatic until 565 G, where the components 2 and 3 become paired, (ii) it is fast from $565 - 500$ G, where onsite trions become energetically favored ($\sum_\alpha U_\alpha < U_2$) and where for fields larger than 520 G, γ_3 is too small to prevent triple occupation (see Fig. 5.3 *a*), and (iii) after a hold time $T_{h,1} = 16J^{-1}$ we add a swap between species 1 and 2 via a fast laser pulse at the end of the ramp, after which there is a second hold time $T_{h,2} = 20J^{-1}$. The ACS correlations in the final state after the swap (Fig. 5.3 *d*) then exhibit dominant pairing between species 1 and 3, as would be expected in the ground state for the parameters of ^{6}Li at $B = 500$ G with the constraint. The other pairing channels are clearly subdominant, and trion formation is also strongly suppressed during the ramp ($\max(T(x)) \approx (O)(10^{-8})$). The probability that no decay event occurs during the ramp shown here for 12

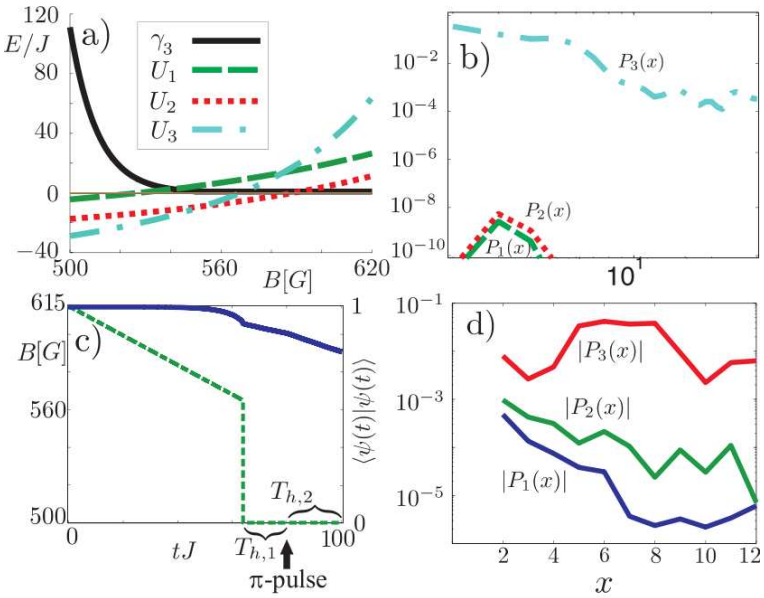

Figure 5.3: a) Hubbard parameters U_1, U_2, U_3 and three-body loss rate γ_3 for ^{6}Li as function of external magnetic field B, for a lattice depth of $V_{ax} = 5\ E_R$ in axial direction, and $V_{rad} = 20\ E_R$ in radial direction. b) ACS correlations for the ground state of H_C at $B = 500\ G$, computed for a system of 30 lattice sites, $\bar{m}_\sigma = 2/15$, $\sigma = 1, 2, 3$. The dash-dotted line shows $P_3(x)$, dashed line $P_1(x)$, dotted line denotes $P_2(x)$. As $U_3 < U_2 \ll U_1$, we see $1 - 3$ pairing dominate, with all other pairing exponentially suppressed. c) Left scale, dashed line: Magnetic field $B(t)$ for the ramp. Right scale, solid line: Probability of no three body loss having occurred at time t. d) ACS correlations after the time-dependent ramp of the magnetic field shown in d), beginning from the ground state at 615 G, with $\bar{m}_\sigma = 0.167$, on 12 sites.

lattice sites is 79%.

In higher dimensions, we expect that actual losses will be suppressed on a lattice by the effect discussed here, and that the ACS phase [128, 129] will also be stabilised due to suppressed trion formation.

5.3 Addendum: detailed constraint mapping

In order to implement correctly the constraint onto the model, we can define an Hamiltonian that embodies the constraint itself via non-local pro-

jectors:

$$H = \mathcal{P} H_{Hubbard-3species} \mathcal{P} \tag{5.2}$$

or alternatively, insert a strong repulsion term:

$$\sum_i \Gamma_3 n_{Ii} n_{IIi} n_{IIIi}$$

to avoid triple occupancies. In the following, we will first take a quick look on the effect of this type of term and then we will proceed studying (5.2) in the weak coupling limit.

5.3.1 Toy model: $\Gamma_3 \to \infty$

Considering simply a standard 3-species hamiltonian with a term:

$$\sum_i \Gamma_3 n_{Ii} n_{IIi} n_{IIIi}, \qquad \Gamma_3 \gg 1$$

we have simply that the spin sector become gapless and the charge sector has $\lambda_c \gg 1, \quad K_c \sim 0$. Inserting an ultra strong coupling in the theory can be anyway a problem, our interest being studying the interplay between the interaction t, U and the populations n.

5.3.2 Effective theory and pseudofermionic mapping

Suppose now that we want to treat the original hamiltonian exactly, that is we start from:

$$H = \prod_{j=1}^{L} (1 - M_j) \left[\sum_{i=1}^{N} H_i \right] \prod_{k=1}^{L} (1 - M_k) \tag{5.3}$$

$$M_j = m_{Ij} m_{IIj} m_{IIIj}, \qquad m_{\alpha j} = c^\dagger_{\alpha j} c_{\alpha j}, \qquad P_j \equiv 1 - M_j$$

$$H_i = -t \sum_{i\alpha} (c^\dagger_{i\alpha} c_{i+1\alpha} + h.c.) + \sum_{i,\alpha} U_\alpha m_{i\alpha} m_{i\alpha+1}$$

This hamiltonian clearly acts only on the physical subsector of the Hilbert space, that is it extracts the correct information from the partition function. In this picture, we have not strong interactions so we can proceed to a low coupling treatment; anyway, the non-locality induced by the projectors

should be somehow embedded into *local* terms. Let's now consider a new set of operators:

$$d^\dagger_{\alpha j} = \prod_{k\neq j} P_k c^\dagger_{\alpha j}, \qquad d_{\alpha j} = \prod_{k\neq j} P_k c_{\alpha j}$$

that present the following commutation relations when applied on physical or unphysical states:

$$\{d^\dagger_{i\alpha}, d_{j\beta}\} \;=\; (\prod_{k\neq i,j} P_k)[c^\dagger_{i\alpha} P_i P_j c_{j\beta} + c_{j\beta} P_j P_i c^\dagger_{i\alpha}] \prod_{k'\neq i,j} P_{k'}$$

then

$$\{d^\dagger_{i\alpha}, d_{j\beta}\}_U = 0 = \{d^\dagger_{i\alpha}, d_{j\beta}\}_P$$

and the analog holds for commutators involving creation and annihilation operators. On the same site, we have:

$$\{d^\dagger_{i\alpha}, d_{i\beta}\} = (\prod_{k\neq i} P_k)[c^\dagger_{i\alpha} c_{j\beta} + c_{j\beta} c^\dagger_{i\alpha}](\prod_{k'\neq i} P_{k'})$$

that leads to:

$$\{d^\dagger_{i\alpha}, d_{i\beta}\}_{U_{k\neq i}} = 0, \qquad \{d^\dagger_{i\alpha}, d_{i\beta}\}_P = \delta_{\alpha\beta} = \{d^\dagger_{i\alpha}, d_{i\beta}\}_{U_i}$$

We have then proved that, on the physical part of the Hilbert space, these operators act like fermions, whereas on the unphysical part, due to the previous relation, they act like *quasi-fermions*. Due to the fact that only the physical space is now relevant, we can treat then as real fermionic operators. Before considering the total hamiltonian, let's remark the following properties:

$$m_{\alpha j} \prod_{k\neq j} P_k = n_{\alpha j}, \qquad n_{\alpha j} \equiv d^\dagger_{\alpha j} d_{\alpha j}, \qquad E_i = 1 - n_{1i} n_{2i} n_{3i}$$

$$E_i = 1 - m_{1i} m_{2i} m_{3i} \prod_{k\neq i} P_k$$

$$P_i(\prod_{j\neq i} P_j) = (1 - m_{1i} m_{2i} m_{3i} \prod_{k\neq i} P_k)(\prod_{j\neq i} P_j) = E_i(\prod_{j\neq i} P_j) \tag{5.4}$$

$$E_i d^\dagger_{i\alpha} = d^\dagger_{i\alpha} - d^\dagger_{i\alpha} n_{i\beta} n_{i\gamma} = d^\dagger_{i\alpha}(1 - n_{i\beta} n_{i\gamma})$$

$$d_{i\alpha} E_i = d_{i\alpha} - d_{i\alpha} n_{i\beta} n_{i\gamma} = d_{i\alpha}(1 - n_{i\beta} n_{i\gamma})$$

We can now rewrite (5.3) as a function of these new operators starting from the hopping term:

$$\begin{aligned}
K &= -t\sum_{i,\alpha} P_iP_{i+1}(\prod_{j\neq i,i+1} P_j)[c^\dagger_{i\alpha}c_{i+1\alpha}+h.c](\prod_{j\neq i,i+1} P_j)P_iP_{i+1} = \\
&= -t\sum_{i\alpha}\left[P_i(\prod_{j\neq i} P_j)c^\dagger_{i\alpha}c_{i+1\alpha}(\prod_{j\neq i+1} P_j)P_{i+1}+P_{i+1}(\prod_{j\neq i+1} P_j)c^\dagger_{i+1\alpha}c_{i\alpha}(\prod_{j\neq i} P_j)P_i\right] = \\
&= -t\sum_{i\alpha}\left\{E_i(\prod_{j\neq i} P_j)c^\dagger_{i\alpha}c_{i+1\alpha}(\prod_{j\neq i+1} P_j)E_{i+1}+E_{i+1}(\prod_{j\neq i+1} P_j)c^\dagger_{i+1\alpha}c_{i\alpha}(\prod_{j\neq i} P_j)E_i\right\} = \\
&= -t\sum_{i\alpha}\left[E_id^\dagger_{i\alpha}d_{i+1\alpha}E_{i+1}+E_{i+1}d^\dagger_{i+1\alpha}d_{i\alpha}E_i\right] = \\
&= -t\sum_{i\alpha}\left[(d^\dagger_{i\alpha}d_{i+1\alpha}+h.c.)(1-n_{i\alpha+1}n_{i\alpha+2})(1-n_{i+1\alpha+1}n_{i+1\alpha+2})\right]
\end{aligned}$$

It is easy to check that:

$$K|\psi\rangle_U = 0$$

For the potential part, we got:

$$\begin{aligned}
U &= \sum_{i\alpha} U_\alpha P_i(\prod_{j\neq i} P_j)m_{i\alpha}m_{i\alpha+1}(\prod_{j\neq i} P_j)P_i = \\
&= \sum_{i\alpha} U_\alpha E_i(\prod_{j\neq i} P_j)m_{i\alpha}m_{i\alpha+1}(\prod_{j\neq i} P_j)E_i = \\
&= \sum_{i\alpha} U_\alpha E_in_{i\alpha}n_{i\alpha+1}E_i = \\
&= \sum_{i\alpha} U_\alpha n_{i\alpha}n_{i\alpha+1}(1-n_{i\alpha+2})
\end{aligned}$$

and again:

$$U|\phi\rangle_U = 0$$

Then, the final effective hamiltonian in terms of d's operator is:

$$\begin{aligned}
H_{eff} &= -t\sum_{i\alpha}\left[(d^\dagger_{i\alpha}d_{i+1\alpha}+h.c.)(1-n_{i\alpha+1}n_{i\alpha+2})(1-n_{i+1\alpha+1}n_{i+1\alpha+2})\right]+ \\
&+ \sum_{i\alpha} U_\alpha n_{i\alpha}n_{i\alpha+1}(1-n_{i\alpha+2}) \qquad (5.5)
\end{aligned}$$

with the same initial fillings for the different species.

Chapter 6

Outlook: quantum magnetism and Bose-Bose mixtures

Quantum magnetism is an old and fascinating problem in many-body physics, in deep connection with various phenomena such as HTc, topological order etc.. However, its observation in cold atomic setups is quite challenging due to the relative strength of the exchange interaction with respect to temperature of the order of $10nK$. Furthermore, the role of the trapping potential is crucial for, e.g., antiferromagnetic phases, where different type of commensurabilities must be realized at the same time. In the following, we present preliminary datas on a numerical analysis of 1D strongly asymmetric Bose-Bose mixtures, which in principle allow for the observation of various magnetic phases. While our final interest is in understanding the inhomogeneous situation, we will first focus on the homogeneous one, considering as an example a strongly asymmetric mixture comparable with a ^{87}Rb-^{41}K mixture currently available at the LENS laboratory in Florence[142].

6.1 Bose-Bose mixtures: phase diagram from bosonization

The qualitative phase diagram from bosonization for Bose-Bose mixtures does not different substantially from the fermionic one, except for the fact that gapless regimes usually correspond to standard single species superfluid order, which is forbidden for fermions. Provided that interspecies interaction are repulsive, the main instabilities are:

- *super-counterflow*(SCF) phase; namely, a superfluid gas of particle-

Phases	Δ_c	Δ_s	K_c	K_s
2TLL	0	0	> 1	> 1
SCF	$\neq 0$	0	–	> 1
AFM	$\neq 0$	$\neq 0$	–	–

Table 6.1: Properties of homogenous phases of a two-species Bose-Bose mixture.

hole pairs, which does not require equal densities but only commensurate ones;

- *antiferromagnetic Neel phase*(AFM), analog of the standard XXZ phase, characterized by a fixed order $abababa...$;
- *ferromagnetic phase*(FM), which in our case corresponds to phase separation(PS).

While PS is not captured by a TLL formalism (in fact, it does correspond to a breakdown of the theory[143]), the AFM phase corresponds to two-gapped sectors, whereas SCF corresponds to a gapped charge sector, the spin one being gapless. In the following, we will concentrate on equal and commensurate populations $n_1 = n_2 = 1/2$; in that case, the additional requirement $K_s > 1$ has to be satisfied in the SCF phase.

6.2 Numerical analysis

In the following, we present some DMRG results on the homogeneous phase diagram of the following lattice Hamiltonian:

$$H = -\sum_{\alpha=1,2}\sum_i t_\alpha(b^\dagger_{i,\alpha}b_{i+1,\alpha} + h.c.) + U_{12}\sum_i n_{i,1}n_{i,2} + \sum_\alpha \frac{U_\alpha}{2}\sum_i n_{i,\alpha}(n_{i,\alpha}-1) \tag{6.1}$$

for strongly asymmetric configurations, which usually favors AFM ordering. Our analysis is mainly based on the estimate of the spin and charge gap in the thermodynamic limit, which combines finite size calculations with a subsequent extrapolation. The finite size charge and spin gaps are defined as:

$$\Delta_{\mathrm{C}} = \frac{E(N_{\mathrm{A}}+1, N_{\mathrm{B}}+1) + E(N_{\mathrm{A}}-1, N_{\mathrm{B}}-1) - 2E(N_{\mathrm{A}}, N_{\mathrm{B}})}{2} \tag{6.2}$$

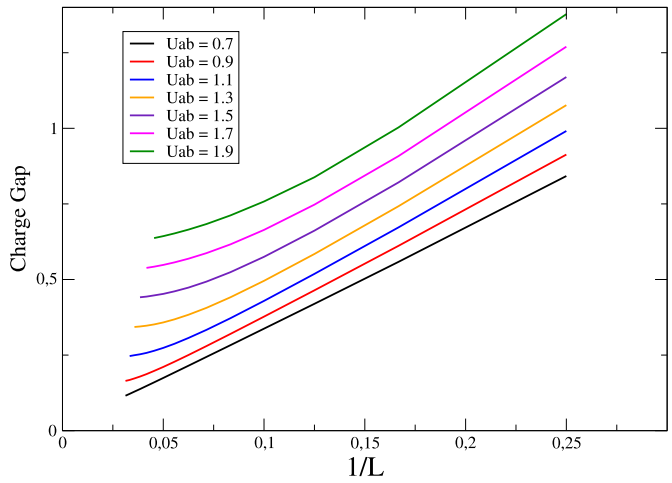

Figure 6.1: Δ_c scaling as a function of $1/L$ for different interspecies interaction U_{12}.

$$\Delta_{\mathrm{S}} = \frac{E(N_{\mathrm{A}}-1, N_{\mathrm{B}}+1) + E(N_{\mathrm{A}}+1, N_{\mathrm{B}}-1) - 2E(N_{\mathrm{A}}, N_{\mathrm{B}})}{2}. \tag{6.3}$$

Once the thermodynamic limit is extrapolated (as a example, see Fig. 6.1), one can argue the phase diagram according to Table 6.1.

6.2.1 Phase diagram at equal densities

At first instance, it is interesting to discuss what happens in 6.1 when one changes U_{12}. In Fig. 6.2, we plot the spin and charge gap for a sample configuration with $t_1 = 0.024, U_2 = 11.08$, with $t_b = 2$ as the energy unit and the a-species in the hard-core limit. Both gaps open at small values of U_{12}, signaling that the SCF region is narrow; remarkably, Δ_s is non monotonic in U_{12}, and it closes at strong coupling, signaling that the AFM phase is embedded between 2 SCF regions. This second transition point, we should belong to the BKT universality class, is in good accordance with a perturbative expansion based on the XXZ spin-$1/2$ model[144].

We are now applying the same method in order to accurately shape the ^{87}Rb-^{41}K 1D phase diagram; an advantage of this method is that it can give rather good estimates on the critical temperature needed to stabilize magnetism, which is usually smaller than the gaps which protect long-range order.

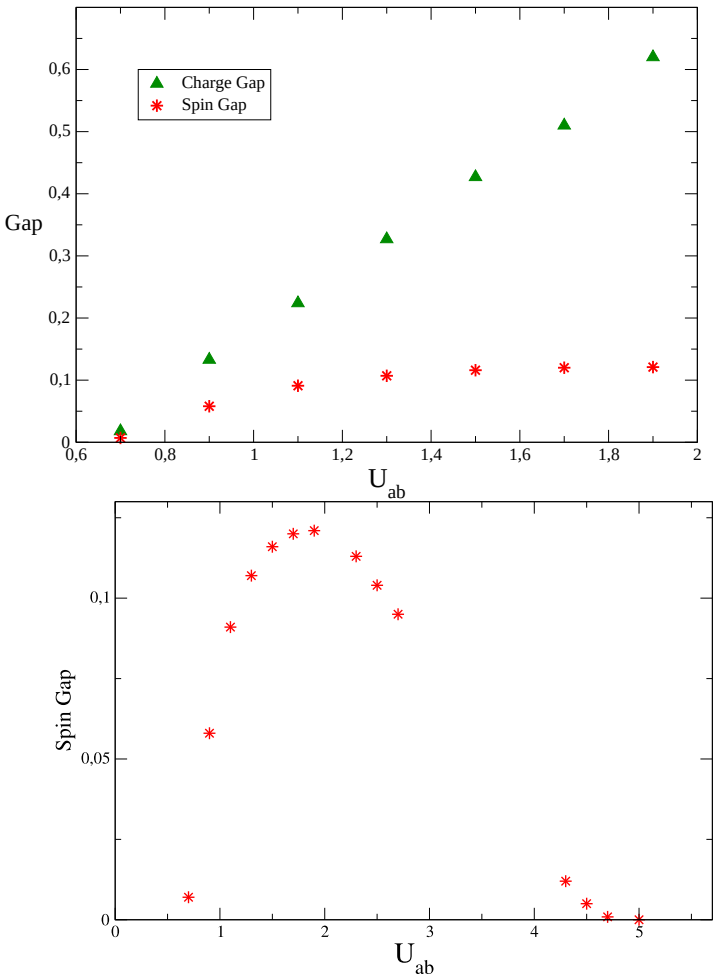

Figure 6.2: Thermodinamic values of the gaps as a function of U_{12}. *Upper panel*: Δ_c (green triangles) and Δ_s (red circles). *Lower panel*: spin gap.

Part III

Long-range interacting systems in 1D and quasi-1D geometries

As we have seen in the previous chapters, ultracold atoms are very well suited to investigate and eventually simulate many-body physics with a high degree of tunability and control. There is, however, a severe limitation, which makes the observation of several phenomena, such as, e.g., quantum magnetism and supersolidity, challenging. In fact, despite the refined use of Feshbach resonances, the interaction in these setups is always characterized by a very small effective range: in a standard optical lattice of height $V \simeq 5E_r$, the overlap of nearest-neighbor Wannier functions is usually 3 order of magnitudes smaller than the typical onsite contribution.

One of the main experimental advances of the last decade has been the possibility to trap and control cold gases in which interactions are not restricted to standard scattering processes, but are instead non-local in nature. The first remarkable example is represented by *magnetic atoms*. Usually, alkali atoms in the ground state have a magnetic moment of the order of the Bohr magneton μ_B, so that the energy scale associated with dipolar magnetic interaction is much smaller than all other ones which come into play. However, other atoms such as Dy, Cr or Er have much larger magnetic dipole moments in their ground state, so that dipolar effects may become tangible and influence both static and dynamical properties [145]. The first example of such a possibility has been shown in [146], where a BEC of ^{52}Cr atoms was prepared and the subsequent expanding dynamics of the cloud revealed dipolar effects. Up to date, the only magnetic atoms which have been Bose-condensed are Cr and Dy [146, 147, 148], but the field is in rapid progress, and new elements such as Er are currently under investigation.

While magnetic atoms have shed some light into the realm of long-range interactions, the limited magnitude of the dipole-dipole interaction between them still limits their range of applicability to many-body problems. On the contrary, heteronuclear molecular gases do not suffer from this disadvantage, and can present electric dipole moments orders of magnitude larger than the magnetic one in ^{52}Cr or Dy [145]. While no BEC nor degenerate Fermi gas has yet been realized in the laboratory, major progress in this direction includes the realization of high-density samples of homonuclear Cs^2 molecules in their rovibrational ground state [149] and an efficient laser cooling of a single SrF molecule [150]. Up to now, the most promising approach toward a high-density sample of heteronuclear, polar molecules consists in starting from an already ultracold two-species atomic mixture and then employ a Feshbach resonance to create molecules, which are finally cooled down to their rovibrational ground state by a photoassociation process known as STIRAP. Remarkable results have been already obtained in Freiburg [151] with LiCs and, in particular,

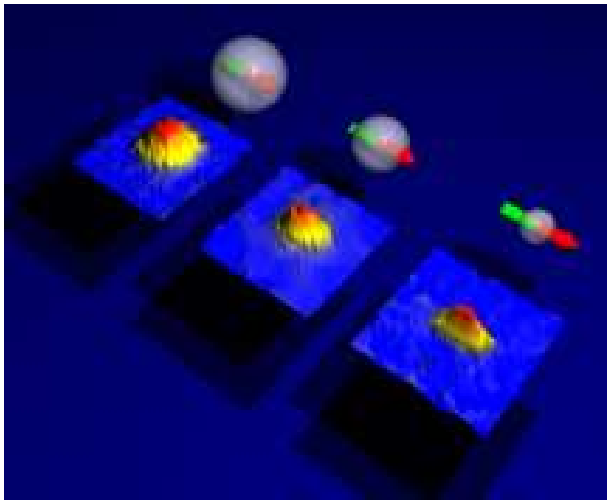

Figure 6.3: Density profile of a ^{52}Cr Bose-Einstein condensate as a function of the isotropic contact interaction tuned via Feshbach resonance[152]. In the cartoons, the green-red arrow denotes the magnetic dipole moment (which remains constant) and the grey area indicates how large the contact interaction contribution is. In the top case, isotropic interactions dominates, whereas in the lower case, the dominant contribution comes from anisotropic dipolar interactions, which induces a direct signature in the strongly anisotropic cloud aspect ratio. Image taken from Tilman Pfau's website.

at JILA with fermionic RbK molecules [153, 154].

The benchmark realization and control of degenerate, ultracold gases of polar molecules would open the door to the study of several quantum phenomena, its application ranging from quantum computing to ultracold chemistry and few-body physics (for a complete review, see Ref. [155] and related articles on the same issue). At the many-body level, these gases allow to investigate a series of complex behaviors which are usually connected to non-local interactions such as supersolidity, quantum magnetism (without any intrinsic temperature limitation, contrary to ultracold atomic gases), bilayer and multilayer physics [145, 156, 157]. A typical example is shown in Fig. 6.4, in which the phase diagram of the extended Bose-Hubbard model(EBH):

$$H_{EBH} = -J \sum_{<i,j>} (b_i^\dagger b_j + h.c.) + \mu \sum_i n_i + V \sum_{i \neq j} \frac{n_i n_j}{d(i-j)^3} \qquad (6.4)$$

is presented as a function of the hopping rate J, the chemical potential μ

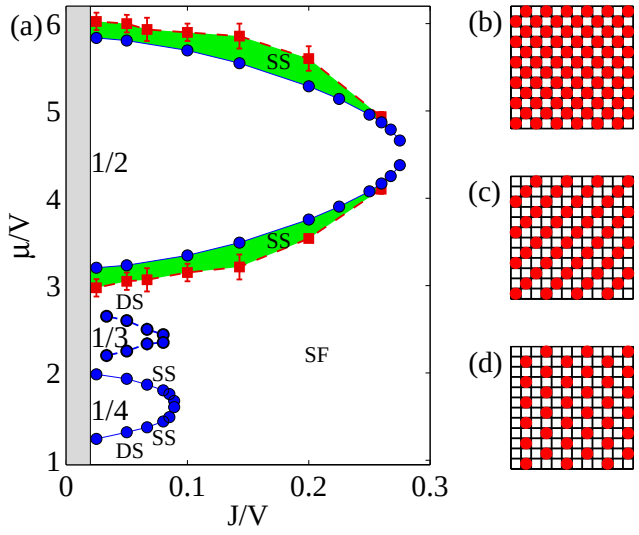

Figure 6.4: Phase diagram of bosonic dipoles in a 2D square lattice as a function of the chemical potential μ and the hopping J with respect to the dipolar interaction strength V; the system remains superfluid as long as the hopping rate is large enough, and eventually orders into a regular patter forming a crystal in the strongly interacting regime for each rational filling; sample configurations are sketched in Panels *b, c, d*. In addition, a supersolid phase appears around he Mott lobes. Image courtesy of G. Pupillo, taken from [158].

and the dipole-dipole interaction strength V ($d(i-j)$ represents the distance between points i and j on a plane) in the case of a 2D square lattice with dipole moments aligned perpendicularly to the plane itself. Even in this simple case, the phase diagram includes checkboard (Mott insulators with less than one particle per site) and supersolid phases which are hardly realizable with purely contact interactions.

However, since we are not dealing with atoms anymore but molecules, undesirable chemical reactions can play a major role by enhancing inelastic processes in certain parameter regimes due to the anisotropic nature of dipole-dipole interactions: the related losses could then affect the stability of the entire system, preventing a clear observation of equilibrium and non-equilibrium properties. A typical example is shown in Fig. 6.5: in the case of a 3D gas of RbK molecules, the loss rate increases with the interaction strength, so that the strongly interacting regime suffers from strong two-body losses. However, in reduced dimensionality such as 2D pan-

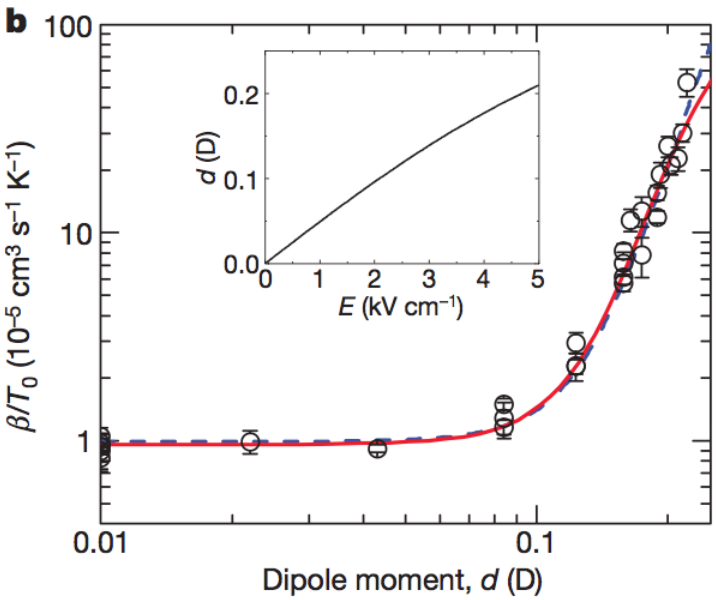

Figure 6.5: Inelastic loss rate β (in scale of the initial temperature T_0) as a function of the dipole moment d for RbK polar molecules in the rovibrational ground state; dashed and solid lines represent quantitative theoretical predictions. The inset describes the dipole moment dependence on the applied electric field. Image taken from Ref. [153].

cakes or 1D tubes, inelastic collisions can be suppressed when the dipole moments are aligned perpendicularly to each other, so that the strong in-plane repulsion prevent molecules from coming too close to each other [159, 160]. In addition, this setup allows to investigate mixed dimensionality systems, such as multilayer (quasi-2D) and multitube (quasi-1D) configurations [145].

In this final part, we will investigate several effects related to dipolar interactions in 1D and quasi 1D geometries from a many-body point of view. While the methods applied here are essentially the same as in the previous parts, the non-trivial effects of long-range interactions reveals drastic effects related to several observables in a physical systems [161].

In Chapter 7, we will consider the simplest configuration, namely a single species gas confined in a purely 1D tube where the interparticle potential is proportional to $1/r^{\beta}$. The case $\beta = 1$ has been already investigated in the context of two-species electron gases in a seminal paper by Schulz[162], where the appearance of strong deviations from the

Tomonaga-Luttinger liquid (TLL) universality class have been shown to lead to the formation of so called *Wigner crystal*, driven by ultraviolet divergences of the Coulomb potential in 1D. For $\beta > 1$, the potential is instead integrable, and a proper description of the system can be given in term of a TLL; we will present a procedure which allow to calculate the corresponding TLL parameter for arbitrary densities, shape and strength of the interaction, and compare our results with both numerical simulations and the exact solution at $\beta = 2$ (Calogero-Sutherland model [187, **?**]). We will then discuss the appearance of a Devil's staircase-like structure in presence of an optical lattice, which shows remarkable differences with respect to the classical one, by employing a mapping to the sine-Gordon model, and we finally discuss what type of insulating states can be detected in state of art experiments with Feshbach and polar molecules.

In Chapter 8, we discuss what happens in quasi-1D geometries known as ladders. By combining analytical and DMRG techniques, we first explore the equal density phase diagram, revealing strong parallelisms with bilayer physics and underlying how long-range interactions affect pairing and crystalline instabilities. Then, we analyze the unbalanced case, exploring the possibility to stabilize ground states characterized by exotic bound states composed by more than two particles. In particular, we find out that a trimer liquid is stable in a wide region of the phase diagram, and surprisingly survives even in presence of a trapping potential.

Finally, in Chapter 9, we will investigate the effect or three-body losses in a bosonic system with attractive onsite interactions. By employing an exact mapping to a spin-1 chain, we will show how ferromagnetic, antiferromagnetic and Haldane-like phases can be stabilized in a such a setup, deriving the complete commensurate phase diagram with DMRG simulations, and comparing its strong coupling limit with a simpler nearest-neighbor interaction approximation. Remarkably, these phases turn out to be quite stable even in an inhomogeneous setup, as present in ultracold bosons experiments, for a wide range of densities.

It is finally worth mentioning that other quantum-optics based setups, such as Feshbach molecules and Rydberg atoms, are suitable for investigation of many body phenomena linked to long range interactions: we refer the reader to specific reviews on the subject (Refs. [164] and [145, 165] respectively) for details.

Chapter 7

A new class of insulators: the Luttinger Staircase.

We study one dimensional fermionic and bosonic gases with repulsive power-law interactions $1/|x|^\beta$, with $\beta > 1$, in the framework of Tomonaga-Luttinger liquid (TLL) theory. We obtain an accurate analytical expression linking the TLL parameter to the microscopic Hamiltonian, for arbitrary β and strength of the interactions. In the presence of a small periodic potential, power-law interactions make the TLL unstable towards the formation of a cascade of lattice solids with fractional filling, a "Luttinger staircase". Several of these quantum phases and phase transitions are realized with groundstate polar molecules and weakly-bound magnetic Feshbach molecules.

7.1 Single wire with long-range interactions

There is presently considerable interest in quantum degenerate gases with long range interactions in reduced geometries [145]. This is motivated by recent experiments with polar molecules [154, 153, 151, 166, 167, 168, 169, 170], where electric dipole moments associated with rotational excitations lead to strong, anisotropic dipolar interactions [153], but also by experiments with atomic gases with strong magnetic dipoles [147]. For polar molecules, electric dipoles can be manipulated with external microwave AC and DC electric fields, which provides a toolbox to tailor the many-body interactions, and in combination with optical trapping in 1D or 2D promises the realization of stable exotic, strongly correlated quantum phases with long range interactions [159, 160, 171].

An intriguing example is given by polar molecules trapped in a 1D

wire [see Fig. 8.1(a)] [172, 173, 174, 175, 176], where long range interactions compete with an optical lattice in a commensurate - incommensurate transition. In the zero-tunneling limit in a deep lattice, this leads to the formation of a *devil's staircase*, that is, a continuous and non differentiable (Cantor) function for the ground state filling fraction as function of the chemical potential μ, studied first in the context of atomic monolayers adsorbed on solids [177, 178]. While recent studies at finite hopping have already shown a modification of this structure in a deep lattice [179, 158], the challenge is now to investigate the quantum regime where large kinetic energies compete with both interaction strengths and periodic confinement.

Below we show that using bosonization techniques [10, 11] the classification of quantum phases can be derived analytically for all power law interactions $C_\beta/|x|^\beta$ with $\beta > 1$ and for arbitrary relative strengths of the kinetic energy and the long-range repulsion. Remarkably, the parameters of the effective bosonized theory can be accurately obtained in analytical form for all β in terms of the microscopic Hamiltonian, even in the absence of integrability. This provides us with a universal phase diagram where the cases of repulsive Van der Waals ($\beta = 6$) and dipolar interactions ($\beta = 3$) should be accessible in polar molecule experiments [159, 160, 171]. In contrast to the classical devil's staircase, where lattice solids are stable over a finite interval in μ for every rational filling fraction between 0 and 1, and the total measure of such interval exhausts the full range of μ, we find that in the 1D quantum case large kinetic energies prevent the formation of ordered states, where the average interparticle distance is not constant. This drastically reduces the number of "steps" in the staircase to a number not dense in the interval $]0, 1]$, i.e. a *Luttinger staircase*. Signatures of these quantum phases are excitations in the form of solitons and breathers, detectable via Bragg scattering.

We assume that the polar molecules are polarized by external electric fields, and confined to a 1D geometry, e.g., by a sufficiently deep 2D optical lattice with frequency $\omega_\perp$. The shape of the long distance interactions can be tuned by coupling the lowest rotational manifolds of each molecule with DC and microwave AC fields. As shown in Refs. [159, 160, 171] we can tune between $\beta = 3$ with $C_3 = d^2/\epsilon_0$, where d is the dipole moment induced by an electric field $E_{\rm DC}$ and ϵ_0 the vacuum permittivity, and $\beta = 6$ with $C_6 \propto d^4/\hbar\Delta$, where Δ the detuning of a microwave field $E_{\rm AC}$ coupling the ground to the first excited rotational manifold. For average interparticle distances $a \gg (C_\beta/\hbar\omega_\perp)^{1/\beta}$ the gas dynamics is one-dimensional

7.1. Single wire with long-range interactions

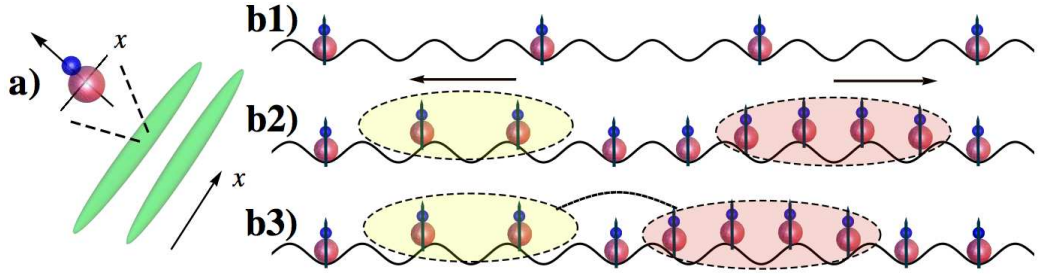

Figure 7.1: (a) Experimental setup (sketch): an array of 1D polar molecular gases is formed along x (green tubes); molecules are polarized perpendicular to x. (b1) Groundstate configuration in the solid phase with filling $1/p = 1/3$. (b2) soliton and antisoliton excitations with repulsive interactions with $1/p = 1$. (b2) a breather, $1/p = 1$ (text).

and microscopically described by the Hamiltonian

$$\begin{aligned} H &= \int dx\, \psi^\dagger(x) \left[-\frac{\hbar^2}{2m}\partial_x^2 + U(x) \right] \psi(x) \\ &+ \frac{1}{8\pi} \int dx\, dx' \psi^\dagger(x)\psi^\dagger(x') \frac{C_\beta}{|x-x'|^\beta} \psi(x')\psi(x). \end{aligned} \tag{7.1}$$

Here, $\psi(x)$ is a field operator for molecules, which can be either fermionic or bosonic, m is the particle mass, and $U(x) = U \sin^2(2\pi x/\lambda)$ is a weak periodic potential, as provided by a shallow optical lattice of strength $U_L \equiv U/E_R \lesssim 1$, with $E_R = h^2/2m\lambda^2$ and λ the lattice wavelength. For the case $\beta = 3$ with experimentally relevant molecules such as LiCs, RbCs or KRb molecules ($d_{\max} = 5.6$, 1.25 and 0.5 Debye, respectively) and confinement $\omega_\perp = 2\pi \times 100$ kHz, $(C_\beta/\hbar\omega_\perp)^{1/3}$ is of the order of 360, 130 and 80nm, respectively [159, 160, 171, 180, 181].

Homogeneous quantum fluid

In the absence of an optical lattice ($U_L = 0$) the short range character of power-law interactions with $\beta > 1$ allows a description of the low energy physics in terms of Tomonaga-Luttinger liquid (TLL) theory [11, 162]. Here, we first consider the bosonic case, and then discuss the differences with the fermionic one. The TLL effective Hamiltonian is given by [33, 174]

$$H = \hbar v \int dx \left[(\partial_x \theta(x))^2/K + K(\partial_x \phi(x))^2 \right] /(2\pi). \tag{7.2}$$

Here, the field $\psi(x)$ in Eq. (7.1) is replaced by $\psi(x) \sim \sqrt{n + \partial_x\theta(x)/\pi}\exp[i\phi(x)]$ in a hydrodynamic approach, and $\partial_x\theta(x)$ and $\partial_x\phi(x)$ characterize the long-wavelength fluctuations of the density n and of the phase $\phi(x)$, respectively, with $[\partial_x\theta(x), \phi(y)] = i\pi\delta(x-y)$. The liquid is completely characterized by the sound velocity v and Luttinger parameter $K = \hbar n\pi/(mv)$, which determines the algebraic decay of the correlation functions

$$\langle n(x)n(x')\rangle \sim |x-x'|^{-2K},\ \langle \psi(x)\psi^\dagger(x')\rangle \sim |x-x'|^{-1/2K}. \tag{7.3}$$

In general, K can be related to the microscopic parameters of the Hamiltonian only for exactly solvable models, e.g., contact interactions or $\beta = 2$ [Calogero-Sutherland (CS) model]. Below we show that the dependence of K on the microscopic parameters in (7.1) can be given *analytically* for arbitrary shape and strength of interactions,

$$K = \left[1 + \beta(\beta+1)\zeta(\beta)n^{\beta-2}R_\beta/(2\pi^2)\right]^{-1/2}, \tag{7.4}$$

with $n^{\beta-2}R_\beta$ the dimensionless interaction strength, and $R_\beta \equiv mC_\beta/(2\pi\hbar^2)$ (see Fig.7.3). In contrast to familiar bosonic gases with contact interactions where $K \geq 1$ [11, 182, 61], long-range power-law interactions constrain K to values $1 \geq K > 0$, where $K = 1$ corresponds to the Tonks-Girardeau gas limit and $K = 0$ to a system with long-range order [162]. Eq. (7.4) allows us to readily determine the *phase diagram* for $U_L = 0$, by comparing the relative decay of the correlation functions in (7.3): a crossover from superfluid (SF) to charge-density wave (CDW) behavior takes place at $K_c = 0.5$. The fermionic gas is also described by Eqs. (8.2) and (7.4), however its phase diagram displays a CDW behavior at all interaction strengths. In addition, correlation functions in (7.3) have a slightly different long-distance decay [10, 11]. In the following, statistics will not be relevant, and thus we deal with both cases at the same time.

7.1.1 The Luttinger staircase

A cascade of insulating lattice solids can be realized from a TLL with power-law interactions, by introducing a vanishingly-small periodic lattice potential, as provided by the shallow optical lattice $U(x)$ in Eq. (7.1). Combining the complete density operator with the periodic term $U(x)$ [61], one obtains

$$\sum_r U_r \equiv \sum_r \left\{ \frac{\mathcal{U}}{\pi\Lambda^2} \int \cos[r2\theta(x) + Q_r(n,\lambda)x]dx \right\}, \tag{7.5}$$

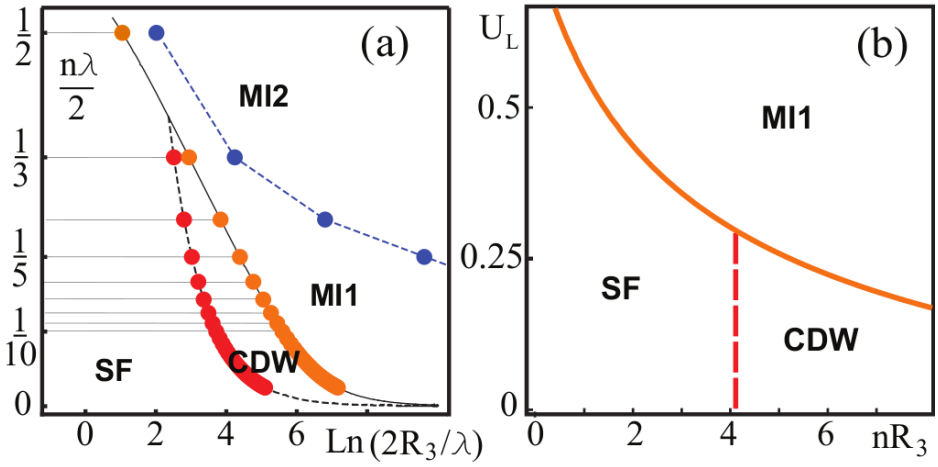

Figure 7.2: (a) Commensurate phase diagram for bosons with dipolar interactions $\beta = 3$, and lattice depth $U_L = 0.1$. Physical configurations correspond to commensurate fillings $n\lambda/2 \equiv 1/p$, with $p \in \mathbb{N}$ (horizontal lines are guides to the eye for $p \leq 10$). Quantum phase transitions from a TLL to a lattice solid [or Mott insulator, (MI)] occur for each $1/p$ at the position of the dots on the continuous line, while red and blue dots on dashed lines indicate crossovers. MI1 and MI2 indicate MI with solitonic and breather excitations, respectively (see Fig.1). (b) Phase diagram at commensurate filling $1/p = 1/3$ in the U_L vs nR_3 plane. Continuous line: quantum phase transition between a TLL and a lattice solid. The phase diagram for fermions is identical to the one for bosons, except the TLL is always a CDW.

with $Q_r(n,\lambda) \equiv 2\pi\,(rn - 2/\lambda)$ and $r \in \mathbb{N}$. Here, $\mathcal{U} \equiv \pi n U \Lambda^2/2$, where Λ is a cutoff that fixes the energy scale of the initial Hamiltonian [10, 11]. The term Q_r in Eq. (7.5) is responsible for a possible competition between two lengths scales: the interparticle distance $1/n$ and the lattice period $\lambda/2$. We can then distinguish two different situations: a *commensurate* one with $Q_r = 0$, where the length-scales do not compete, corresponding to the condition $2/(\lambda n) = p \in \mathbb{N}$, and an *incommensurate* one with $Q_r \neq 0$, where a competition is present.

In all commensurate cases $2/(\lambda n) = p \in \mathbb{N}$, the most relevant term due to the optical lattice in (7.5) in the renormalization-group sense is U_p. Keeping only this term, the system becomes equivalent to a sine-Gordon model [10, 11], where the scaling dimension of the cosine operator is affected by the interparticle interactions through K and by the optical lattice through $\mathcal{U}$. For $p > 1$ we then expect that for weak interactions and small

depth of the optical lattice the cosine term in (7.5) is irrelevant and the TLL liquid is preserved, with correlation functions decaying polynomially as in (7.3). However, when the cosine term is relevant, we have a non-zero expectation value $\langle \cos[p\sqrt{4\pi}\phi(x)]\rangle \neq 0$ and the system is *pinned* on the lattice. This pinning corresponds to the breakdown of TLL and to the formation of a lattice solid, or Mott insulator (MI), with particles localized at individual sites of the lattice, every p lattice sites. In this phase, the excitation spectrum is gapped and the off-diagonal correlation function decays exponentially. Using Berezinskii-Kosterlitz-Thouless (BKT) scaling near criticality [10, 11], we find that for each p the gapped phase occurs for

$$2 + U_L > Kp^2, \tag{7.6}$$

with $U_L \equiv U/E_R \lesssim 1$. Eq. (7.6) is remarkable in that it shows that power-law interactions make possible the realization of an infinite series of gapped phases at lattice filling less than one [Fig. 8.1(b1) for $p = 3$]. The case $p = 1$ is peculiar as Eq. (7.6) is always satisfied, implying a lattice solid for a vanishingly small U_L. The cascade of solids with $p \in \mathbb{N}$ corresponds to a quantum version of a Devil's staircase structure, where large kinetic energies of order of E_R prevent the formation of ordered states where the average interparticle distance is not constant. This is in contrast to the *classical* Devil's staircase of the Frenkel-Kontorova model [177, 178], where commensurability is also allowed for rational fillings $r \in \mathbb{Q} \neq \mathbb{N}$. Evidence of this classical case have been recently found in the deep lattice limit of Refs. [179, 158] for $\beta = 3$, in 1D and 2D.

Equation (7.6) shows that a gap is favored by high densities, strong interactions and finite (small) lattice depths. For $U_L < 1$ a good estimate for the gap Δ is given by [78]

$$\Delta = \frac{8}{\sqrt{\pi}} \frac{\Gamma[\frac{\pi K}{(4-2K)}]}{\Gamma[\frac{2+K(\pi-1)}{4-2K}]} \left(K^2 \frac{U_L}{16} \frac{\Gamma[1-\frac{K}{2}]}{\Gamma[1+\frac{K}{2}]} \right)^{\frac{1}{2-K}} . \tag{7.7}$$

When K is close to $1/p^2$, Δ approaches the *massive fermion* limit $\Delta \sim U/2$ recently observed for $p = 1$ with contact interactions [61] (see Chapter 2 for details), whereas close to the BKT transition it closes exponentially. In the vicinity of the BKT transition excitations are of the soliton/antisoliton type, which in the massive fermion limit correspond to weakly repulsive particles and holes, Fig. 8.1(b2). In contrast to contact interactions, power-law interactions allow one to tune the *sign* of the soliton-antisoliton interactions from repulsive ($K > 1/p^2$) to *attractive* ($K < 1/p^2$), giving rise to soliton-antisoliton bound states called *breathers* [Fig. 8.1(b3)]. These excitations are confined in space but oscillatory in time, and are stable solutions

	KRb	RbCs	LiCs	$^{52}Cr_2$	$^{164}Dy_2$	$^{166}Er_2$
$U_L(1)$	0_+	0_+	0_+	0_+	0_+	0_+
$U_L(1/2)$	0.8	0_+	0_+	1.9	1.5	1.7
$U_L(1/3)$	-	1.4	0_+	-	-	-

Table 7.1: Minimal lattice depth $U_L(1/p)$ for a lattice solid at filling $1/p$, for groundstate polar molecules (KRb, RbCs, LiCs) and magnetic Feshbach molecules ($^{52}Cr_2$,$^{164}Dy_2$,$^{166}Er_2$); an arbitrarily small periodic potential pins the TLL for 0_+. Lattice depths with $U_L(1/p) \gtrsim 2$, where the sine-Gordon picture breaks down (see Chapter 2), are not considered.

of the equations of motion for the sine-Gordon model [10, 11]. The number of breather excitations is $\mathcal{N} = 2(1/K - 1)$, with energy

$$M_b(n') = 2\Delta \sin[\pi n'/(4/K - 2)], \quad n' \leq \mathcal{N}. \tag{7.8}$$

For $K < 1/(2p^2)$ breathers are the lowest-energy excitations, qualitatively changing the spectrum of the insulating phase with respect to the familiar case of contact interactions. Strong power-law interactions will allow for an unambiguous observation of this localized topological excitations, with applications ranging from Josephson junctions to conjugated polymers, see below [183, 184]. In the vicinity of commensurate fillings ($p \in \mathbb{N}$), the system exhibits a gap as long as the energy shift due to $Q_r \neq 0$ remains small with respect to $K\Delta/2$, the energy required to add a particle: this ensures stability of the phases above with respect to small density changes. Above a critical Q_c a commensurate-incommensurate phase transition takes place from an insulator to a gapless phase, similar to contact interactions [185, 61]. For generic values of $Q_r \neq 0$, the TLL is stable.

Figure 7.2(a) shows the *commensurate phase diagram* for the case of bosonic particles with dipole-dipole interactions $\beta = 3$ as a function of the lattice filling $1/p = n\lambda/2$ and the strength of interactions R_3. The lattice depth is $U_L = 0.1$. For each $p \in \mathbb{N}$, the BKT quantum phase transition occurs at the position of the dot along the continuous line, while dots on the dashed lines characterize crossovers. The regions denoted as MI1 and MI2 correspond to MI with soliton/antisoliton and breather excitations, respectively, and the dashed line signals the crossover for $K = 1/(2p^2)$. Panel (b) shows the transition between the TLL and solid behavior as a function of the lattice depth and nR_3 for the case of $p = 3$. The phase diagram for fermionic particles is identical to Fig. 7.2, except that the TLL phase is always a CDW. Phase diagrams for $\beta \neq 3$ look qualitatively similar to Fig. 7.2.

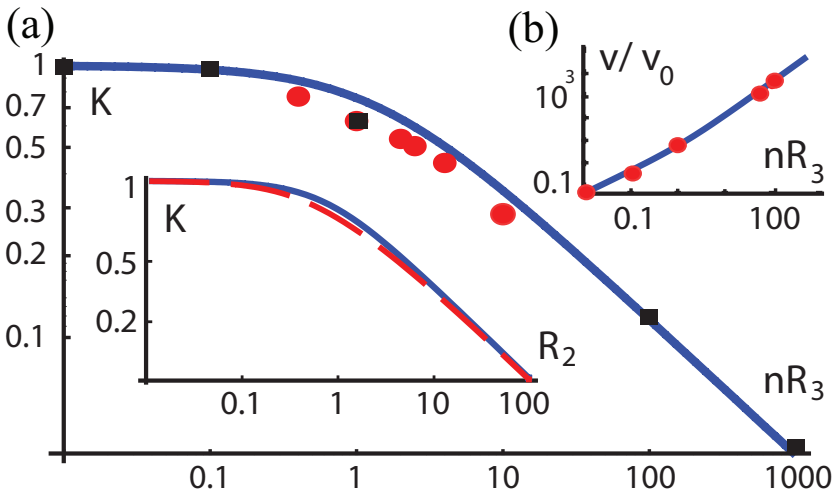

Figure 7.3: (a) TLL parameter K vs the dimensionless interaction strength $n^{\beta-2}R_\beta$ for dipolar interactions $\beta = 3$. Line: analytic result Eq. (7.4). Squares and dots: quantum Monte-Carlo (QMC) results of Refs. [174] and [176], respectively. Inset: K vs $n^{\beta-2}R_\beta$ with $\beta = 2$. Continuous line: Eq. (7.4). Dashed line: exact Calogero-Sutherland model. (b) TLL velocity v vs nR_3 for $\beta = 3$, with $v_0 \equiv \hbar/(\sqrt{2}mR_3)$. Line and dots: analytic and QMC results of Ref. [175], respectively.

In Table 7.1 we list the estimated minimal lattice depth necessary to realize a MI with filling $1/p$, for a few groundstate polar molecules. In addition, we report estimates for magnetic Feshbach molecules, where the magnetic dipole moment is taken as twice the atomic one [186]. The realization of insulating states with, e.g., $p = 2$ will help stabilize highly-excited Feshbach molecules against three-body recombination, opening the way to the realization of strongly-correlated lattice phases.

7.1.2 Analytical expression for K

For $U_L = 0$, Eq. (7.1) describes an effective, strictly one-dimensional, *scale invariant* theory, dependent only on $n^{\beta-2}R_\beta$ at all length/energy scales. After rescaling, dimensionless interactions read $V(y \equiv rn) = R_\beta n^{\beta-2}/y^\beta$, and ultraviolet divergences in Eq. (7.1) can be treated by introducing a dimensionless cut-off A [10, 11]. We choose A such that $V(y) \propto (y + A)^{-\beta}$, so that scale-invariance is preserved explicitly: the *shape* of the regularized potential is independent of C_β and n. We can now fix A self-consistently in the effective 1D theory, as follows [consistency with the microscopic derivation of (7.1) implies $A/n \gtrsim (C_\beta/\hbar\omega_\perp)^{1/\beta}$]. We com-

pute K analytically in the strong- ($n^{\beta-2}R_\beta \gg 1$) and in the weak-coupling ($n^{\beta-2}R_\beta \ll 1$) limits as $K_{\rm s} = \pi/[\beta(\beta+1)\zeta(\beta)R_\beta n^{\beta-2}/2]^{1/2}$ [175] and $K_{\rm w} = (1+n^{\beta-2}R_\beta\tilde{V}(0)/2\pi)^{-1/2}$ [10, 11], respectively, with $\tilde{V}(0) = A^{1-\beta}/(\beta-1)$ the Fourier transform of $V(y)$ at zero-momentum, and ζ the Riemann Zeta-function. Due to the similar functional dependence, we then fix $A = [\beta(\beta-1)(\beta+1)\zeta(\beta)/\pi]^{1/(1-\beta)}$ by matching $K_{\rm w} = K_{\rm s}$ for $n^{\beta-2}R_\beta \gg 1$ and obtain the approximate Eq. (7.4) [1].

Expression (7.4) compares favorably with known exact results. In Fig. 7.3(a) (Inset) we compare it to the exact expression $K_{CS} = 2/(1+\sqrt{1+2R_2})$ for $\beta = 2$, which we derive from the Bethe-Ansatz solution of the CS-model [187, 188]. We find *quantitative* agreement between the two curves for the entire range of interaction strengths $0 < R_2 \leq 100$, with a maximal relative difference of about 5% at $R_2 \simeq 1$, and recover the n-independence of the CS model [187, 188, 189]. Furthermore, in the main figure we compare $K = 1/\sqrt{1+0.73nR_3}$, as derived from Eq. (7.4) for $\beta = 3$, to the numerical quantum Monte-Carlo results of Refs. [174] and [176] (black squares and red dots, respectively), finding good agreement for $0 < nR_3 \leq 1000$. In panel (b), we also plot the velocity v in the same range of nR_3 values, finding excellent agreement with the results of [174]. This fixes the phenomenological parameters in the effective Hamiltonian (8.2). We are not aware of exact results for $\beta > 3$ to compare with our predictions.

The extension of the techniques described here to several species will enable a microscopic treatment of strongly correlated phenomena in mixtures of polar molecules in single- and multi-tube configurations, as relevant to experiments [153], in particular exotic phases such as bond-ordered density waves and trimer liquids.

[1] This fails for the Coulomb case [162] [$\zeta(\beta)$ not defined], with the cut-off usually fixed by the microscopic theory.

Chapter 7. A new class of insulators: the Luttinger Staircase.

Chapter 8

Two-leg dipolar ladder: quasi-1D crystals and exotic bound states.

We investigate the pairing and crystalline instabilities of bosonic and fermionic polar molecules confined to a ladder geometry[190, 191]. By means of analytical and quasi-exact numerical techniques, we show that gases of composite molecular dimers as well as trimers can be stabilized as a function of the density difference between the wires. A shallow optical lattice can pin both liquids, realizing crystals of composite bosons or fermions. We show that these exotic quantum phases should be realizable under current experimental conditions in finite-size confining potentials.

8.1 Introduction

The confinement of groundstate polar molecules to low-dimensional geometries combined with their polarization using external fields opens the possibility of studying novel inter-molecular pairing mechanisms associated with dipole-dipole interactions in a setup where collisional losses are suppressed[153]. This has lead to the prediction of several novel quantum phases in coupled two-dimensional (2D) layers as well as one-dimensional (1D) wires, such as spontaneous 2D inter-layer superfluidity, analogous to bi-exciton condensation, and molecular 1D polymers. One question is whether these pairing mechanisms, which in their basic form rely on the pairing of two dipoles separated by a confining potential, can be generalized to complex multi-molecular structures and whether these few-molecule structures can be stabilized in finite-density many-body phases.

In this Chapter we focus on the physics of polar molecules confined

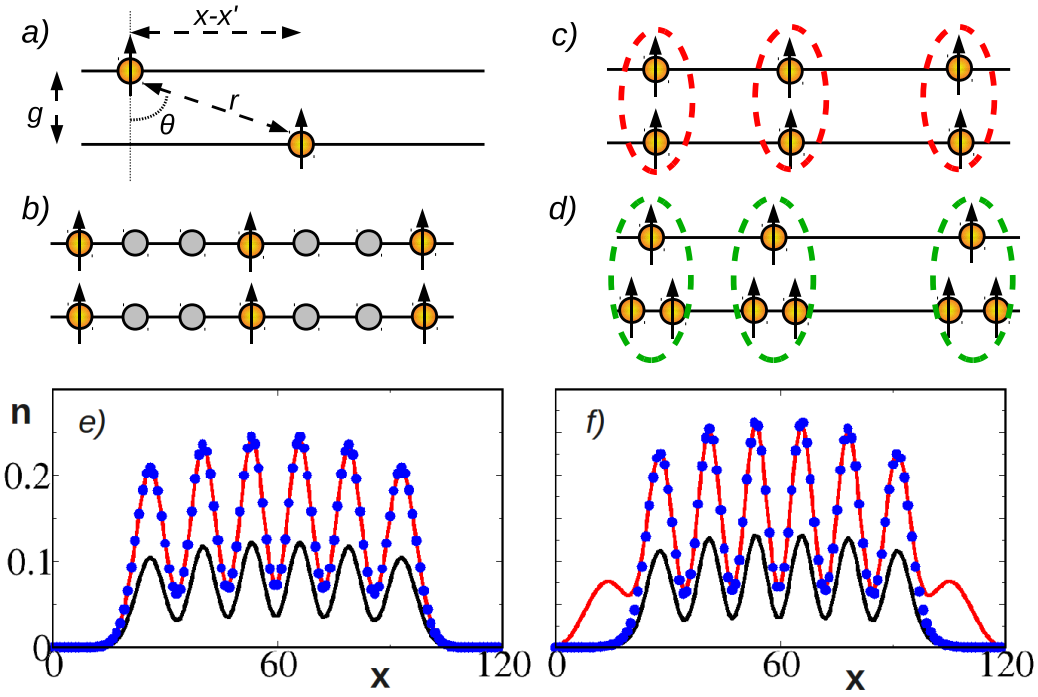

Figure 8.1: Panel *a*: typical configuration of a two-leg ladder. Panels *b-d*: cartoons of phases discussed in the text: DC(*b*), DL(*c*) and TL(*d*)(see text). (e-f) Density distributions n_1(black, darker) and n_2(red) of a trapped gas with $\mathcal{K} = 0.03, t_2 = 0.01, d_1 = 3 = 6d_2, g = \lambda/2$. *e*: $n_2 = 2n_1 = 12$, *f*: $n_2 = 2n_1 + 2 = 14$ respectively; as a reference, blue points denote $2n_1$. $L = 60$ denote the trap center.

to two coupled 1D wires, under realistic conditions where the number of molecules can very across the tubes. This situation leads to a rich phase diagram, which we describe entirely. We find that: (i) when tubes are identical, a two-body bound state is always present and responsible for realizing dimer liquids, similar to 2D [192, 193]. However, in general, *few-body* pairing across the tubes is favored for *any* rational ratio of populations between the tubes $P = p/q$, with $p, q \in \mathbb{N}$, which is a set dense between $]0, 1]$. In particular, we prove that a gas of trimers, composite bosons or fermions involving two particles on one tube and one in the other, can be realized in state of art experiments with cold polar molecules. Crucially, repulsive intra-tube interactions as well as negligible inter-tube tunneling ensure collisional stability. These dimer and trimer liquids can then be pinned by a weak period potential, which can stabilize a quasi-1D

composite crystal with long-range diagonal order (TLRO). In general one would expect that these exotic bound-states and the ensuing few-body liquids to be unstable under realistic conditions where particles are confined by finite-size harmonic potentials. Surprisingly, we find that in the presence of confining potentials the gases realize stable wedding-cake structures of few-body composite molecules with different numbers of particles per macro-molecule. These structures are found to be robust against small fluctuations in the populations in the various tubes.

8.2 Model Hamiltonian

Our starting point is the Hamiltonian $H = \sum_\alpha H_\alpha + H_{12}$ describing the dynamics of molecules in the configuration of Fig. 8.1, with $\alpha = 1, 2$ and H_α the single-wire term

$$\begin{aligned} H_\alpha &= \int dx\, \psi_\alpha^\dagger(x) \left[-\frac{\hbar^2}{2m_\alpha}\partial_x^2 + U_\alpha(x) \right] \psi_\alpha(x) \\ &+ \frac{d_\alpha^2}{8\pi} \int dx\, dx' \frac{1}{|x-x'|^3} n_\alpha(x) n_\alpha(x'), \end{aligned} \tag{8.1}$$

and $H_{12} = (d_1 d_2)/(8\pi) \int dx\, dx' V(x-x') n_1(x) n_2(x')$ the inter-wire coupling, with $V(x-x') = [1 - 3\cos^2(\theta)]/[g^2 + (x-x')^2]^{3/2}$ showing a short-distance inter-wire attraction. Here, m_α, d_α are the mass and the dipole strength respectively, and ψ_α ($\psi_\alpha^\dagger$) are fermionic or bosonic annihilation (creation) operators, with $n_\alpha(x) = \psi_\alpha^\dagger(x)\psi_\alpha(x)$; $U_\alpha(x) = \mathcal{U}_\alpha \sin^2(2\pi x/\lambda)$ represents an underlying periodic potential, as usually provided by an optical lattice [44] with wavelength λ and depth $\mathcal{U}_\alpha$; θ is the angle between particles in different wires, with distance g, Fig. 8.1.

In the previous Chapter, it is shown that in the absence of an optical lattice ($U_\alpha = 0$) and of inter-wire interactions, the dynamics in each wire is described by an effective Tomonaga-Luttinger liquid (TLL) theory [33] with Hamiltonian [11, 10]

$$\mathcal{H}_\alpha = \frac{\hbar v_\alpha}{2\pi} \int dx \left[(\partial_x \vartheta_\alpha(x))^2 / K_\alpha + K_\alpha (\partial_x \phi_\alpha(x))^2 \right].$$

Here v_α and $K_\alpha = (1 + 0.73 n_\alpha R_\alpha)^{-1/2}$ are the effective sound velocity and the TLL parameter, respectively**[?]**, with $R_\alpha = m_\alpha d_\alpha^2/(2\pi\hbar^2)$ the intra-wire dipole length, and $\vartheta_\alpha, \phi_\alpha$ represent long-wavelength density and phase fluctuations[11, 10]. For finite interactions, Eq. (8.2) is then effectively described by $\mathcal{H} = \sum_\alpha \mathcal{H}_\alpha + \mathcal{H}_{12}$, with $\mathcal{H}_{12} = \mathcal{H}_f + \mathcal{H}_b$. Here, in the weak

coupling regime and approximating the interwire interaction with its zero-component Fourier transform[11, 10],

$$\mathcal{H}_f = -\frac{d_1 d_2}{24 g^2 \pi^3} \int dx \partial_x \vartheta_1(x) \partial_x \vartheta_2(x) \tag{8.2}$$

is the *quadratic* forward-scattering part of the interactions [11, 10], and $\mathcal{H}_b$ is the *back scattering* part, with a typical sine-Gordon-type (sG) form, to be discussed below. As customary, the effect of $\mathcal{H}_f$ is to modify the effective parameters in the two coupled TLLs, while $\mathcal{H}_b$ can induce novel pairing instabilities. Here, we first discuss the case of two identical (*balanced*) coupled wires, and then the more general case of (*unbalanced*) wires with different densities, molecular masses and interactions.

8.2.1 Balanced case

In the balanced case, the quadratic part $\sum_\alpha \mathcal{H}_\alpha + \mathcal{H}_f$ of $\mathcal{H}$ can be diagonalized by introducing standard charge and spin fields, $\vartheta_{c,s} = (\vartheta_1 \pm \vartheta_2)/\sqrt{2}$, leading to a description in terms of coupled TLLs with effective parameters $K_{c,s}$. For weak interactions we estimate

$$K_{c,s} = K_1 \left[1 \mp \Gamma_{12} K_1 / v_1\right]^{-1/2}, \tag{8.3}$$

with $\Gamma_{12} = d_1^2/(24\pi^2 \hbar g^2)$. The term $\mathcal{H}_b$ has the sG form

$$\mathcal{H}_b \propto -\frac{n_1^2 d_1 d_2}{12 g^2 \pi} \int dx \cos[2\sqrt{2}\vartheta_s(x)], \tag{8.4}$$

and, in agreement to Berezinskii-Kosterlitz-Thouless (BKT) theory [10], it is relevant, thus opening a spin gap, if $K_s < 1$; this condition is always satisfied in Eq. (8.3), showing that, similar to the 2D case, pairing of molecules across the wires is always favored in 1D, even for an infinitesimally small attraction between the wires with $g, R_\alpha \ll n_\alpha^{-1}$. The role of dipolar interactions is evident in the charge sector: in contrast to models with attractive contact interactions such as the Hubbard model[11, 10], here K_c can be much smaller than 1; as an example, in the strongly interacting regime $n_\alpha R_\alpha \gg 1$, where dimers are well approximated by tightly-bound composite particles with effective mass $M = 2m$ and dipole strength $D = 2d$, $K_c \simeq 2/(1 + 0.37 n_\alpha R_\alpha)^{1/2}$. As a result, the many-body groundstate shows a crossover from a dimer liquid (DL) with dominant pair correlations $\mathcal{D}(x) = \langle \psi_{1,i}^\dagger \psi_{2,i}^\dagger \psi_{1,i+x} \psi_{2,i+x} \rangle \sim |x|^{-1/K_c}$ for $K_c > 1$ to a charge-density wave (CDW) with dominant density correlations $\mathcal{G}(x) = \langle n_i n_{i+x} \rangle \sim |x|^{-K_c}$

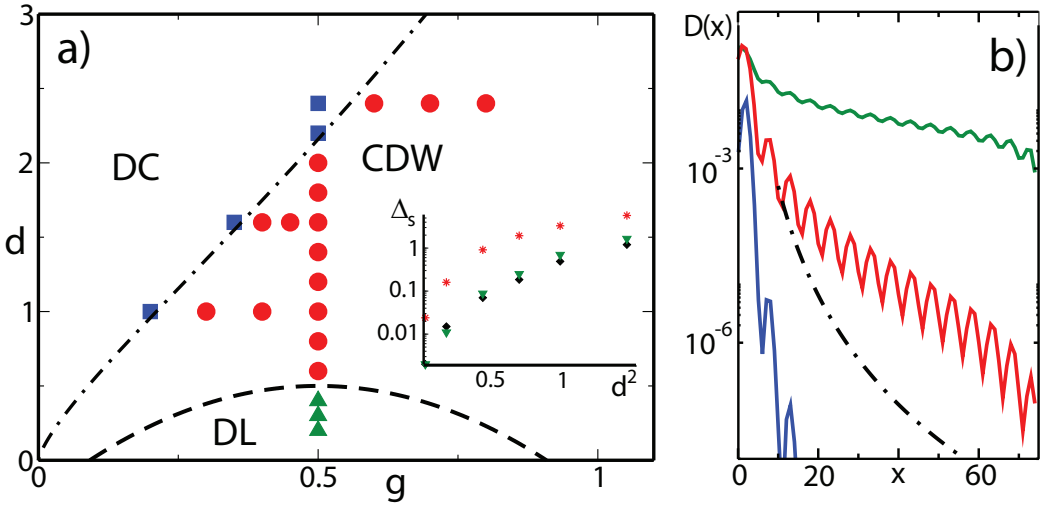

Figure 8.2: Panel *a*: phase diagram in the balanced case with $n_1 = n_2 = 1/5$ in the deep lattice regime, $g = \lambda/4$. Green triangles, red circles and blue squares denote DL, CDW and DC phases respectively; dashed and dot-dashed lines are qualitative phase boundaries. Inset: scaling of Δ_s as a function of d for different populations and interwire distances: $n = 1/5, g = 0.35\lambda$ (red squares), $n = 2/5, g = \lambda/2$ (green triangles) and $n = 1/5, g = \lambda/2$ (black circles). Panel *b*: suppression of $\mathcal{D}(x)$ with increasing interaction. Here $g = \lambda/4, n_1 = n_2 = 1/5$ and $d = 0.5$ (DL), 1.3 (CDW) and 2.2 (DC) from top to bottom, thick lines; the dot-dashed line is an algebraic references, $1/x^{25/4}$.

for $K_c < 1, n_i = n_{i,1} + n_{i,2}$. In this regime the addition of a shallow lattice potential commensurate with the dimer density immediately pins the CDW, inducing a quantum phase transition to an insulating phase. Here the lattice has the sG form[11, 10] (see the previous Chapter):

$$\mathcal{H}^{bc}_{OL} \propto \frac{n_1^2 d_1 d_2}{g^2} \int dx \cos[2f\sqrt{2}\vartheta_c(x)], \tag{8.5}$$

with $f \in \mathbb{N}$. BKT-scaling then shows that an insulating dimer crystal (DC) is stabilized whenever the commensurability condition $n\lambda/2 = 1/f$ is satisfied and $K < K_c = 4/f^2$, forming a Luttinger staircase as illustrated in Chapter 7; each DC is characterized by a periodic structure with one dimer every f sites and is gapped.

We verify numerically these predictions in the deep lattice regime $\mathcal{U}/E_r \gg 1$, with E_r the lattice recoil, where an appropriate description is given in

terms of an anisotropic extended Hubbard model (AEHM) [145]:

$$\begin{aligned}\hat{H} &= -\sum_{\alpha,i} t_\alpha (c^\dagger_{\alpha,i} c_{\alpha,i+1} + h.c.) - \frac{2d_1 d_2}{g^3} \sum_i n_{1,i} n_{2,i} + \\ &+ \sum_{i<j} \left[d_1 d_2 V_{ij} (n_{1,i} n_{2,j} + n_{2,i} n_{1,j}) + \sum_\alpha \frac{d_\alpha^2 n_{\alpha,i} n_{\alpha,j}}{(j-i)^3} \right].\end{aligned}$$

Here V_{ij} describes the anisotropic part of the dipolar interaction, $t_\alpha = 1$ sets the energy scale. In the balanced case, $d_\alpha = d$ and $n_\alpha = n$. The field theoretical description of Eq. (8.6) in terms of continuum fields is equivalent to the one in the limit of a shallow lattice given above, and we thus expect a similar qualitative behavior. Figure 8.2 shows the phase diagram for a commensurate density $n_\alpha = 1/5$, where the numerical data are obtained using a quasi-exact Density-Matrix-Renormalization-Group technique [28, 29]. By fixing $g = \lambda/4$ and increasing d, we find first a crossover from a TLL of dimers (DL) to a DCDW, and then a BKT-type pinning quantum phase transition to a DC with $n_\alpha = 1/5$ (phase boundaries are discussed in [194]). Examples of $\mathcal{D}(x)$ are plotted in panel (b) for all three phases, where the dash-dotted line marks the transition from power-law to exponential decay. We also calculate the spin gap Δ_s, by performing a finite-size scaling of $\Delta_s(L) = E_L(N,N) - E_L(N+1,N-1)$, with $E_L(M,M')$ the ground state energy at finite size L in the sector with $n_1 = M, n_2 = M'$, for different densities and g [Inset of panel (a)]. We find that a finite gap is present in the entire phase diagram, as expected, although it is small for weak interactions due to the BKT scaling $\Delta_s \propto \exp[-\beta d^2]$[10].

8.2.2 Unbalanced case

The unbalanced case presents unconventional instabilities. As shown in [123, 195], the Haldane expansion of density operators [33] in a two-component TLL generates a infinite series of massive terms coming from different combinations of vertex operators

$$\mathcal{H}_b = \sum_{p,q\in\mathbb{N}} G_{p,q} \int dx \cos[2x(pk_{F1} - qk_{F2}) + 2(p\theta_1 - q\theta_2)],$$

where $G_{p,q}$ are model dependent coefficients and $k_{F\alpha} = \pi n_\alpha$. With the exception of the simplest case $p = q = 1$, these terms are usually neglected for two reasons: *i)* if the oscillatory factor $\mathcal{F}_{p,q} = pk_{F1} - qk_{F2}$ is non-zero, they cannot contribute to the long-wavelength theory due to strong fluctuations, whereas *ii)* when $\mathcal{F}_{p,q} = 0$ for $p + q > 2$ they are irrelevant from the

renormalization group point of view due to their large scaling dimension. However, we find that strong dipolar interactions drastically enhance the effect of $\mathcal{H}$[194], allowing the formation of *multiparticle composites* [123], or *multimers*, made of one particle on the upper wire and κ particles on the lower one. Analogous to the above discussion of dimers, the system may behave as a *multimer liquid*, uniquely identified by the finite gap associated with the bound state formation and an algebraic decay of multimer correlations

$$\langle \mathcal{M}^\dagger(0)\mathcal{M}(x)\rangle, \quad \mathcal{M} = (\psi_1)^\kappa \psi_2, \tag{8.6}$$

while the single-particle and dimer correlations $\mathcal{D}(x)$ decay exponentially. To prove this, let us consider, e.g., a population $n_2 = \kappa * n_1, \kappa \in \mathbb{N}$ in the lower wire. In that case, the condition $\mathcal{F}_{\kappa,1} = 0$ is satisfied, and the more relevant term in $\mathcal{H}_b$ has the sG form

$$G_{\kappa,1} \int dx \cos[2(\kappa\vartheta_1 - \vartheta_2)]. \tag{8.7}$$

Neglecting effective spin-charge interaction and collapse instabilities, we expect a BKT transition from two TLLs to a multimer liquid when the effective spin parameter $K_M = (1 + \kappa K_1 K_2 g/(\kappa^2 K_1 + K_2))^{-1}$, defined with respect to the multimer field $\vartheta_M = (\kappa\vartheta_1 - \vartheta_2)/\sqrt{2}$ is smaller than 1, which suggests that very large interaction strengths are needed to stabilize multimers with $\kappa > 2$. In the following, we thus investigate in detail the possibility to stabilize a trimer liquid (TL), with $n_2 = 2n_1$. We consider the lattice case of Eq. (8.6) with both interaction and hopping asymmetry, quantified by the ratios d_2/d_1 and t_2/t_1.

A first hint on possible TL instabilities is provided by the binding energy of the three body problem, $\Delta_B = \lim_{L\to\infty}[E_L(1,1)+E_L(0,1)-E_L(1,2)]$. Numerical results for three archetype cases are plotted in the inset of Fig. 8.3*a*, showing that $\Delta_B > 0$ up to a certain value of t_2 which depends on both d_1 and d_2. We have then investigated the $t_2 \lesssim 0.3$ region for different values of $d_1,\ d_2$ and density $n_2 = 1/5, 1/10$ on systems up to $L = 120$ with DMRG. The TL phase is characterized by an exponential decay of both $\mathcal{D}(x)$ and single particle correlation function $\mathcal{C}_\alpha(x) = \langle c^\dagger_{\alpha,i} c_{\alpha,i+x}\rangle$, whereas the trimer correlator

$$\mathcal{T}(x) = \langle c^\dagger_{1,i} c^\dagger_{2,i} c^\dagger_{2,i+1} c_{2,i+x+1} c_{2,i+x} c_{1,i+x}\rangle \tag{8.8}$$

decays algebraically, while when no correlation is exponentially suppressed the systems behaves like a two-fold TLL(see Fig.8.3*b-c*). In addition, strong asymmetry can lead to phase separation (PS) between high- and low-density regions. The phase diagram for $d_1 = 6d_2, n_2 = 1/10$ is plotted in Fig.8.3*b*(see

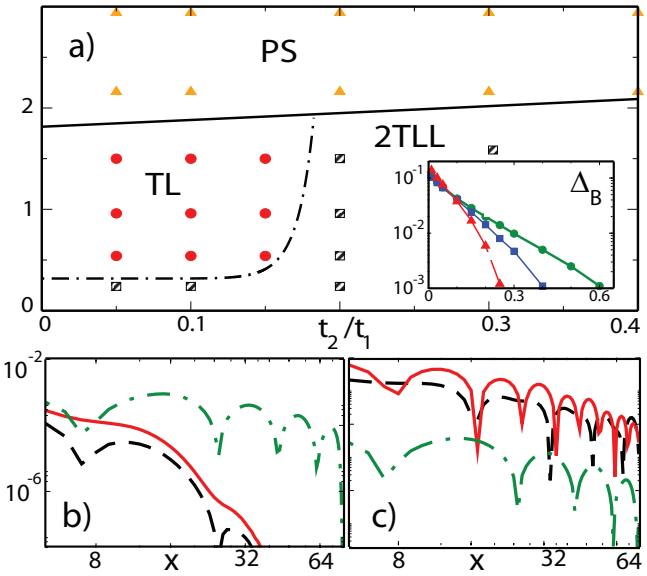

Figure 8.3: Panel *a*: unbalanced numerical phase diagram for $n_2 = 2n_1 = 1/10$ at $d_1 = 6d_2, g = \lambda/2$: red points, yellow triangles and black squares denote points in the TL, 2TLL and PS region; lines are guide for the eye. Inset: trimer binding energy Δ_B for different Hamiltonian parameter $(d_1/t_1, d_2/t_1)$ in linear-log scale as a function of t_2/t_1: red triangles (0.5, 3), blue squares (0.3, 1.8) and green circles (0.5,2). Panels *b-c*: correlation functions $\mathcal{T}(x)$(green squares), $\mathcal{C}_1(x)$(red triangles) and $\mathcal{D}(x)$(black circles) in a $L = 120$ sites system: TL(*b*; $d_1 = 3 = 6d_2, t_2 = 0.1$) and TLL phase(*c*; $d_1 = 2.4 = 6d_2, t_2 = 0.4$).

also [194]): the TL extends in a broad region, and survives even with relatively small interaction strength and interaction asymmetry; however, in both cases small hopping rates $t_2 \leq 0.2$ are needed. In the strongly interacting regime, phase separation occurs.

8.2.3 Effect of the trap

. The fate of these exotic bound states in a trapped system is, however, not guaranteed. First of all, one needs to identify a proper local order parameter which can give evidence of a paired states. In the TL case, we found that the quantity $\delta n_i = 2n_{1,i} - n_{2,i}$, which describes the matching between the density of the majority component with respect to double the minority one, provides a useful tool to distinguish between different phases in the

inhomogenous system[194]. We have then performed DMRG calculations introducing a trapping potential of the form $\hat{H}_{trap} = (\mathcal{K}/L^2)\sum_i n_i(L/2-i)^2$ for different values of $\mathcal{K}$ and $t_2 = 0.01, d_1 = 3 = 6d_2$, checking what are the required trap strength needed to stabilize a TL. The numerical results show how a shallow trap strength of order $\mathcal{K} \lesssim 0.3$ allows trimer to appear in the middle of the system: remarkably, the TL is stable even for not exactly matched densities $2n_1 \neq n_2$, as can be inferred in Fig. 8.1 *e-f* (see also [194]). In addition, the large effective mass of the trimers push them towards the middle region, while dimers and single particles usually appear in the wings (Fig 8.1 *f* and [194]).

Chapter 8. Two-leg dipolar ladder: quasi-1D crystals and exotic bound states.

Chapter 9

Magnetic phases with long-range interactions: hidden order via three-body losses

We study the emergence of several magnetic phases in dipolar bosonic gases subject to three-body loss mechanism employing numerical simulations based on the density matrix renormalization group(DMRG) algorithm. After mapping the original Hamiltonian in spin language, we find a strong parallelism between the bosonic theory and the spin-1 Heisenberg model with single ion anisotropy and long-range interactions. A rich phase diagram, including ferromagnetic, antiferromagnetic and non-local ordered phases, emerges in the one-dimensional case, and is preserved even in presence of a trapping potential.

9.1 Introduction

Recent experimental advances in controlling ultracold gases of magnetic atoms[146, 147] and polar molecules[154, 151, 153] have paved the way to the investigation of several quantum many-body phenomena[145, 156]. These setups naturally provide anisotropic, long-range dipolar interactions, which can be tuned and manipulated with high accuracy in order to access the physics of spin systems[196] and Hubbard-like models[145, 156] loaded into optical lattices[44]. Considerable theoretical efforts have focused on one dimensional geometry, where non-local interactions play a fundamental role in stabilizing interesting phenomena such as supersolidity[197], checkboard insulator[179] (see also Chapter 7) and insulating phases characterized by non-local order parameters[126, 198].

Furthermore, dissipative processes have emerged as an additional, relevant source of interaction. Two-body losses have been successfully employed to engineer hard core interactions in molecular gases[92], thus leading to the stabilization of a Tonks-Giradeau gas, and three-body losses have been proposed as a dynamical source of three-body interaction[93] which stabilizes dimer-superfluidity[93, 199, 200], color-superfluidity (as investigated in Chapter 5)and Pfaffian-like states[133, 201] with ultracold atoms.

The aim of this Chapter is to investigate the interplay between local (two- and three-body) and non-local interactions in low dimensional systems of ultracold dipolar bosons. We focus on a one dimensional geometry, and find that the phase diagram of such systems strongly resembles that of the spin-1 Heisenberg model with Ising-like and single ion anisotropy [202, 22, 203, 204, 205], or $\lambda - D$ model, extensively studied in the past in the contest of one-dimensional spin chains. We present numerical results on the phase diagram, which exhibits ferromagnetic, antiferromagnetic and hidden order phases, and finally discuss the stability of these phases in presence of a trapping potential and density fluctuations, as naturally present in cold atomic and molecular setups. Several of the magnetic phases discussed do not require strong dipolar interactions, and can thus be observed even with magnetic atoms, where dipolar interaction is usually much smaller than any other relevant energy scale[145].

The chapter is organized as follows: in Sec. 9.2, we describe the parallelism between constrained bosonic gases and spin systems and introduce the Hamiltonian, which is then investigated by DMRG simulations and strong coupling arguments in Sec. 9.3. In Sec. 9.4 we extend the numerical simulations to the inhomogeneous case; finally, we draw our conclusions in Sec. 9.5.

9.2 Bosonic Hamiltonian and λ-D model

Dipolar bosons confined in a one dimensional geometry and subject to a deep optical lattice are generally described by the following Hamiltonian [**?**]:

$$\begin{aligned}\mathcal{H} &= -t\sum_{\langle i,j\rangle} b_i^\dagger b_j + \frac{U}{2}\sum_i n_i\left(n_i-1\right) + \mu\sum_i n_i + \\ &+ k\sum_i (i-L/2)^2 n_i + \Lambda\sum_{i<j}\frac{n_i n_j}{(j-i)^3}. \end{aligned} \tag{9.1}$$

Here, $b_i^\dagger, b_i, n_i$ are bosonic creation, annihilation and number operator at site i, the first line describes the standard Bose-Hubbard model, where t is the hopping term between nearest neighbor sites and U the onsite interaction, and the last line includes trapping and long-distance dipolar potentials. The hopping coefficient t varies with the depth of the underlying optical lattice, whereas Λ can be tuned by varying the applied EC electric field; finally, the onsite interaction U depends on the short-distance details of the interparticle interaction[206] and, for magnetic atoms, can be controlled by using Feshbach resonances[43]. The phase diagram of Eq. (9.1) with $U > 0$ has been investigated in several regimes: at unitary filling, a new insulating phase characterized by hidden order has been predicted between a Mott insulator and a charge density wave[126, 198], whereas for densities $\bar{n} < 1$ and strong repulsive interaction $U \gg t$ a devil's staircase of insulating phases appears as a function of the chemical potential[179]. However, the attractive regime $U < 0$ has so far been neglected. This is partially due to the fact that losses given by strong three-body recombination are enhanced in this regime, thus making a time-dependent description of the system more suitable in order to take into account dissipative effects[207]. The situation can be though strongly simplified when the decay rate γ_3[93] associated with three-body loss processes is much larger than the typical tunneling rate, i.e. $\gamma_3 \gg t$: in this regime, a mechanism analogous to the quantum Zeno effect gives rise to an effective strong three-body repulsion, which can be implemented in the Hamiltonian with the additional condition $(b_i^\dagger)^3 = 0$[93].

The opportunity to engineer strong three-body repulsion has then two striking effects: *i)* the system is in general stable regardless of the sign of the couplings U, Λ and *ii)* the onsite Hilbert space is reduced to $|0\rangle, |1\rangle, |2\rangle$, thus resembling a spin-1 system. This correspondence is further clarified after introducing spin-1 operators S_i^+, S_i^-, S_i^z and performing the following mapping:

$$n_i = 1 - S_i^z, \qquad b_i^\dagger = \alpha S_i^- + \beta(S_i^z S_i^- + S_i^- S_i^z) \tag{9.2}$$

where $\alpha = (2+\sqrt{2})/4,\ \beta = -(2-\sqrt{2})/4$ are fixed by commutation relations, as described in appendix 9.5.1. From now on, we will consider a fixed density $\bar{n} = 1$, then obtaining (fixing $t = 1$):

$$\begin{aligned} \mathcal{H} &= -\sum_{<i,j>} S_i^+ S_j^- (J + J_1 S_i^z + J_2 S_j^z + J_3 S_i^z S_j^z) + \\ &+ \Lambda \sum_{i<j} \frac{S_i^z S_j^z}{(j-i)^3} + \frac{U}{2}\sum_i (S_i^z)^2 - k\sum_i (i - L/2)^2 S_i^z \end{aligned} \tag{9.3}$$

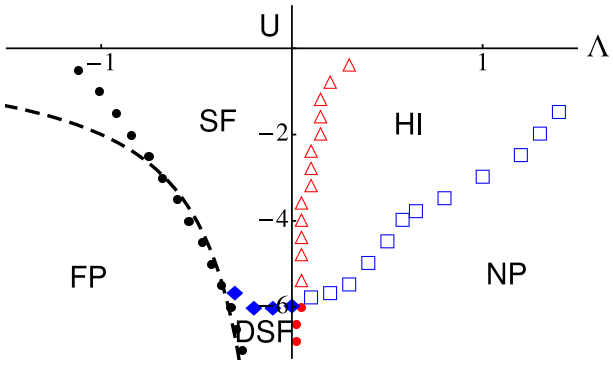

Figure 9.1: : homogeneous phase diagram for dipolar bosons on an optical lattice with three-body hard core constraint at filling $\bar{n} = 1$ (see text): triangles, squares, diamonds, black and red points denote numerical results, while the black dashed line describes an approximate strong coupling description for $|U| \gg J$.

where the first line includes a nearest-neighbor exchange with $J = \alpha^2 - \beta^2$ and correlated exchange terms with $J_1 = \sqrt{2}\beta$, $J_2 = 2\beta$ and $J_3 = 4\beta^2$, which break particle-hole symmetry, as required for constrained bosons.

We notice that Eq. (9.3) is a generalization of the so called $\lambda - D$ model[202], extensively studied over the last two decades both from analytical and numerical points of view.

The spin-1 $\lambda - D$ model presents a rich phase diagram: in addition to ferromagnetic and antiferromagnetic (AFM) phases, in a broad region of the parameter space competition between local and non-local interactions favors the so-called *Haldane phase* (as expected for integer spin chains[208, 209]), which displays a gap in the energy spectrum, a unique ground state (at least in the thermodynamic limit, whereas it is four-fold degenerate for chains of finite size), a finite correlation length, and thus no long-range order even if it is possible to define suitable string correlation functions that measure a hidden topological order. The spin liquid picture introduced by Tasaki[22] provides a intuitive understanding of the Haldane phase: let us assign the presence of an effective spin-$1/2$ particle with spin pointing up (down) if at the i-th lattice site $S_i^z = +1(-1)$ and no particles if $S_i^z = 0$. The Haldane phase is then interpreted as a liquid in which these effective particles carry no positional order along the chain but still retain antiferromagnetic (AFM) order in their effective spins. The positional disorder is associated with the absence of long-range order in

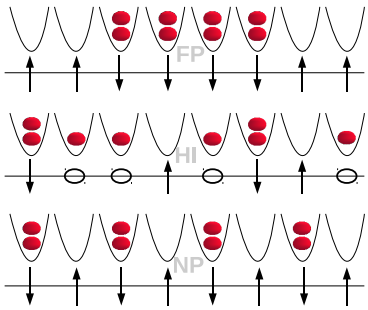

Figure 9.2: : cartoon of magnetic phases related to the model in Eq.(9.1,9.3): from top to bottom, ferromagnetic, Haldane and Néel phase in bosonic and spin language(see text).

the usual spin-1 correlation functions

$$\mathcal{C}_\alpha(j) = (-1)^j \langle S_i^\alpha S_{i+j}^\alpha \rangle \qquad \alpha = x, y, z \tag{9.4}$$

whereas the spin-$1/2$ magnetic order that we would get if all the sites with $S_i^z = 0$ were taken off from the chain is measured by the asymptotic value of the string order parameters (SOP)[124]:

$$\mathcal{O}_\alpha(j) = \langle S_l^\alpha e^{i\pi \sum_{l<k<j+l} S_k^\alpha} S_{l+j}^\alpha \rangle, \quad \alpha = x, y, z. \tag{9.5}$$

As shown thoroughly by Kennedy and Tasaki [203] the $\lambda - D$ model possesses an hidden (non-local) $Z_2 \times Z_2$ symmetry, and the non-vanishing values of the SOP can be understood as the breaking of such a symmetry.

9.3 Homogeneous phase diagram.

In order to exploit a complete parallelism between Eq. (9.3) and the $\lambda - D$ model, we investigate its phase diagram in the homogeneous case, $k = 0$, by means of numerical simulations based on the density-matrix renormalization group (DMRG) algorithm [28], truncating the dipolar interaction up to fifth-nearest-neighbors [210]. Let us summarize the main results, as schematically presented in Fig. 9.1: the $\Lambda > 0$ region displays *i)* an antiferromagnetic Néel-like phase (NP), where doubly occupied sites alternate with empty ones in a periodic pattern, *ii)* an Haldane insulator phase (HI), where doubly occupied and empty sites are separated by strings of single occupied ones[126, 211](see Fig. 9.2), and *iii)* two superfluid phases,

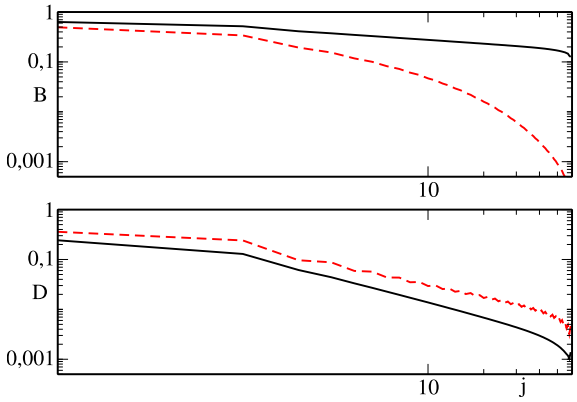

Figure 9.3: : superfluid correlations in double logarithmic scale as a function of the distance from the middle in a $L = 120$ chain. Red (dashed) and black (thick) lines represent DSF and SF phase respectively, with $U = -6.5, \Lambda = 0$ and $U = -3, \Lambda = 0.05$.

in which the superfluid components are single bosons (SF) and dimers (DSF) respectively. In the $\Lambda < 0$ regime, both superfluid phases collapse beyond a critical value of Λ into a ferromagnetic phase (FP), where the mutual attraction between bosons gives rise to a region of constant density $\bar{n} = 2$. The system thus displays all phases and phase transitions of the $\lambda - D$ model with attractive single-ion anisotropy; there are however some quantitative differences. First, both SF and DSF, which correspond to the XY phases in spin language, extend on a broad region around $\Lambda = 0$ due to the presence of correlated hopping terms which disadvantage long-range order. In addition, the HI region is present even at larger Λ, as expected due to long-range frustration of dipolar interactions with respect to antiferromagnetic ordering[126].

Different phases are uniquely characterized by the asymptotic decay of correlation functions[212]. In the SF phase, both single particle and dimer superfluid correlations

$$\mathcal{B}(j) = \langle b_i^\dagger b_{i+j} \rangle \propto \mathcal{C}_x(j), \quad \mathcal{D}(j) = \langle (b_i^\dagger)^2 (b_{i+j})^2 \rangle \tag{9.6}$$

decay algebraically; by contrast, in all other phases $\mathcal{B}$ is exponentially suppressed, whereas $\mathcal{D}$ decays algebraically in the DSF phase, as can be seen in Fig. 9.3. Magnetic phases are instead characterized by a non-vanishing asymptotic value of certain correlation functions: in the HI, both

9.3. Homogeneous phase diagram.

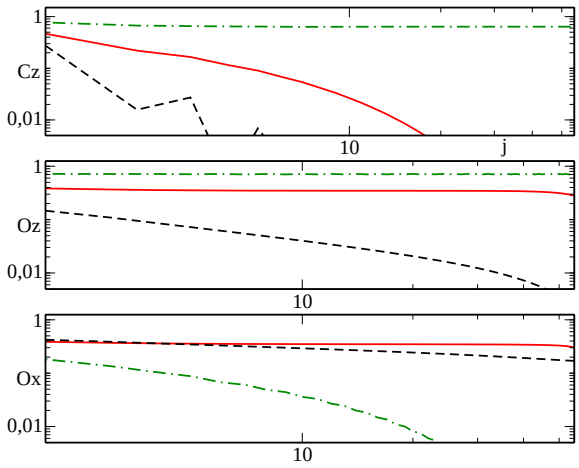

Figure 9.4: : magnetic order parameters in double logarithmic scale as a function of the distance from the middle in a $L = 120$ chain. Black (dashed), red (thick) and green (dot-dashed) represent $(U = -3, \Lambda = 0.05), (-3, 0.7), (-3, 1.3)$ respectively.

$\mathcal{O}_x, \mathcal{O}_z$ decay to a constant at long distances while $\mathcal{C}_z$ vanishes exponentially, whereas in the NP $\mathcal{O}_x$ decays exponentially and $\mathcal{O}_z, \mathcal{C}_z$ are constant. All magnetic order parameters decay at long distances in both SF and DSF phases. Correlation functions have been computed by analyzing systems of size L=60, 80, 100 and 120 sites, with up to 600 states per block, 4 sweeps and open boundary conditions. Fig. 9.4 describes typical decays in the SF (black, dashed), HI (red, thick) and NP (green, dot-dashed) of the magnetic order parameters.

Haldane insulator - Néel phase . Any one of the pairs $\{\mathcal{C}_z, \mathcal{O}_z\}$, $\{\mathcal{C}_z, \mathcal{O}_x\}$ or $\{\mathcal{O}_x, \mathcal{O}_z\}$ can be used to give an accurate description of the HI-NP boundary: from Figs. 9.5, 9.6, it can be inferred that the bulk asymptotic behavior of these correlators is well described already for $L = 60$. This feature is not surprising, considering that in the $\lambda - D$ model this transition is believed to belong to the Ising-type universality class[205]. However, the same cannot be said when considering the other phase transitions present in the model.

Superfluid - Dimer superfluid . The SF-DSF phase transition corresponds to a level crossing in the spectrum between excitations with $S^z = \pm 1$ and $S^z = \pm 2$, with finite size gaps Δ_1 and Δ_2 respectively [205]. This condition stems from the fact that, beyond a critical attraction $-U_c(\Lambda) \gg J$, a fi-

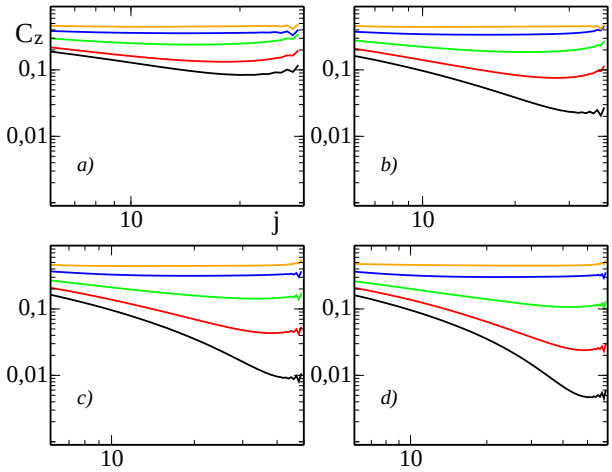

Figure 9.5: $\mathcal{C}_z(x)$ correlation function at the HI-NP boundary for chains of different lengths $L = 60, 80, 100, 120$, panels *a,b,c* and *d* respectively; correlations are taken with respect to the center of the chain. Here, $U = -3$, and, from top to bottom, $\Lambda = 1.1$ (orange), $\Lambda = 1.05$ (blue), $\Lambda = 1$ (green), $\Lambda = 0.95$ (red) and $\Lambda = 0.9$ (black).

nite energy is required to break *dimers*, and thus exciting the system in the $S^z = \pm 1$ sector would become energetically unfavorable. We determine the phase boundary (marked by blue diamonds in Fig. 9.1) by calculating finite size gaps

$$\Delta_{\alpha=1,2}(L) = \frac{\mathcal{E}(N+\alpha; L) + \mathcal{E}(N-\alpha; L) - 2\mathcal{E}(N; L)}{2}$$

for periodic chains of several lengths and then by imposing that, at the phase transition, the condition $\lim_{L\to\infty}(\Delta_1(L) - \Delta_2(L)) = 0$ is satisfied; a typical set of data for $\Lambda = -0.1$ is presented in Fig. 9.7.

Superfluid - Haldane insulator and Dimer superfluid - Néel phase . Finite size calculations are also useful to better shape the SF-HI and DSF-NP transitions, which, in analogy with the $\lambda - D$ model[213, 214, 215], should belong to the Berezinskii-Kosterlitz-Thouless (BKT) universality class[12], albeit the non trivial nature of non-local interaction can in principle lead to different critical behaviors. BKT transitions are usually hard to determine due to the exponential opening of the gap; however, string order parameters have been shown to provide a rather accurate estimate of the transition points[213, 215]. In the following, we consider systems with periodic boundary conditions, in order to avoid boundary effects, with up

9.3. Homogeneous phase diagram.

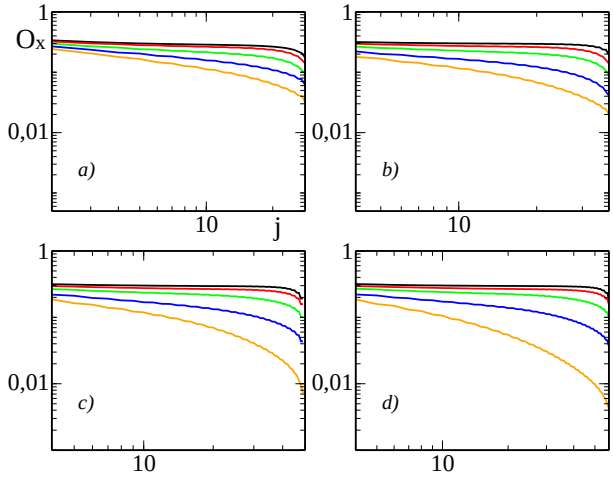

Figure 9.6: String correlator $\mathcal{O}_x(x)$ at the HI-NP boundary for chains of different lengths $L = 60, 80, 100, 120$, panels *a,b,c* and *d* respectively; correlations are taken with respect to the center of the chain. Here, $U = -3$, and, from top to bottom, $\Lambda = 0.9$ (black), $\Lambda = 0.95$ (red), $\Lambda = 1$ (green), $\Lambda = 1.05$ (blue) and $\Lambda = 1.1$ (orange).

to $L = 42$ sites, and calculate the string order parameter from the first to the $L/2 + 1$ site, $\mathcal{O}_z(x - x' = L/2)$, which represents a suitable order parameter for both SF-HI and DSF-NP transitions[205]. Then, we estimate its asymptotic value C_1 by fitting the datas with the following scaling form:

$$\mathcal{O}_z(L/2) = C_1 + \frac{C_2}{L^{C_3}}. \tag{9.7}$$

This method has been successfully employed to study the same transition in the $\lambda - D$ model within an exact diagonalization approach[213]. The usual error of this procedure is related to the DMRG truncation error, always smaller than $3 * 10^{-5}$, and to the algebraic fit [106]: by employing numerical datas with $20 \leq L \leq 42$, we then estimate that the asymptotic value C_1 is non-vanishing within numerical error as long as $C_1 > 0.005$. A typical example of the estimate of C_1 is described in Fig. 9.8, where different datas are presented for $U = -0.8, 0.1 \leq \Lambda \leq 0.5$. In Fig. 9.9, we plot C_1 as a function of both U (fixing $\Lambda = 0.1, 0.2, 0.3$) and Λ (fixing $U = -0.8, -2$); the asymptotic value of the string order parameter increases with both Λ and $|U|$. The corresponding transition points are marked by red triangles in Fig. 9.1.

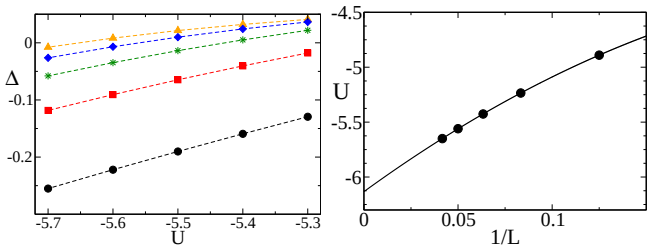

Figure 9.7: *Left panel*: dependence of $\Delta = \Delta_1 - \Delta_2$ on U for $\Lambda = -0.1$ and different chain lengths: $L = 8$ (black circles), $L = 12$ (red squares), $L = 16$ (green stars), $L = 20$ (blue diamond) and $L = 24$ (orange triangles). Dashed lines are guides for the eye. *Right panel*: critical value of the SF-DSF transition as a function of $1/L$ for $\Lambda = -0.1$; circles represent numerical datas, line is a best fit of the type $a_1 + a_2/L + a_3/L^2$.

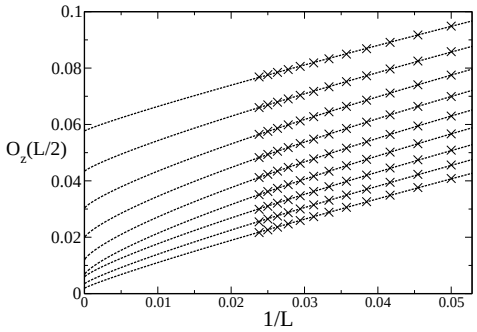

Figure 9.8: Finite-size scaling of $\mathcal{O}_z(L/2)$ for $U = -0.8$ by using Eq. (9.7) (see text). From top to bottom: $\Lambda = 0.5, 0.45, 0.4, 0.35, 0.3, 0.25, 0.2, 0.15$ and 0.1.

Ferromagnetic phase - Superfluid . A clear evidence of the FP-SF transition emerges instead when the ground state energy density $\mathcal{E}_{GS}(L)$ approaches the exact value for ferromagnetic states $\mathcal{E}_{FP}$ in the thermodynamic limit[205]. The transition line, marked by black dots in Fig.(9.1), is obtained by requiring that $\lim_{L\to\infty} \mathcal{E}_{GS}(L) = \mathcal{E}_{FP}$.

9.3.1 Strong coupling regime

In the large $|U|$ regime, the quantitative difference between dipolar and nearest-neighbor(NN) interaction can be investigated with a perturbative argument. If $|U| \gg |\Lambda|, J$, the effective Hilbert space is reduced to $S^z = \pm 1$,

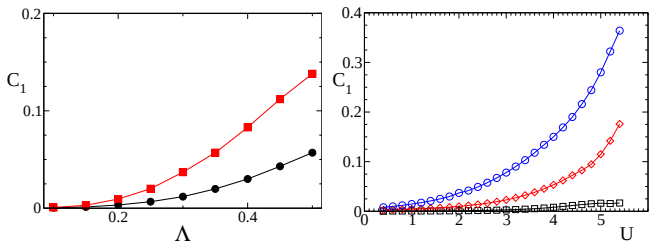

Figure 9.9: *Left panel*: string order parameter C_1 for $U = -0.8, -2$ (black circles and red squares respectively) as a function of Λ. *Right panel*: C_1 for $\Lambda = 0.1, 0.2, 0.3$ (black squares, red diamonds and blue circles respectively) as a function of U. In both panels, lines are guide for the eye.

that is, bosons are tightly bound in dimers, so that we can map the spin-1 problem into a spin-$1/2$ theory employing the following identities[214]:

$$S_i^z = 2s_j^z, \qquad S_j^+ S_j^+ = 2s_j^+, \qquad S_j^- S_j^- = 2s_j^- \tag{9.8}$$

$$S_j^+ S_j^- = 2(1/2 + s_j^z), \qquad S_j^- S_j^+ = 2(1/2 - s_j^z) \tag{9.9}$$

where $\vec{s}$ is a spin-$1/2$ operator. After a proper rescaling, the strong coupling Hamiltonian including only NN interaction is mapped into a spin-$1/2$ XXZ chain:

$$H_{sc} = \sum_{<i,j>} (s_i^+ s_j^- + (1-\Delta) s_i^z s_j^z), \quad \Delta = -2/\Lambda|U|. \tag{9.10}$$

From the exact solution of Eq.(9.10)[216], we argue that the system is in a DSF phase as long as $-\frac{2}{|U|} \leq \Lambda \leq 0$; the DSF-FP and DSF-NP transitions are located at $\Lambda_{NN}^{(c)} = -\frac{2}{|U|}, 0$ respectively. We can now compare this criterion, derived considering only NN interactions, with the numerical one, obtained from DMRG as previously described. The DSF-FP transition (black dashed line in Fig.9.1) is then predicted at $-\Lambda \simeq 2/|U|$, whereas numerical values (including dipolar interaction) for, e.g., $U = -10$, indicate $-\Lambda \simeq 1.75/|U|$; in this regime, dipolar interactions show a small quantitative difference with respect to standard NN couplings.

9.4 Effect of a trapping potential.

The observation of the different magnetic orders discussed above in a standard cold atom experiment is strictly related to the possibility of stabilizing these phases even in an inhomogeneous background. In fact, atoms

and molecules are loaded into a trapping potential, which introduces a position-dependent term in the Hamiltonian with a minimum at the trap center, namely, the first term in the second line of Eq.(9.1). In this setup, another energy scale comes into play; particles will try to minimize their potential energy by concentrating in the middle of the trap, thus displaying a strong spatial dependence of the local density $\langle n_i \rangle$. This feature is in sharp contrast to the ideal configuration needed to realize the magnetic phases described above, all of them requiring a constant density in the thermodynamic limit. Our goal here is to investigate what are the proper trap configurations needed to stabilize a magnetic phase in this inhomogeneous setup: in particular, we will focus our attention to the region in the middle of the confining potential, where it is usually easier to create large regions of space at constant density[44, 217]. First of all, let us briefly discuss what happens the in the FP: in analogy to a standard Mott-like phase[44], it can always be realized by considering a sufficiently strong trap such that the density is maximized in the middle, $\langle n_i \rangle = 2$. This simple argument cannot be extended to neither HI or NP: in fact, a very strong trap will simply destroy these types of order. In this section, we will thus focus on the stability of these two orders in presence of a trapping potential.

We identify a certain magnetic order in a region of space by requiring that *i)* the region is at constant density, $\langle n_i \rangle = 1$, and *ii)* the proper order parameters with respect to the middle of the trap, defined as:

$$\mathcal{O}_{\alpha=x,z}(L/2, j) = \langle S^{\alpha}_{L/2} e^{i\pi \sum_{L/2<k<j+L/2} S^{\alpha}_{k}} S^{\alpha}_{L/2+j} \rangle \tag{9.11}$$

$$\mathcal{C}_{z}(L/2, j) = (-1)^{j} \langle S^{z}_{L/2} S^{z}_{L/2+j} \rangle \tag{9.12}$$

where j is the distance from $L/2$, behave as expected in the HI or in the NP up to a certain range. We performed DMRG simulations on a $L = 80$ sites chain, fixing as energy unit for the trapping potential $k^* = 1/(L/2)^2 = 1/1600$, and kept as much as 600 states per block with 10 finite-size sweeps [28]. Since a trapping potential favors a configuration where the particles are in the middle of the chain, we focused on a $N = 40$ particles system: this assures that the density close to the chain boundary rapidly goes to zero, thus avoiding possible finite-size effects and, at the same time, allows for a constant density of order 1 in the middle of the system.

9.4.1 Haldane order

We start our treatment by considering the possibility to stabilize hidden order in an inhomogeneous system. As a sample configuration, we fixed

9.4. Effect of a trapping potential.

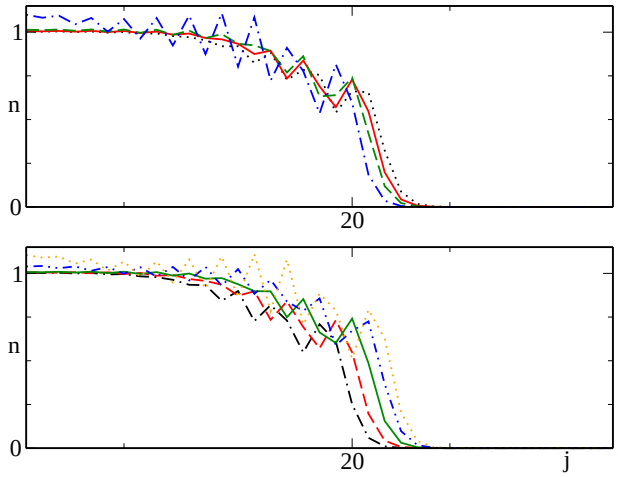

Figure 9.10: : density distribution as a function of the distance from the trap center for $U = -2.5, \Lambda = 0.9$. *Top panel*: fixed population $N = 40$ and different trap strength $k = 7.5k^*$ (black, dotted), $8.5k^*$ (red, thick), $9.5k^*$ (green, dashed) and $10.5k^*$ (blue, dot-dashed). *Bottom panel*: fixed trap strength $k = 9k^*$ and different populations: N=36 (black, dot-dashed), 38 (red, dashed), 40 (green, thick), 42 (blue, dot-dot-dashed) and 44 (orange, dotted).

$U = -2.5, \Lambda = 0.9$ such that the corresponding homogeneous phase at integer filling is an HI. In a very shallow trap, the non-local interparticle repulsion would drive the system in a very dilute limit with $\langle n_i \rangle < 1$ all over the trap, whereas in the opposite strong trap limit, an high density region with $\langle n_i \rangle > 1$ would be stabilized in the middle. We shall then focus on an intermediate regime in order to satisfy the density requirement $\langle n_i \rangle = 1$ needed in the HI.

In Fig. 9.10, upper panel, we plot the density distribution as a function of the distance from the trap center for different values of k, $7.5 \leq k/k^* \leq 10.5$: the requirement $\langle n_i \rangle = 1$ is satisfied for values of the trap strength inside the interval $8.5 \leq k/k^* \leq 9.5$. In order to verify whether hidden order is present or not, we plot the relevant magnetic order parameters as defined in Eqs. 9.11, 9.12 in Fig. 9.11; in the interval $8.5 \leq k/k^* \leq 9.5$, the string order parameter $\mathcal{O}_z$ is constant up to a certain distance from the trap, and at the same time $\mathcal{C}_z$ decays, then proving that particles close to the trap center display HI; outside of the constant density region, the order is lost, as can also be seen by looking at $\mathcal{O}_z$.

However, while an accurate fine tuning of the trap strength does not

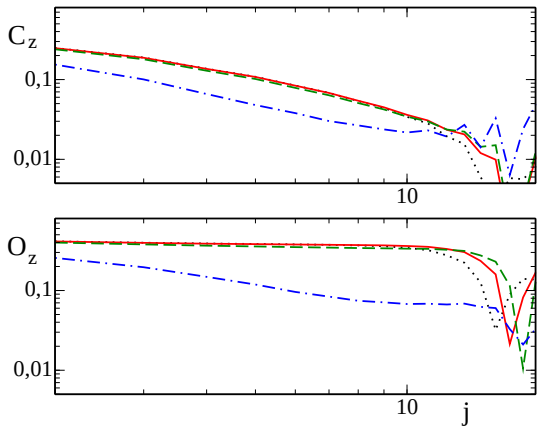

Figure 9.11: : magnetic order parameters $\mathcal{C}_z(L/2, j)$ (top panel) and $\mathcal{O}_z(L/2, j)$ (bottom panel) as a function of the distance from the trap center for $U = -2.5, \Lambda = 0.9, N = 40$ and different values of k: $k = 7.5k^*$ (black, dotted), $8.5k^*$ (red, thick), $9.5k^*$ (green, dashed) and $10.5k^*$ (blue, dot-dashed).

present major difficulties in a typical experimental setup, a proper control over populations in a tube is challenging, and it is thus instructive to investigate small population unbalance with respect to the previous $N = 40$ case. In Fig. 9.10, lower panel, we plot the density distribution at a fixed trap strength $k = 9k^*$ for different total number of particles $N = 36, 38, 40, 42$ and 44, while the corresponding order parameters are plotted in Fig. 9.12. We notice that the Haldane phase is unstable when $N \geq 42$ since too many particles concentrate in the middle of the trap, whereas it is stable for $N \leq 40$; we can then conclude that a large population difference of order $\delta N \sim 0.1$ prevents the HI phase to stabilize in the center of the trap.

9.4.2 Antiferromagnetic ordering

We turn now our attention to the NP by fixing $U = -4, \Lambda = 1.5$. As already discussed for the HI, a very shallow trap is not sufficient to stabilize antiferromagnetic order in the trap due to density requirements, whereas a too strong trap would prevent it by concentrating too many particles in the trapping potential minimum. The density distribution as a function of the trap strength in the interval $5 \leq k/k^* \leq 20$ is presented in Fig. 9.13, upper panel; a large region with $\langle n_i \rangle = 1$ is stable in the middle as long as

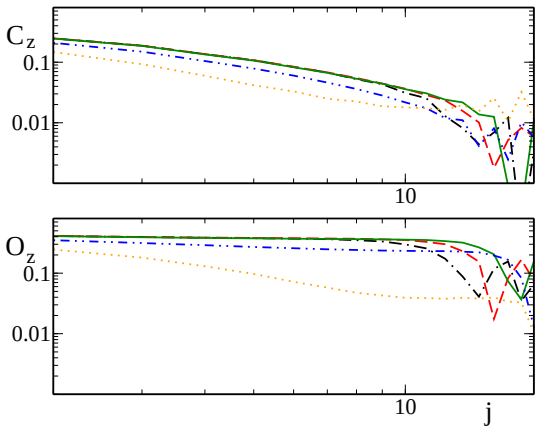

Figure 9.12: : magnetic order parameters $\mathcal{C}_z(L/2, j)$ (top panel) and $\mathcal{O}_z(L/2, j)$ (bottom panel) as a function of the distance from the trap center for $U = -2.5, \Lambda = 0.9, k = 9k^*$ and different number of particles N=36 (black, dot-dashed), 38 (red, dashed), 40 (green, thick), 42 (blue, dot-dot-dashed) and 44 (orange, dotted).

$k > 5k^*$, and, remarkably, the size of this region increases with increasing k, including up to 30 particles when $k = 20k^*$. The corresponding magnetic order parameters are plotted in Fig. 9.14; both $\mathcal{C}_z$ and $\mathcal{O}_z$ are constant in the middle of the trap as long as $k > 5k^*$, and their plateau extends all over the constant density region.

Small changes in the total number of particles do not alter this picture significantly. In Fig. 9.13, lower panel, we plot the density distribution at a fixed trap strength $k = 12k^*$ and different total number of particles $N = 36, 38, 40, 42$; a constant region in the middle of the trap is always present and, in addition, it displays antiferromagnetic correlations, as can be inferred from the magnetic order parameters presented in Fig. 9.15.

We can then conclude that, while both the HI and NP are incompressible, the former requires a finer tuning of the trapping potential and a more accurate control of the population of the system in order to be stabilized in the centre of the trap.

9.5 Conclusions

We have investigated the effect of a three-body hard-core constraint in a one dimensional system of dipolar bosons such as magnetic atoms or polar molecules confined in a one dimensional tube by optical lattices. After

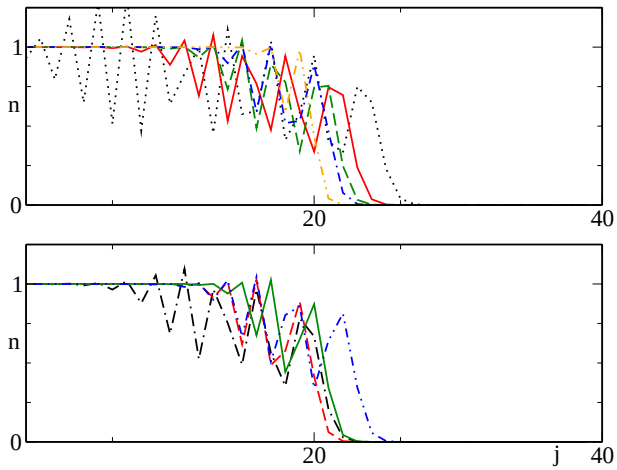

Figure 9.13: : density distribution as a function of the distance from the trap center for $U = -4, \Lambda = 1.5$. *Top panel*: fixed population $N = 40$ and different trap strength $k = 5k^*$ (black, dotted), $7k^*$ (red, thick), $9k^*$ (green, dashed), $11k^*$ (blue, dot-dashed) and $20k^*$ (orange, dot-dot-dashed). *Bottom panel*: fixed trap strength $k = 12k^*$ and different populations: N=36 (black, dot-dashed), 38(red, dashed), 40 (green, thick) and 42 (blue, dot-dot-dashed).

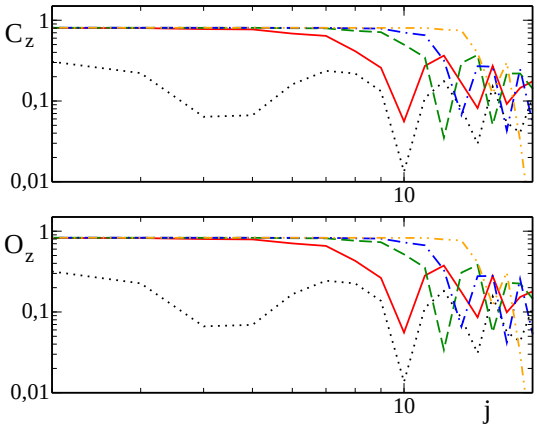

Figure 9.14: : magnetic order parameters $\mathcal{C}_z(L/2, j)$ (top panel) and $\mathcal{O}_z(L/2, j)$ (bottom panel) as a function of the distance from the trap center for $U = -4, \Lambda = 1.5, N = 40$ and different values of k: $k = 5k^*$ (black, dotted), $7k^*$ (red, thick), $9k^*$ (green, dashed), $11k^*$ (blue, dot-dashed) and $20k^*$ (orange, dot-dot-dashed).

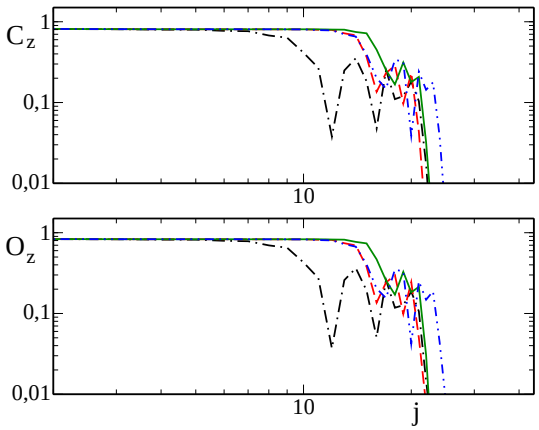

Figure 9.15: : magnetic order parameters $\mathcal{C}_z(L/2,j)$ (top panel) and $\mathcal{O}_z(L/2,j)$ (bottom panel) as a function of the distance from the trap center for $U=-4, \Lambda=1.5, k=12k^*$ and different number of particles: N=36 (black, dot-dashed), 38(red, dashed), 40 (green, thick) and 42 (blue, dot-dot-dashed).

mapping the original problem in spin language, a strong parallelism between the system and the $\lambda - D$ model is established and confirmed by DMRG calculations; we have shown that ferromagnetic, antiferromagnetic and hidden orders can be stabilized in this framework, and that dipolar interactions give rise to small quantitative changes in the phase diagram with respect to more usual nearest-neighbor interactions.

Finally, we have considered the effect of a confining potential, as usually present in cold atomic gas experimental setups. Remarkably, both HI and FP can be stabilized in a large region in the middle of the trap even if the total population is not exactly controlled; the realization of the HI needs however an appropriate trap tuning. This feature opens up the possibility to observe strongly correlated phases in cold gases of magnetic atoms such as *Dy*, *Cr* or *Er*[146, 145], which are usually characterized by relatively small dipolar interactions. All of these phases can be probed via noise correlations[218], or, in the HI case, via Bragg spectroscopy[126] or in-situ imaging[219, 217]. Finally, this setup can be adapted to investigate spin-1 Heisenberg-like models in 2-D systems, where various interesting phases such as field induced supersolidity have been recently suggested[220] or else extended in order to consider the effect of disorder in such systems.

9.5.1 Addendum: constrained bosons - spin-1 mapping

The constraint $\left(b^\dagger\right)^3|0\rangle = 0$ allows us to make the following correspondence between the reduced bosonic Hilbert space and that of a spin-1

$$|0\rangle \to |\uparrow\rangle \qquad |1\rangle \to |\tilde{0}\rangle \qquad |2\rangle \to |\downarrow\rangle \tag{9.13}$$

where $|\uparrow\rangle$, $|\tilde{0}\rangle$ and $|\downarrow\rangle$ are eigenstates of S^z with eigenvalues $+1$, 0 and -1 respectively. The corresponding operator mapping is:

$$b^\dagger b = 1 - S^z \tag{9.14}$$

$$b = \alpha S^+ + \beta\left(S^z S^+ + S^+ S^z\right) \tag{9.15}$$

where the coefficients α, β have to be determined by imposing the correct action on the Hilbert space and commutation relations. Verifying the former, we have:

$$\begin{array}{ll} b|0\rangle = 0 & \left[\alpha S^+ + \beta\left(S^z S^+ + S^+ S^z\right)\right]|\uparrow\rangle = 0 \\ b|1\rangle = |0\rangle & \left[\alpha S^+ + \beta\left(S^z S^+ + S^+ S^z\right)\right]|\tilde{0}\rangle \\ & = \left(\alpha\sqrt{2} + \beta\sqrt{2}\right)|\uparrow\rangle \end{array} \tag{9.16}$$

$$\begin{array}{ll} b|2\rangle = \sqrt{2}|1\rangle & \left[\alpha S^+ + \beta\left(S^z S^+ + S^+ S^z\right)\right]|\downarrow\rangle \\ & = \left(\alpha\sqrt{2} - \beta\sqrt{2}\right)|\tilde{0}\rangle. \end{array} \tag{9.17}$$

It follows then

$$\alpha + \beta = \frac{1}{\sqrt{2}} \qquad\qquad \alpha - \beta = 1. \tag{9.18}$$

Furthermore, if we write down the number operator in terms of spin-1 operators

$$\begin{aligned} b^\dagger b \to \mathcal{S} &= \alpha^2 S^- S^+ + \beta^2\left(S^- S^z S^+ S^z + S^- S^z S^z S^+ + \right. \\ &+ \left. S^z S^- S^+ S^z + S^z S^- S^z S^+\right) \\ &+ \alpha\beta\left(S^- S^+ S^z + 2S^- S^z S^+ + S^z S^- S^+\right) \end{aligned} \tag{9.19}$$

and we apply it to number eigenstates, we get:

$$\begin{array}{ll} b^\dagger b|0\rangle = 0 & \mathcal{S}|\uparrow\rangle = 0 \\ b^\dagger b|1\rangle = |1\rangle & \mathcal{S}|\tilde{0}\rangle = 2\left(\alpha+\beta\right)^2|\tilde{0}\rangle = |\tilde{0}\rangle \\ b^\dagger b|2\rangle = 2|2\rangle & \mathcal{S}|\downarrow\rangle = 2\left(\alpha-\beta\right)^2|\downarrow\rangle = 2|\downarrow\rangle. \end{array} \tag{9.20}$$

9.5. Conclusions

We will now show that the operators defined by our mapping satisfy the correct commutation relations. Since we are considering constrained bosons the usual bosonic commutation relation becomes[221]

$$\left[b, b^{\dagger}\right] = |0\rangle\langle 0| + |1\rangle\langle 1| - 2|2\rangle\langle 2|. \tag{9.21}$$

Recalling that

$$\begin{aligned} \left[S^{+}, S^{-}\right] &= 2S^{z} \\ \left\{S^{+}, S^{-}\right\} &= 2\left(S\left(S+1\right) - \left(S^{z}\right)^{2}\right) \end{aligned} \tag{9.22}$$

we have

$$\left[b, b^{\dagger}\right] = -8\alpha\beta + 2\left(\alpha^{2} + \beta^{2}\right) S^{z} + 12\alpha\beta\left(S^{z}\right)^{2} \tag{9.23}$$

and then

$$\langle 0|\left[b, b^{\dagger}\right]|0\rangle = 2\left(\alpha+\beta\right)^{2} = 1$$

$$\langle 1|\left[b, b^{\dagger}\right]|1\rangle = -8\alpha\beta = 1 \tag{9.24}$$

$$\langle 2|\left[b, b^{\dagger}\right]|2\rangle = -2\left(\alpha-\beta\right)^{2} = -2.$$

In order these relations to be satisfied we must have

$$\alpha = \frac{2+\sqrt{2}}{4} \qquad \beta = -\frac{2-\sqrt{2}}{4}. \tag{9.25}$$

Chapter 9. Magnetic phases with long-range interactions: hidden order via three-body losses

Conclusions and perspectives

We discussed two relevant aspects of cold atomic gases confined in low dimensional geometries. In the first part, we proved that quantum simulators of 1D quantum field theories can provide accurate answers at the many-body level, by comparing results of integrable models with experimental datas. Then, we investigated some fermionic and bosonic models with allow to stabilize very interesting phases: phase separation, topological and crystalline order, quantum magnetism and atomic color superfluidity are the main examples of our findings. In the last part, we turned our attention to the role of non-local interactions in 1D, starting from basic results on TLLs and Mott insulators, then moving towards exotic pairing and magnetic phases. We discuss in each chapter possible experimental realization of our theoretical findings, with particular attention to external potentials and typical parameter regimes reachable in state of art experiments.

Even though the interest in 1D physics has strongly increased in recent years, there is still very interesting physics to be explored, and cold molecules and atoms in optical lattices provide an almost ideal setup to compare theory with experiments. While *equilibrium* physics is well understood, exotic phenomena related, e.g., to non trivial dipolar interactions can emerge even in simple geometrical setups. Furthermore, *out-of-equilibrium* phenomena have been under the microscope in the last few years, and despite several interesting results, a complete understanding is still missing. In this context, the possibility to adapt the rich equilibrium formalism to out-of-equilibrium situation may strongly improve our understanding of several interesting many-body problems such as open quantum systems, quantum quenches and thermalization.

Chapter 9. Magnetic phases with long-range interactions: hidden order via three-body losses

Acknowledgements

Eccoci arrivati, o quasi. Innanzitutto, vorrei ringraziare la mia relatrice, Prof.sa Elisa Ercolessi, per le innumerevoli discussioni, gli input continui e il supporto lungo questi tre anni, ma soprattutto per aver limitato il mio animo scientifico a volte troppo dispersivo. Vivaci ringraziamenti anche a tutti i membri del gruppo, Luca Barbiero, Davide Cornigli, Cristian Degli Esposti Boschi, Marco Mattioli, Giuseppe Morandi, Fabio Ortolani, Luca Taddia ed anche a Stefano Evangelisti e Francesco Ravanini. Un ringraziamento particolare a Mario Di Dio, immancabile compagno d'ufficio in questi 3 anni. Vorrei inoltre ringraziare tutto il gruppo del Prof. Peter Zoller, che mi ha fatto sentire a casa tra le montagne tirolesi, in particolare Markus, Sebastian e Guido, che molto mi hanno aiutato nei primi, non facili momenti.

Le discussioni avute in questi anni sono state innumerevoli, e sarebbe poco pratico ringraziare tutte le persone con le quali mi sono confrontato criticamente e con piacere. Grazie mille ad Andrea Trombettoni, Walter Hofstetter e Jeff Kimble per avermi ospitato rispettivamente a Trieste, Francoforte e Caltech, a Marco Casadei e Tommaso Roscilde per le varie discussioni avute durante le nostre collaborazioni, e a Francesco Minardi, Giacomo Lamporesi, Jacopo Catani e tutti gli altri membri del LENS e al gruppo di Hanns-Christoph Nägerl per avermi fatto capire che sono un teorico, e che purtroppo la fisica non è sempre così arrendevole come sul foglio di carta...

Un grazie fortissimo a tutti i miei familiari, dalle nonne agli ultimi arrivati, per i momenti di gioia e le chiacchere rilassanti, e ai miei genitori, Anna e Rino, per la grandiosa disponibilità e il supporto immancabile, *in combutta* con Michele e Matilde. Un grazie a tutti gli imolesi, agli emigrati e agli irriducibili, e a tutte le nuove conoscenze bolognesi che in questi anni mi hanno accompagnato.

Ed un grazie a *LaVale*, raggio di luce dei miei giorni bui e carezzevole brezza di quelli felici.

Chapter 9. Magnetic phases with long-range interactions: hidden order via three-body losses

List of Figures

1.1 Typical examples of analog quantum simulators 12
1.2 Superfluid to Mott insulator quantum phase transition as realized in Ref. [5] 13

2.1 Comparing two types of superfluid-to-Mott-insulator phase transitions in 1D. 16
2.2 Modulation spectroscopy on bosons in 1D. 20
2.3 Transport measurements on the 1D Bose gas. 22
2.4 Phase diagram for the strongly interacting 1D Bose gas. . . . 24
2.5 Fermi surface of atoms in an optical lattice 31
2.6 Phase separation in a two-species Fermi gas 33
2.7 Scattering properties and three-body losses in ^{6}Li 34

3.1 Cartoons of some possible particle configurations in the asymmetric Hubbard model 38
3.2 Cubic spline extrapolation of CDW/SS transition point. . . . 39
3.3 Numerical results on the CDW/SS transition line 41
3.4 Analytical estimates of $\bar{z}(n)$. 45
3.5 Energy density for the half filled HP in the AHM 46
3.6 Second order contributions at half-filling 47
3.7 Weak-coupling phase diagram 49
3.8 Spatial density profiles for $z = 0.1, n = 0.2, u = 100$ 53
3.9 Spatial density profiles for $z = 0.5, 0.9, n = 0.2, u = 100$ . . . 55
3.10 Strong coupling phase diagram for $n = 0.4$ 58
3.11 Strong coupling phase diagram for $n = 0.9$ 58

4.1 Phase diagram of mass unbalanced atomic mixtures. 64
4.2 Numerical results for repulsive atomic mixtures 68
4.3 String ordering in atomic mixtures. 69
4.4 Momentum distribution of hard-core bosonic mixtures. . . . 71

5.1 Qualitative phase diagram for a 3-species attractive Fermi gas. . . . 75
5.2 Correlation functions with and without three-body constraint 78
5.3 Hubbard parameters for ^{6}Li and time dependent protocol. . 81

6.1 Finite-size gap scaling for commensurate Bose-Bose mixtures. 87
6.2 Spin and charge gap scaling for commensurate Bose-Bose mixtures. . . . 88
6.3 Condensate profile of a ^{52}Cr ferrofluid 92
6.4 Phase diagram of 2D dipolar gases on a lattice 93
6.5 Loss rates for RbK molecules in 3D 94

7.1 Experimental setup and soliton/antisoliton excitations. . . . 99
7.2 Commensurate phase diagram for long-range interacting bosons. . . . 101
7.3 TLL parameter: dipolar interactions and Calogero-Sutherland model. . . . 104

8.1 Sketch of a two-leg ladder and phases. . . . 108
8.2 Balanced phase diagram 111
8.3 Unbalanced phase diagram. . . . 114

9.1 Phase diagram of constrained dipolar bosons. . . . 120
9.2 Cartoons of some magnetic phases. . . . 121
9.3 SF and DSF correlations. . . . 122
9.4 Magnetic order parameters. . . . 123
9.5 $\mathcal{C}_z$ correlation at the HI-NP border. . . . 124
9.6 $\mathcal{O}_x$ correlation at the HI-NP border. . . . 125
9.7 SF-DSF transition: gap scaling. . . . 126
9.8 FInite-size scaling of the string order parameter. . . . 126
9.9 String order parameter as a function of U, Λ. . . . 127
9.10 Density distribution in the inhomogeneous HI. . . . 129
9.11 Correlation functions in the inhomogeneous HI. . . . 130
9.12 Correlation functions in the inhomogeneous HI; II. . . . 131
9.13 Density distribution in the inhomogeneous NP. . . . 132
9.14 Correlation functions in the inhomogeneous NP. . . . 132
9.15 Correlation functions in the inhomogeneous NP; II. . . . 133

Bibliography

[1] G. Galilei, *Il Saggiatore* (1623); see also S. Drake, *Discoveries and Opinions of Galileo*, Doubleday & Co., New York (1957).

[2] N. Metropolis *et al.*, Jour. Chem. Phys. **21**, 6, 1087 (1953).

[3] R. Feynman, Int. J. Theor. Phys. **21**, 467 (1982).

[4] D. Jaksch, C. Bruder, J. I. Cirac, C. Gardiner and P. Zoller, Phys. Rev. Lett. **81**, 3108 (1998).

[5] Greiner, M. *et al.*, *Nature* **415**, 39-44 (2002).

[6] S. Jochim *et al.*, Science **302**, 2101 (2003).

[7] M. Greiner, C. A. Regal and D. S. Jin, Nature **426**, 537 (2003).

[8] B. Paredes et al., Nature 429, 277 (2004).

[9] T. Kinoshita, T. Wenger and D. S. Weiss, Science **305**, 1125 (2004).

[10] A.O. Gogolin, A.A. Nersesyan, A.M. Tsvelik, *Bosonization and strongly correlated systems*, (Cambridge University press, Cambridge, 1998).

[11] T. Giamarchi, *Quantum Physics in one dimension*, (Oxford University press, Oxford, 2003).

[12] S. Sachdev, *Quantum Phase Transitions*, Cambridge University, Cambridge (1998).

[13] G. Parisi, *Statistical Field Theory*, Perseus Books, Reading (Massachusetts) (1998).

[14] G. Morandi, F. Napoli and E. Ercolessi, *Statistical Mechanics*, World Scientific, Singapore (2001).

[15] N. D. Mermin and H. Wagner, Phys. Rev. Lett. **17**, 1133 (1966).

[16] A. Auerbach, *Interacting electrons and quantum magnetism*, Springer-Verlag, New York (1994).

[17] P. C. Hohenberg, Phys. Rev. **158**, 383 (1966).

[18] N. N. Bogoliubov, Phys. Ab. Sov. **6**, 1, 113, 229 (1962).

[19] A. Gelfert and W. Nolting, J. Phys. Cond. Matt. **13**, R505 (2001).

[20] S. Coleman, Comm. Math. Phys. **31**, 259 (1973).

[21] M. P. A. Fisher *et al.*, Phys. Rev. B **40**, 546 (1989).

[22] H. Tasaki, Phys. Rev. Lett. **66**, 798 (1991).

[23] P. Di Francesco, P. Mathieu and D. Sénéchal, *Conformal Field Theory*, Springer-Verlag, New York (1997).

[24] C. Gomez, M. Ruiz-Altaba, G. Sierra, *Quantum Groups in Two-dimensional Physics*, Cambridge University Press, Cambridge (1996).

[25] A. A. Belavin, A. M. Polyakov and A. B. Zamolodchikov, Nucl. Phys. B **241**, 2, 333 (1984).

[26] A. A. Abrikosov, L. P. Gorkov and I. E. Dzyaloshinski, *Methods of Quantum Field Theory in Statistical Physics*, Dover Pubblications, New York (1975).

[27] P. Jordan and E. P. Wigner, Z. Phys. **47**, 631 (1928).

[28] S.R.White, Phys. Rev. Lett. **69**, 2863 (1992); Phys. Rev. B **48**, 10345(1993).

[29] U. Schollwöck, Rev. Mod. Phys. **77**, 259 (2005).

[30] C. N. Yang and C. P. Yang, Jour. Math. Phys. **10**, 1115 (1969).

[31] S.I. Tomonaga, Prog. Theor. Phys. **5**, 544(1950).

[32] J. M. Luttinger, J. Math. Phys. **4**, 1154 (1963)

[33] F.D.M. Haldane, Phys. Rev. Lett., **47**, 1840 (1981).

[34] K. von Klitzing, G. Dorda and M. Pepper, Phys. Rev. Lett. **45**, 494 (1980).

[35] J.G. Bednorz and K.A. Mueller, Z. Phys. B **64**, 189(1986).

[36] A. Geim, Science **324**, 5934 (2009).

[37] M. Bockrath *et al.*, Nature **397**, 598 (1999).

[38] M. Z. Hasan and C. L. Kane, Rev. Mod. Phys. **82**, 3045 (2010).

[39] A. M. Chang, L. N. Pfeiffer and K. W. West, Phys. Rev. Lett. **77**, 2538 (1996).

[40] M. H. Anderson *et al.*, Science **269**, 5221 (1995).

[41] K. B. Davis *et al.*, Phys. Rev. Lett. **75**, 22 (1995).

[42] S. Inouye *et al.*, Nature **392**, 151 (1998).

[43] C. Chin, R. Grimm, P. Julienne and E. Tiesinga, Rev. Mod. Phys. **82**, 1225-1286 (2010).

[44] I. Bloch, J. Dalibard and W. Zwerger, Rev. Mod. Phys. **80**, 885 (2008) .

[45] M. Lewenstein *et al.*, Ad, in Phys. **56**, 1-2, 243-379 (2007).

[46] M. A. Cazalila *et al.*, arXiv:1101:5337.

[47] S. Lloyd, Science **273**, 1073 (1996).

[48] I. Buluta and F. Nori, Science **326**, 108 (2009).

[49] J. Hubbard, Proc. Roy. Soc. A **276**, 238 (1963).

[50] M. C. Gutzwiller, Phys. Rev. Lett. **10**, 159 (1963).

[51] E. H. Lieb and F. Y. Wu, Phys. Rev. Lett. **20**, 1445 (1968).

[52] F. Essler *et al.*, *The One-Dimensional Hubbard Model*, Cambridge University Press, Cambridge, 2005.

[53] R. Gerrirsma *et al.*, Phys. Rev. Lett. **106**, 060503 (2011).

[54] R. Gerrirsma *et al.*, Nature **463**, 68 (2010).

[55] A. Friedenauer *et al.*, Nature Physics **4**, 757 (2008).

[56] M. J. Hartmann, F. G. S. L. Brandao and M. B. Plenio, Nature Physics **2**, 849 (2006).

[57] S. Trotzky *et al.*, Nature Physics **6**, 998 (2010).

[58] J. I. Cirac, P. Maraner and J. K. Pachos, Phys. Rev. Lett. **105**, 190403 (2010).

[59] S. Coleman, Phys. Rev. D **11**, 2088 (1975).

[60] A. B. Zamolodchikov and Al. B. Zamolodchikov, Ann. Phys. **120**, 253 (1979).

[61] H. P. Büchler, G. Blatter and W. Zwerger, Phys. Rev. Lett. **90**, 130401 (2003).

[62] V. L. Pokrovsky and A. L. Talapov, Phys. Rev. Lett. **42**, 65-67 (1979).

[63] R. Jördens *et al.*, Nature **455**, 204 (2008).

[64] U. Schneider *et al.*, Science **322**, 1520 (2008).

[65] M. Girardeau, J. Math. Phys. **1**, 516 (1960).

[66] E. Haller *et al.*, Science **325**, 1224 (2009).

[67] E. H. Lieb and W. Liniger, Phys. Rev. **130**, 1605 (1963).

[68] T. Kraemer *et al.*, Appl. Phys. B **79**, 1013 (2004).

[69] T. Stöferle *et al.*, Phys. Rev. Lett. **92**, 130403 (2004).

[70] A. Iucci *et al.*, Phys. Rev. A **73**, 041608(R) (2006).

[71] S. R. Clark and D. Jaksch, New J. Phys. **8**, 160 (2005).

[72] J. Mun *et al.*, Phys. Rev. Lett. **99**, 150604 (2007).

[73] C. D. Fertig *et al.*, Phys. Rev. Lett. **94**, 120403 (2005).

[74] E. Altman *et al.*, Phys. Rev. Lett. **95**, 020402 (2005).

[75] J. Schachenmayer, G. Pupillo and A. J. Daley, New J. Phys. **12**, 025014 (2010).

[76] S. Rapsch, U. Schollwöck, W. Zwerger, Europhys. Lett. **46** 559 (1999).

[77] Cazalilla, M. A. Bosonizing one-dimensional cold atomic gases. *Journal of Physics B: AMOP* **37**, S1-S47 (2004).

[78] A. Zamolodchikov, Int. J. Mod. Phys. A **10**, 1125 (1995).

[79] P. L. Gould, G. A. Ruff and D. E. Pritchard, Phys. Rev. Lett. **56**, 827 (1986).

[80] J. T. Stewart, J. P. Gaebler, and D. S. Jin, Nature, 744 (2008).

[81] C. H. Schunck, Y. Shin, A. Schirotzek, and W. Ketterle, Nature **454**, 739 (2008).

[82] E. Wille *et al.*, Phys. Rev. Lett. **100**, 053201 (2008).

[83] A. Schirotzek, C.-H. Wu, A. Sommer, and M. W. Zwierlein, Phys. Rev. Lett. **102**, 230402 (2009).

[84] T. B. Ottenstein *et al.*, Phys. Rev. Lett. **101**, 203202 (2008).

[85] J. H. Huckans *et al.*, Phys. Rev. Lett. **102**, 165302 (2009).

[86] G. B. Partridge *et al.*, Phys. Rev. Lett. **97**, 190407 (2006).

[87] S. Giorgini, L. P. Pitaevskii and S. Stringari, Rev. Mod. Phys. **80**, 1215 (2008).

[88] M. A. Cazalilla *et al.*, Phys. Rev. Lett. 95, 226402 (2005).

[89] S. Capponi *et al.*, Phys. Rev. A **77**, 013624 (2008).

[90] P. Azaria *et al.*, Phys. Rev. A **80**, 041604 (2009).

[91] C. W. Gardiner and P. Zoller, *Quantum Noise* (Springer, Berlin, 2005).

[92] N. Syassen *et al.*, Science 320, 1329 (2008).

[93] A. J. Daley *et al.*, Phys. Rev. Lett. **102**, 040402 (2009).

[94] L. M. Falicov, J. C. Kimball, Phys. Rev. Lett. **22**, 997 (1969).

[95] W. V. Liu, F. Wilczek, P. Zoller, Phys. Rev. A **70**, 033603 (2004).

[96] G. G. Batrouni, M. J. Wolak, F. Hbert, V. G. Rousseau, Europhys. Lett. **86**, 47006 (2009).

[97] B. Wang, H.-D. Chen, S. Das Sarma, Phys. Rev. A **79**, 051604(R) (2009).

[98] G. Fath, Z. Domański, R. Lemański, Phys. Rev. B **52**, 13910 (1995).

[99] E. H. Lieb, F. Y. Wu, Phys. Rev. Lett. **20**, 1445 (1968).

[100] J. K. Freericks, E. H. Lieb, D. Ueltschi, Phys. Rev. Lett. **88**, 106401 (2002).

[101] D. Ueltschi, J. Stat. Phys. **116**, 681 (2004).

[102] Z. Domański, R. Łyżwa, P. Erdős, J. Mag. Mag. Mat. **140**, 1205 (1995).

[103] Z. Domański, R. Lemanński, G. Fath, J. Phys.: Condens. Matter **8**, L261 (1996).

[104] Z. G. Wang, Y. G. Chen, S. J. Gu, Phys. Rev. B **75**, 165111 (2007).

[105] A. W. Sandvik, L. Balents, D. K. Campbell, Phys. Rev. Lett. **92**, 236401 (2004).

[106] W. H. Press, B. P. Flannery, S. A. Teukolsky, W. T. Wetterling, *Numerical recipes in C, the art of scientific computing, Second edition* (Cambridge University Press, 1992).

[107] L. Mathey, Phys. Rev. B **75**, 144510 (2007).

[108] P. Farkašovski, Phys. Rev. B **77**, 085110 (2007).

[109] W.L. Chan et al., J. Phys.: Condens. Matter **20**, 345217 (2008).

[110] W. Metzner, D. Vollhardt, Phys. Rev. B **39**, 7, 4462 (1989).

[111] S.-J. Gu, R. Fan, H.-Q. Lin, Phys. Rev. B **76**, 125107 (2007).

[112] F. Wegner, Ann. Physik **3**, 77 (1994).

[113] J. Stein, J. Stat. Phys. **88**, 487 (1997).

[114] M. Takahashi, J. Phys. C **10**, 1289 (1977).

[115] M. Ogata, H. Shiba, Phys. Rev. B **41**, 2326 (1990).

[116] J. Silva-Valencia, R. Franco, M. S. Figueira, Physica B **398**, 427 (2007).

[117] T. Keilmann, I. Cirac, T. Roscilde, Phys. Rev. Lett. **102**, 255304 (2009).

[118] M. Rizzi and A. Imambekov, Phys. Rev. A **77**, 023621 (2008).

[119] T. Roscilde, Phys. Rev. A **77**, 063605 (2008).

[120] O. F. Syljuåsen, Phys. Rev. E **67**, 046701 (2003).

[121] T. Roscilde, C. Degli Esposti Boschi and M. Dalmonte, in progress.

[122] P. Calabrese and J. Cardy, JSTAT P06002 (2004).

[123] E. Burovski *et al.*, Phys. Rev. Lett. **103**, 215301 (2009).

[124] M. den Nijs and K. Rommelse, Phys. Rev. B **40** 4709 (1989).

[125] J. P. Kestner *et al.*, arXiv:1011.2490 (2010).

[126] E. G. Dalla Torre *et al.*, Phys. Rev. Lett. **97**, 260401 (2006).

[127] C. Weitenberg *et al.*, arXiv:1101.2076 (2011).

[128] A. Rapp, G. Zarand, C. Honerkamp, and W. Hofstetter, Phys. Rev. Lett **98**, 160405 (2007).

[129] A. Rapp, W. Hofstetter and G. Zarand, Phys. Rev. B **77**, 144520 (2008).

[130] A. Modawi and A. Leggett, J. Low Temp. Phys. **109**, 625 (1997).

[131] R. W. Cherng, G. Refael, and E. Demler, Phys. Rev. Lett. **99**, 130406 (2007).

[132] K. Rajagopal and Frank Wilczek, in *At the frontier of particle physics, Handbook of QCD*, p. 2061, M Shifman (ed.) (World Scientific, Singapore, 2001).

[133] M. Roncaglia, M. Rizzi, and J. I. Cirac, arxiv:0905.1247.

[134] J. J. Garcia-Ripoll *et al.*, New J. Phys. **11**, 013053 (2009).

[135] G. Vidal, Phys. Rev. Lett. **93**, 040502 (2004).

[136] F. Verstraete, V. Murg, and J. I. Cirac, Adv. Phys. **57**, 143 (2008).

[137] A. J. Daley *et al.*, J. Stat. Mech.: Theor. Exp. P04005 (2004).

[138] S.R. White and A.E. Feiguin, Phys. Rev. Lett. **93**, 076401 (2004).

[139] F. Verstraete, J. J. Garcia-Ripoll, and J. I. Cirac, *ibid.* **93**, 207204 (2004).

[140] A. V. Gorshkov *et al.*, Nature Phys. **6**, 289 (2010).

[141] M. Dalmonte *et al.*, in preparation.

[142] G. Thalhammer *et al.*, Phys. Rev. Lett. **100**, 210402 (2008).

[143] M. A. Cazalilla and A. F. Ho, Phys. Rev. Lett. **91**, 150403 (2003).

[144] M. Mattioli, Master Thesis, University of Bologna (2011).

[145] T. Lahaye *et al.*, Rep. Prog. Phys. **72**, 126401 (2009).

[146] J. Stuhler *et al.*, Phys. Rev. Lett. **95**, (2005).

[147] T. Koch *et al.*, Nat. Phys. **4**, 218 (2008).

[148] M. Lu, S.-H. Youn, and B.L. Lev, Phys. Rev. Lett. **104**, 063001 (2010).

[149] J. G. Danzl *et al.*, Nat. Phys. **6**, 265 (2010).

[150] E.S. Shuman, J.F. Barry and D. DeMille, Nature **467**, 820 (2010).

[151] J. Deiglmayr *et al.*, Phys. Rev. Lett. **101**, 133004 (2008).

[152] T. Lahaye *et al.*, Nature **448**, 672 (2007).

[153] K.-K. Ni *et al.*, Nature **464**, 1324 (2010).

[154] K.-K. Ni *et al.*, Science **322**, 231 (2010).

[155] L.D. Carr *et al.*, New J. Phys. **11**, 055049 (2009).

[156] M. Baranov, Phys. Rep. **464**, 71 (2008)

[157] G. Pupillo *et al.*, in *Cold Molecules: Theory Experiment, Applications* edited by R.V. Krems, W.C. Stwalley and B. Friedrich, (CRC Press, 2009).

[158] B. Capogrosso-Sansone *et al.*, Phys. Rev. Lett. **104**, 125301 (2010).

[159] H.P. Büchler *et al.*, Phys. Rev. Lett. **98**, 60404 (2007).

[160] A. Micheli, *et al.*, Phys. Rev. A **76**, 043604 (2007).

[161] It is finally worth mentioning that other quantum-optics based setups, such as Feshbach molecules and Rydberg atoms, are suitable for investigation of many body phenomena linked to long range interactions: we refer the reader to specific reviews on the subject (Refs. [164] and [145, 165] respectively) for details.

[162] H. J. Schulz, Phys. Rev. Lett. **71**, 1864 (1993).

[163] F. Calogero, J. Math. Phys. **10**, 2197 (1969); B. Sutherland, J. Math. Phys. **12**, 246 (1971).

[164] F. Ferlaino, S. Knoop and R. Grimm, in *Cold Molecules: Theory Experiment, Applications* edited by R.V. Krems, W.C. Stwalley and B. Friedrich, (CRC Press, 2009).

[165] M. Saffman, T. G. Walker and K. Mølmer, Rev. Mod. Phys. **82**, 2314 (2010).

[166] S. Y. T. van de Meerakker *et at.*, Nat. Phys. **4**, 595 (2008).

[167] D. Wang *et al.*, Phys. Rev. Lett. **93**, 243005 (2004).

[168] J. M. Sage *et al.*, Phys. Rev. Lett. **94** 203001 (2005).

[169] T. Rieger *et al.*, Phys. Rev. Lett. **95** 173002 (2005).

[170] S. D. Kraft *et al.*, J. Phys. B **39**, S993 (2006).

[171] A.V. Gorshkov *et al.*, Phys. Rev. Lett. **101**, 073201 (2008).

[172] C. Kollath, J.S. Meyer, and T. Giamarchi, Phys. Rev. Lett. **100**, 130403 (2008).

[173] Y.P. Huang and D.W. Wang, Phys. Rev. A **80**, 053610 (2009).

[174] R. Citro *et al.*, Phys. Rev. A, **75**, 051602 (2007)(R).

[175] R. Citro *et al.*, New J. Phys. **10**, 045011 (2008).

[176] T. Roscilde and M. Boninsegni, New J. Phys. **12**, 033032 (2010) .

[177] J. Hubbard, Phys. Rev. B **17**, 494 (1978).

[178] M.E. Fisher and W. Selke, Phys. Rev. Lett. **44**, 1502 (1980).

[179] F.J. Burnell *et al.*, Phys. Rev. B **80**, 174519 (2009).

[180] G. Quéméner and J.L. Bohn, Phys. Rev. A **81**, 060701(R) (2010).

[181] A. Micheli *et al.*, Phys. Rev. Lett. **105**, 073202 (2010).

[182] M.A. Cazalilla, J. Phys. B: AMOP **37**, S1-S47 (2004).

[183] S. Flach and A.V. Gorbach, Phys. Rep. **467**, 1 (2008), and references therein.

[184] A. Trombettoni and A. Smerzi, Phys. Rev. Lett. **86**, 2353 (2001).

[185] H. J. Schulz, Phys. Rev. B **22**, 5274 (1980).

[186] F. Ferlaino, invited talk at "FerMix 2009 Meeting", Trento, Italy, June (2009).

[187] F. Calogero, J. Math. Phys. **10**, 2197 (1969).

[188] B. Sutherland, J. Math. Phys. **12**, 246 (1971).

[189] G. E. Astrakharchik *et al.*, Phys. Rev. E **74**, 021105 (2006).

[190] C.-M. Chang *et al.*, Phys. Rev. A **79**, 053630 (2009).

[191] A. Argüelles and L. Santos, Phys. Rev. A **75**, 053613 (2007); *ibidem* **77**, 059904 (E)(2008).

[192] A. Pikovski *et al.*, Phys. Rev. Lett. **105**, 215302 (2010)

[193] M. Baranov *et al.*, arXiv:1012.5589.

[194] M. Dalmonte, G. Pupillo and P. Zoller, in progress.

[195] G. Orso, E. Burovski and T. Jolicoeur, Phys. Rev. Lett. **104**, 065301(2010).

[196] A. Micheli, G. Brennen and P. Zoller, Nat. Phys. **2**, 341 (2006).

[197] G.G. Batrouni, F. Hébert, and R.T. Scalettar, Phys. Rev. Lett. **97**, 087209 (2006).

[198] L. Amico *et al.*, New J. Phys. **12**, 013002(2010).

[199] S. Diehl *et al.*, Phys. Rev. Lett. **104**, 165301 (2010).

[200] S. Diehl *et al.*, Phys. Rev. B **82**, 064510 (2010).

[201] B. Paredes, T. Keilmann and J.I. Cirac, Phys. Rev. A **75**, 053611 (2007).

[202] I. Affleck, J. Phys.: Cond. Matter **1**, 3047 (1989).

[203] T. Kennedy and H. Tasaki, Phys. Rev B **45**, 304 (1992);

[204] T. Kennedy and H. Tasaki, Comm. Math. Phys. 147, 431 (1992).

[205] W. Chen, K. Hida and B.C. Sanctuary, Phys. Rev. B **67**, 104401 (2003).

[206] K. Gòral, L. Santos, and M. Lewenstein, Phys. Rev. Lett. **88**, 170406 (2002).

[207] G. Brennen *et al.*, J. Phys. B **38**, 1687 (2005).

[208] F.D.M. Haldane, Phys. Rev. Lett. **50**, 1153 (1983).

[209] F.D.M. Haldane, Phys. Lett. A **93**, 464 (1983).

[210] We verified that a simpler nearest-neighbor approximation leads to appreciable quantitative differences in the phase boundaries.

[211] An analogous pattern in multicomponent systems has been recently proposed in H. Nonne *et al.*, Phys. Rev B **81**, 020408 (R) (2010).

[212] H.J. Schulz, Phys Rev. B **34**, 6372 (1986).

[213] F. C. Alcaraz and Y. Hatsugai, Phys. Rev. B **46**, 013914 (1992).

[214] C. Degli Esposti Boschi *et al.*, Eur. J. Phys. B **35**, 465 (2003).

[215] H. Ueda, H. Nakano and K. Kusakabe, Phys. Rev. B **78**, 224402(2008).

[216] V. Korepin, N.M. Bogoliubov, A.G. Izergin, *Quantum Inverse Scattering Method and Correlation Functions*, Cambridge University Press, Cambridge (1993).

[217] W. S. Bakr *et al.*, Nature **462**, 74 (2009).

[218] E. Altman, E. Demler and M.D. Lukin, Phys. Rev. A **70**, 013603 (2004).

[219] J.F. Sherson *et al.*, Nature **467**, 68 (2010).

[220] P. Sengupta and C. D. Batista, Phys. Rev. Lett. **98**, 227201 (2007).

[221] The factor -2 comes from $\langle 2|bb^\dagger|2\rangle = 0$ and not $\langle 2|bb^\dagger|2\rangle = 3$ as in the usual bosonic Hilbert space: thus $\langle 2|\left[b, b^\dagger\right]|2\rangle = -2$.